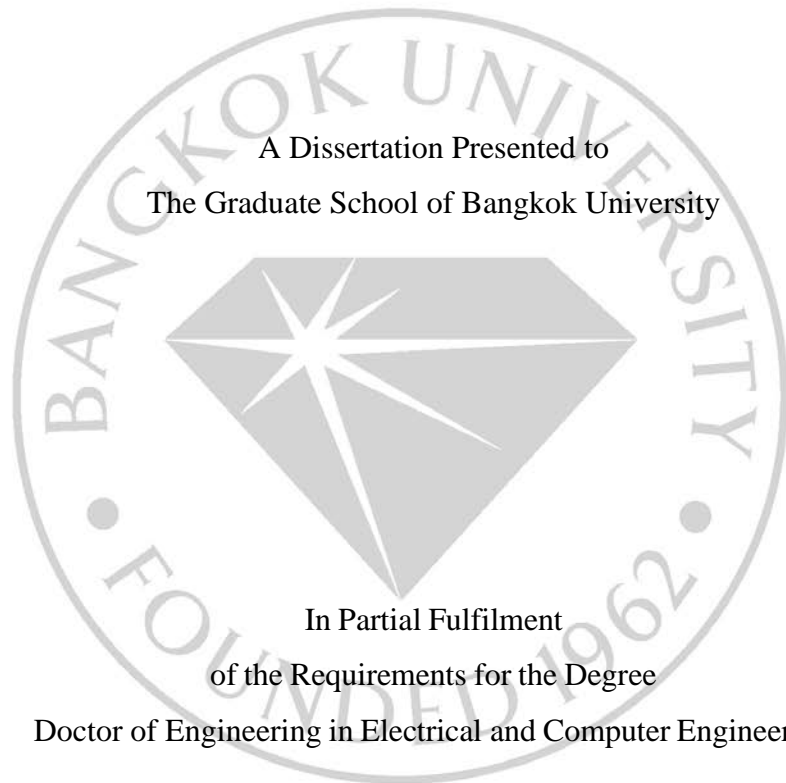


3D PRINTED OPTICAL SYSTEM BASED ON DIGITAL LIGHT PROCESSING
TECHNOLOGY FOR SENSING APPLICATIONS



3D PRINTED OPTICAL SYSTEM BASED ON DIGITAL LIGHT PROCESSING
TECHNOLOGY FOR SENSING APPLICATIONS

A Dissertation Presented to
The Graduate School of Bangkok University



In Partial Fulfilment
of the Requirements for the Degree
Doctor of Engineering in Electrical and Computer Engineering

by
Kankan Swargiary
2021



© 2021

Kankan Swargiary

All Right Reserved

This thesis has been approved by

School of Engineering

Bangkok University

Title: 3D printed optical system based on Digital Light Processing technology for sensing applications

Author: Kankan Swargiary

Thesis Committee:



Thesis Advisor

(Dr. Waleed Soliman Mohammed)



Thesis Co-advisor

(Dr. Romuald Jolivot)



Graduate Program Director

(Asst. Prof. Dr. Chakkaphong Suthaputchakun)



External Representative

(Dr. Mati Horprathum)



(Asst. Prof. Dr. Wisarn Patchoo)

Dean of the School of Engineering

(26 / 06 / 21)

Swargiary, K. Doctor of Engineering in Electrical and Computer Engineering, July 2021,
Graduate School, Bangkok University

3D printed optical system based on Digital Light Processing technology for sensing applications. (167 pp.)

Advisor of Dissertation: Waleed Soliman Mohammed, Ph.D.

ABSTRACT

This research demonstrates the design, fabrication and development of a simple and practical cost-effective optical waveguide system by making use of 3D printing Digital Light Processing technology for sensing applications. The cost is minimized by utilizing 3D printing Fused Deposition Method technology to print the mechanical components involved.

This research involves a new approach to fabricate a single-step integrated optical waveguide system where strong light confinement in the ridge (guiding) section of the fabricated structure is realized through the introduction of an elevated (tower-shaped) waveguide in a transparent photosensitive resin (PX-8880) with refractive index $n=1.47$. This fabrication scheme is optimized to maximize light confinement through varying the dimensions of the guiding region and the tower structure. The FEM simulation with the desired parameters of the fabricated structure performed showed strong light confinement in the guiding region. Benefiting from the surface roughness produced by the slicing process in the 3D printing DLP technology ($50\mu\text{m}$ resolution), the fabricated structure was tested for vapor sensing. Intensity

dynamics responses are achieved due to the change of the optical scattering from the presence of vapor as well as polymer resin vapor interaction where it displayed a potential to implement it as a sensor.

Further optimization of the fabricated structure was enhanced by introducing a gap in the ridge region of waveguide system and it is implemented as a practical isopropanol alcohol (IPA) concentration sensor without in need of a vacuum system. This is also done by designing and fabricating using 3D printing DLP technology using photosensitive MonoCure 3D Rapid UV clear resin with the refractive index $n=1.50$. Various waveguides with different gap size along the horizontal region (guiding region) were printed and comparisons were performed for the several gap sizes including the structure without the gap by implementing re-coupling of light concept and swelling characteristics of the photopolymer resin resulting in higher transmitted light power/intensity in the presence of alcohol. Three different concentrations (2.5 μ l, 5 μ l and 10 μ l) of IPA was used for testing with the fabricated structures. The parameters investigated are the dimensions of the waveguide gap with its overall structure and the sensor chamber.

The waveguide gap size of 300 μ m displayed the strong confinement at the ridge region with the increase in transmitted optical power for 65% when tested with 10 μ l (500ppm) concentration of IPA and faster response time in increasing transmitted optical power rise after depositing IPA in the sensor chamber for $t=5$ seconds compared to all the gaps with Limit of Detection (LOD) of 0.366 μ l. In addition, the fabricated waveguide gap structure of 300 μ m demonstrated the sensing limit of IPA concentration below 400ppm which is considered as an exposure limit by “National

Institute for Occupational Safety and Health”.

Thus, the fabricated optical system successfully demonstrated its usefulness with its ease of fabrication using 3D printing DLP technology and proved as a sensor where the dimensions are in hundreds of microns.

Keywords: Polymer, Resin, 3D printing, Digital Light Processing, Isopropanol alcohol, Swelling effect, Fused Deposition Method



Approved: _____

Signature of Advisor

ACKNOWLEDGEMENT

I would like to express my sincere gratitude to all those people who supported me throughout my doctoral studies and completion of this thesis. Foremost, my deep sense of thanks and gratitude is to my advisor **Dr. Waleed S. Mohammed** for his continuous support, guidance, enthusiasm and motivation during my studies in Bangkok University. He provided me with a great research environment, timely advice, and continuous help, being main reason for completion of my thesis. I would also thank my co-advisor, **Dr. Romuald Jolivot**, for his suggestions, constructive comments, constant encouragement and scientific guidance for my research work.

I express my gratitude to **Dr. Sakoolkan Boonruang**, Researcher, Photonics Technology Research Team (PHT), National Electronics and Computer Technology Centre (NECTEC), Thailand, for her timely suggestions, motivation, and lab facilities.

My sincere thanks to the **Bangkok University Teaching Assistance (BUTA) Scholarship Award** for partial tuition fee waiver support for my doctoral studies and also giving me an opportunity to be a Teaching Assistant in Laboratory classes for undergraduate students for teaching experience.

I also thank all the faculty members and students from **BU-CROCCS**, and also to all my friends, teachers, and **Dr. Sunandan Baruah**, Dean, Engineering and Technology, **Assam Down Town University** back in India, for playing vital role in shaping my career.

I also thank my wife **Jirina Basumatary** for putting up with me being sat in the office for hours on end and for providing spiritual support and patience throughout this journey.

Finally, I express my deepest appreciation to my precious family for their never-ending encouragement and support in every way to succeed in my education and throughout giving an opportunity.



TABLE OF CONTENTS

	Page
ABSTRACT.....	iv
ACKNOWLEDGEMENT.....	vii
LIST OF TABLES.....	xiii
LIST OF FIGURES.....	xiv
CHAPTER 1 INTRODUCTION.....	1
1.1. Polymer-Optical Waveguide.....	2
1.2. 3D Printing Technology.....	5
1.3. Material Extrusion.....	5
1.4. Material Jetting.....	6
1.5. Vat Polymerization.....	6
1.6. Research Aims.....	8
1.7. Research Focus.....	8
1.8. Objectives Of The Study.....	9
CHAPTER 2 LITERATURE REVIEW.....	14
2.1 Waveguide Types.....	15
2.1.1 Planar Waveguide.....	15
2.1.2 Non-Planar Waveguide.....	21
2.2 Losses in an Optical Waveguide.....	23
2.3 Waveguide Materials.....	25
2.3.1 Material Properties.....	25
2.3.1.1 Optical Properties.....	25
2.3.1.2 Typical Optical Waveguide Materials.....	27

TABLE OF CONTENTS (Continued)

	Page
CHAPTER 2 LITERATURE REVIEW (Continued)	
2.4 Polymer-Based Waveguide	30
2.4.1 Fabrication Techniques For Polymer-Based Waveguide.....	32
2.5 3D Printing DLP Technology	33
2.5.1 DLP Technology.....	34
2.5.2 Materials for DLP-Based 3D Printers.....	39
2.5.3 Photopolymerization.....	39
2.5.4 Monomer and Oligomers.....	40
2.5.5 Photoinitiators.....	41
2.5.6 Photopolymer.....	44
CHAPTER 3 NUMERICAL METHODS.....	51
3.1 Basic Equations	51
3.1.1 Maxwell's Equation.....	52
3.1.2 Boundary Conditions.....	53
3.1.3 Wave Equations.....	55
3.2 Brief Comparison of Different Numerical Methods	57
3.2.1 Finite Difference Method.....	57
3.2.2 Finite Difference Time Domain Method.....	58
3.2.3 Finite Element Method.....	58
3.3 Fundamental Of Finite Element Method	59
3.3.1 Variational Formulations.....	61
3.3.2 The Scalar Approximations.....	62
3.3.3 Vector Formulations.....	62

TABLE OF CONTENTS (Continued)

	Page
CHAPTER 3 NUMERICAL METHODS (Continued)	
3.4 Outline Of Finite Element Formulation	64
CHAPTER 4 DESIGN AND FABRICATION OF THE WAVEGUIDE.....	69
4.1 Concept Of The Waveguide Structure.....	69
4.2 Flow Chart for Modelling The Waveguide Structure.....	74
4.3 Fabrication Of The Tower-Shaped Waveguide Structure.....	74
4.4 Optical Characterization Of The Fabricated Structures.....	78
4.4.1 Surface roughness quantification of the fabricated structure.....	81
4.4.2 Power Attenuation Analysis.....	87
4.5 Response Of The Single-Step Tower-Shaped Waveguide Structure.....	91
CHAPTER 5 SINGLE-STEP TOWER-SHAPE GAP WAVEGUIDE STRUCTURE.....	97
5.1 Design Of The Tower-shaped Gap Waveguide Structure.....	97
5.2 Fabrication Of The Tower-shaped Gap Waveguide Structure.....	99
5.3 Design Of The Sensor Chamber.....	101
5.4 Principle Of Operation For The 3D Designed Waveguide Gap Structure.....	102
5.5 Response Of The Tower-Shaped Waveguide Gap Structure.....	105
5.5.1 Repeatability Response Trend Of The Tower-Shaped Waveguide Structure.....	107
5.5.2 Response Of The Different Tower-Shaped Waveguide	

TABLE OF CONTENTS (Continued)

	Page
CHAPTER 5 SINGLE-STEP TOWER-SHAPE GAP WAVEGUIDE STRUCTURE (Continued)	
Gap Structure.....	109
CHAPTER 6 CONCLUSIONS AND FUTURE WORK.....	123
BIBLIOGRAPHY.....	127
APPENDICES.....	145
APPENDIX A.....	147
APPENDIX B.....	155
APPENDIX C.....	157
APPENDIX D.....	159
APPENDIX E.....	160
BIODATA.....	166
LICENSE AGREEMENT OF DISSERTATION PROJECT.....	167

LIST OF TABLES

	Page
Table 2.1: Comparison of various 3D printing technologies.....	35
Table 2.2: Commercial UV- light sensitive photoinitiators for 3D printing.....	43
Table 2.3: Property parameters of photopolymer resin.....	45
Table 4.1: Different dimensions for the designed tower-shaped waveguide.....	75
Table 4.2: Differentiation between practical and theoretical value of line size in the waveguide tower area and the floor area.....	83
Table 4.3: Evaluation of GLCM metrics of polished and un-polished structures.....	87
Table 5.1: Discrete gap dimensions of the waveguide	99
Table 5.2: Likeness of the structures gap dimensions (3D printed).....	100
Table 5.3: Isopropanol alcohol conversion (μL to ppm)	102
Table 5.4: Comparison table between different waveguide gaps (in percentage) to different IPA amounts.....	112
Table 5.5: Limit of Detection (LOD) of different fabricated gap dimensions.....	121
Table B1: Curing properties of various acrylates (3Dprinter.wikidot, 2011).....	155
Table B2: Properties of oligomer types (Idacavage, 2012).....	156

LIST OF FIGURES

	Page
Figure 2.1: Principle of light guidance at the optical interface at the entrance and exit of an optical waveguide.....	15
Figure 2.2: Typical structure of the planar waveguide.....	16
Figure 2.3: Concept showing the TIR at the two interfaces of a slab waveguide.....	17
Figure 2.4: Wave representation of TE and TM modes in a planar waveguide (Pavesi & Guillot, 2006).....	19
Figure 2.5: Various types of waveguides: (a) ridge waveguide; (b) rib waveguide; (c) strip-loaded waveguide; (d) immersed waveguide; (e) metal waveguide; (f) buffered metal waveguide (g) vertical slot waveguide (h) horizontal slot waveguide (i) hollow waveguide.....	22
Figure 2.6: Propagation loss of various polymer waveguides with different polymer materials at difference length (Bamiedakis et al., 2009; Wang et al., 2010; Kim et al., 2003; Jiang et al., 2013 and Papakonstantinou, 2008).....	31
Figure 2.7: Schematic diagram of the DLP based 3D printing technology (Ngo et al.,2018).....	38
Figure 2.8: Diffusion model of the substance in swelling polymer film (Muto et al., 1998).....	46
Figure 2.9: Swelling mechanism by ray tracing model (Muto et al., 1998).....	49
Figure 3.1: Index of refractive medium of the boundaries between two medias with \mathbf{n} as the unit vector.....	54
Figure 3.2: Random shape of optical waveguide having contrasting materials.....	60

LIST OF FIGURES (Continued)

	Page
Figure 3.3: Arbitrary shaped waveguide structure cross section area Ω and boundary Γ	63
Figure 4.1: (a) Ridge area mode confinement in the tower-shaped waveguide structure (b) Base area mode confinement in the waveguide structure without tower	70
Figure 4.2: Flow chart of the FEM technique using MATLAB program to calculate the field distribution for fundamental mode in the tower-shaped waveguide structure.....	71
Figure 4.3: Traditional ridge waveguide structure field distribution for fundamental mode.....	72
Figure 4.4: (a) Design parameters of the tower-shaped waveguide (b) Confinement of mode in the ridge area	73
Figure 4.5: Fabrication steps of the tower-shaped waveguide structure.....	75
Figure 4.6: (a) Creation Workshop platform (b) 3D designed elevated waveguide with the support generation and rotated at 25 degrees by lifting towards Z-axis (c) DLP based 3D printer Wanhao Duplicator D7 Box.....	76
Figure 4.7: Illustrated diagram of the DLP based 3D printer.....	77
Figure 4.8: Illustrative optical set-up for investigation of confinement of light and transmitted power calculation	79
Figure 4.9: Captured images of the varying dimensions of the tower region confinement of light with 600 μm ridge area (a) 80 μm , (b) 100 μm , (c) 150 μm , and (d) 200 μm	80

LIST OF FIGURES (Continued)

	Page
Figure 4.10: (a) Illustrative view of the waveguide tower structure with supports at the base with 25-degree print angle for appropriate pixelation and 50 μ m roughness of the surface. (b) Front view of the waveguide tower structure displaying its roughness of the surface. (c) Waveguide tower structure oblique view. (d) Top view of the waveguide tower structure floor region	82
Figure 4.11: (a) Top view of the structure lines in the tower area (a-3) and in floor area (left area: a-1, right area: a-2) (b) Front view of the structure slicing lines. (c) Top view of the floor area of the structure (c.1) polished area and (c.2) non-polished area	85
Figure 4.12: Vertical evaluation of transmission of the fabricated structures.....	88
Figure 4.13: Approximation evaluation of the structure's attenuation coefficient by the incident light at vertical position and its different acquired positions	89
Figure 4.14: Attenuation coefficient of the different fabricated waveguide structures.....	90
Figure 4.15: Tower dimension α coefficient Vs normalized transmittance.....	91
Figure 4.16: The 3D designed vapor chamber using Autodesk 123D CAD software for sensing analysis.....	92
Figure 4.17: Block diagram for the experimental setup of vapor detection investigation	93

LIST OF FIGURES (Continued)

	Page
Figure 4.18: Optical power evaluation graph of 200 μ m dimension waveguide structure using 50 μ l and 100 μ l IPA amount.....	94
Figure 5.1: Design concept of the tower-shaped gap waveguide structure.....	98
Figure 5.2: Captured images of both designed and measured printed gap structures.....	100
Figure 5.3: 3D designed sensor chamber structure with overall volume of 20 cm^3	101
Figure 5.4: Concept of scattering and swelling property of polymer (a) Interaction process between polymer and air (b) Interaction process between polymer and alcohol	103
Figure 5.5: Operating principle of 3D designed waveguide gap structure (a) Leaky-type gap structure (b) Guided-type gap structure.....	105
Figure 5.6: Experimental setup and schematic diagram for testing waveguide gap structure	106
Figure 5.7: (a) Repeatability response of the sensor with 125 ppm concentration of IPA (b) Repeatability response of the sensor with 500 ppm concentration of IPA (c) Repeatability response of the waveguide with 250ppm concentration of IPA	108
Figure 5.8: Response time variation of the different gap sizes of the waveguide structures with 5 μ l (250ppm) concentration of IPA.....	110
Figure 5.9: Schematic showing the light coupling and numerical aperture effect from the waveguide 1 to waveguide 2.....	113
Figure 5.10: Acceptance angle calculation from the measured number of readings	115

LIST OF FIGURES (Continued)

	Page
Figure 5.11: Experimental set-up of humidity, temperature and optical power measurement	116
Figure 5.12: Response time measurement of waveguide gap structure of 300 μ m (a) Transmitted power (b) Humidity and (c) Temperature.....	117
Figure 5.13: Comparison graph of different gap structures along with percentage increase power	118
Figure 5.14: LOD calculations for different gaps: (a) 0 μ m, (b) 250 μ m, (c) 300 μ m, (d) 400 μ m, (e) 500 μ m.....	120
Figure E1: Left Center and Right image.....	162
Figure E2: Left and Right image.....	162

CHAPTER 1

INTRODUCTION

The main concept of the integrated optics was first proposed by Dr. S.E. Miller of Bell Labs in the United States, 1969 (Miller, 1969). With these, the optical devices such as optical fiber and optical integrated circuits replaced the traditional wire links and electrical integrated circuits. As a result, a huge mass manufacturing of low-cost integrated circuits came into picture.

Integrated optics is a technology of building integrated optical devices, photonic integrated circuits or a planar circuit, containing several optical components which are combined to achieve complex functions (Hunsperger, 1984). Such components are optical filters, modulators, lasers and photodetectors. They can be fabricated on the surface of some crystalline materials (e.g., silicon, silica, or LiNbO_3) and connected with waveguides (Tien, 1971).

The inspiration of integrated optics emerged from the electronic integrated circuits, that has shown a rapid development over the past decades. This has accelerated a series of milestones, such as powerful microprocessors and computer memory chips with massive data storage capacity (Stegeman et al, 1988). However, integrated optics has not been able to compete the progress of microelectronics in terms of the complexity of devices. Some of the limitations are mentioned in the following list:

1. Electronic circuits contain many small wires and for that, the optical components must to be connected via waveguides and the dimensions

cannot be smaller than the wavelength. For this reason, it fails to hold very sharp bends. This can be eliminated by using waveguides with very high index contrast, e.g., nanowires, nanofibers, photonic crystals and photonic wires.

2. Optical connections between waveguides and couplers are significantly more complex than electrical circuit connections.
3. Waveguide device connections exhibit optical losses, which often needs to be boosted with optical amplifiers.

For these reasons, integrated optical circuits have not attained the complexity process. However, for devices having moderate complexity, it can be useful for optical fiber communications. Such as distributed feedback lasers, optical modulators, photodiodes, and optical filters. Recently, a new powerful, flexible, broad compatibility and cost-effective integrated optical technology has arisen from developments in polymer photonics (Okamoto,1999). With its transparency and reliability in nature, polymers are widely commercially available and its extensive research and development for waveguide applications can be seen. One of the increasing areas for the research in polymer photonics is based on guided wave optics where the light is trapped inside a core of the waveguide with maximum index of refraction surrounded by minimum index of refraction in the cladding area for high sensing applications.

1.1 Polymer-Optical Waveguide

In integrated optics, the employment of optical waveguides based on

polymer in the dimension of microns is extensively rapidly rising for few years in the past where the polymers such as PMMA (Koo et al., 2003), OrmoComp (Viphavakit et al., 2014), PDMS (Sieber et al., 2012) and Poly(methylmethacrylimide) (PMMI) (Prajzler et al., 2011) were used for realization of integrated optical components. Polymers based on waveguide structures are highly chose due to their processibility and loss characteristics as it suffers scattering from roughness of the surface which is an advantage (Hu et al., 2008).

The most widely used materials for optical integrated circuits are silica, semiconductor, LiNbO_3 , and polymers. Silica, Silicon, and LiNbO_3 are excellent substrate materials for the fabrication of integrated optical devices. Some expensive lithography technique such as deep-ultraviolet (UV) or E-beam lithography is required for waveguide nanowire fabrication due to the submicron cross section (Kawachi et al., 1990).

A widely known material used as optical waveguide is silicon nanowire. In photonics and optoelectronic applications, it is being widely employed (Dell'Olio et al., 2007). The sensors made from silicon nanowire can detect the index of effective region change in the guided area. This type of mechanism is known as surface detection. The mostly used optical sensors are made of Silicon-On-Insulator (SOI) technology. This displays a maximum confinement of light in the sensing area (Leung et al., 2011). Here, the guided light in index of refraction at maximum area are sandwiched mostly by SOI substrate and the local area by water or air. The foremost target in sensing applications is for detection of a minute

variation in the index of refractive in cladding area. Yet, for obtaining the mentioned specifications, highly advanced instruments, vacuum system and cleanrooms are required which is expensive and requires strong handling to create. On that account, the employment of other material types is of huge interest for creating an optical waveguide.

The optical waveguides made of polymers are apprehended as a fascinating device in sensing applications for their distinctive properties. It offers the possibility of low-cost fabrication and soft lithography replication (Flores et al., 2008). Furthermore, it is taken as a promising candidate to address the requirement of optical interconnects (Lin et al., 2013). Polymer has increased the compatibility with printed circuit boards and flexible substrates (Immonen et al., 2005). It also has a large transparent platform from the visible to infrared waveband, which is compatible for wide range of applications (Jiang et al., 2013).

Besides, the refractive index (RI) of polymeric material, it can also be easily adjusted through synthesis processing and heat treatments (Ke et al., 2006). Hence, there is a variety of sensing applications due to their favorable optical and electrical properties. Polymers are economical, easier for operation and workable for meeting an application in broader area (Xu et al., 2017) (Kemp et al., 2007). Nanoimprint (Viphavakit et al., 2014), UV written (Koo et al., 2003) (Khatri et al., 2019) are few techniques employed for fabricating optical waveguides application as a sensor. In regard to all these techniques, an fascinating method for developing optical waveguide is based on 3D printing technology where a strong potential for sensing in easier manner is possible.

1.2 3D Printing Technology

The 3D printing makes use of rapid prototyping. It is a form of AM (Additive Manufacturing). AM has undergone vast development since its conception in 1984 presented by Chuck Hull as a first commercial rapid prototyping technology that is known as Stereolithography (Gibson et al., 2015). AM process are used to design and create parts by addition of material in a layer wise fashion (Gibson et al., 2015). Additionally, these processes allow cheaper and faster operations comparing to conventional methods. In 3D printing, a desired structure is first digitally designed in the CAD (Computer Aided Design) software and then the digital data is loaded in the 3D printer of choice and the structure is acquired. There are various approaches for designing and developing a 3D printed structure using 3D printing technology. As according to ASTM (American Society for Testing and Materials), AM techniques are classified into 7 different categories based on the materials. Out of these categories, some of these processes are elaborated below.

1.3 Material Extrusion

Material extrusion is most commonly used by the fused filament fabrication (FFF) process. According to ASTM Standard F2792, this is defined as “a material extrusion process that is used to make thermoplastic parts through heated extrusion and deposition of materials layer by layer” (Groover, 2013). This is also known as Fused Deposition Modeling (FDM) process (Stratasys, 2017). The extruded material takes desired shape after being extruded from a tiny

nozzle tip, typically 0.3 to 0.5 mm in diameter. A thermoplastic filament in the form of thin wires is used as the base material (Bellini et al., 2003). Most of the 3D printers that falls in this category typically uses thermoplastic materials such as PLA (Polylactic acid), ABS (Acrylonitrile butadiene styrene), TPU (Thermoplastic Polyurethane) etc., as their filaments.

1.4 Material Jetting

Material jetting (MJ) is a widely used 3D printing technology which uses a photopolymer-based ink that is jetted out and then cured on a substrate. Multiple materials with different colors and textures can be printed using this method. In MJ, a printhead dispenses a droplet of photosensitive material that solidifies under ultraviolet (UV) light, building a part layer-by-layer (Willis, 2012). The materials used in MJ are thermoset photopolymers (acrylics) which is in a liquid form. Multiple inkjet printheads are also attached side-by-side and material is deposited on the whole print surface in a single go (Wolfer et al., 2014).

1.5 Vat Polymerization

Vat polymerization is a technique that uses a vat of photopolymer resin, upon which the model is built layer by layer fashion. An UV light is used to harden the resin during its operation, where a print platform moves the object downwards (Z-direction) after each new layer is formed. Resins are cured using a process called photo polymerization (Gibson et al., 2015) by UV light where the light is exposed to the surface of the resin using motor-controlled mirrors. Digital Light

Processing (DLP) technology is a type of a 3D printing method that is based on image projection technology developed by Texas Instruments in 1980's (Lu et al.,2006). DLP technology uses vat polymerization method where light is projected onto the resin and the entire layer is printed immediately. Hence, this technology allows fast printing (Ngo et al., 2018).

Comparing with the 3D printing methods: extrusion-based 3D printing technology and material jetting 3D printing technology have a significant advantage in printing resolution, efficiency, and working condition. Hence, it can bring multiple useful features to the products. Some of its applications are in medical field, that can be used for printing splints, jaw, etc. for Orthognathic surgeries (Metzger et al., 2008). In optics, it is used for developing optical components such as transparent glass (Klein et al., 2015), lens (Zhang et al., 2016).

In this work, 3D printing based DLP technology is used for fabricating an optical system which is a polymer-based optical waveguide structure and it is implemented as a sensor for vapor sensing application. With the help of DLP technology, two types of waveguides based on polymer are designed and fabricated for achieving maximum confinement of light for converting into highly responsive sensors. Also, for the sensor chamber is developed by material extrusion-based 3D printing technology. With this technology, the cost of the overall system is reduced and it is implemented as an alternative fabrication technique where a requirement of vacuum system is excluded as the dimensions are in microns.

1.6 Research Aims

In this research work, the aim is to develop two different types of polymer-based waveguide that is implemented as a sensor for vapor sensing applications. This work encompasses a new approach for designing and fabricating an optical waveguide using a photopolymer resin by 3D printer Digital Light Processing technology. CAD software is used for the designing the digital file of that waveguide and later fabricating it with 3D DLP printer. This work is based on utilizing an alternative fabrication scheme by excluding highly sophisticated instruments and expensive techniques. Hence, making it more relatively simpler and inexpensive technology where an advantage of easier operation and high accuracy is involved.

1.7 Research Focus

The design of the waveguide based on polymer involves a new approach, i.e., both core and base area are fabricated with similar material ensuring maximum confinement of light in the core area when light is illuminated at the waveguide face. Generally, for maximum confinement of light at the ridge/core area, a higher index refraction is needed in core area comparing to the base and local area. This type of designing is acquired in lithography, thin film deposition, and imprinting techniques. When the core and the base structure is developed using similar material, the appeared modes get confined in the base area. This phenomenon is not accepted when dealing with application as a sensor. Therefore,

this work is focused on the development of an optical waveguide where the design is carried forward by guiding the light in the ridge area for achieving higher confinement or power at maximum by lifting the ridge area in upward direction, sitting on a tower. By doing so reduces the index of refraction index in the base area. This phenomenon is acquired by introducing a tower shaped waveguide by employing 3D printer based DLP technology. The dimension of the tower for maximum confinement of light in the core area and a minimum gap dimension in between the waveguide is investigated in this work for re-coupling of light and acquiring of maximum power for alcohol-concentration application as a sensor.

1.8 Objectives Of the Study

This research work objectives are to design, develop and characterize an optical waveguide based on polymer employing 3D printer based DLP technology for application as a vapor sensor. The two different types of optical waveguides based on polymer are fabricated, i.e., single step tower-shaped waveguide and single step tower-shaped gap waveguide. The list of objectives in particular are given:

1. Designing and fabricating based on a new approach for optical waveguide based on polymer, i.e., tower shape waveguide.
2. To optimize the dimensions for minimum dimension of the tower for best optical guiding property for achieving highest possible confinement of light/power in the ridge area.
3. Optimization of the minimum gap dimension in between of the tower-

shaped waveguide for acquiring higher sensitivity.

4. To investigate the guided mode in the ridge section of the tower shape waveguide using Finite Element Method.
5. To perform experimental measurements of the surface roughness of the fabricated tower shape waveguide for light scattering that is generated due to printing resolution of the 3D DLP printer for the feasibility towards optical sensing application.
6. To analyze the texture of the fabricated waveguide using Grey level Co-occurrence Matrix (GLCM) for surface roughness quantification.
7. To construct the optical characterization setup (which includes the sensor chamber, holder stands for the camera and various related mechanical mounts) using 3D printer FDM technology and a powermeter for experimentally analyzing the power confinement, the attenuation coefficient and the behavior of the transmitted optical power for both tower shaped waveguide and tower-shaped gap waveguide with the changes of the environment within the sensor chamber.

Chapter 1 is about brief background introduction of integrated optics that has displayed a great advantage in recent years with the development of miniature devices that have high throughputs. It gives an eye opener of the different polymer-based waveguides that are fabricated using different methods. It also describes about how 3D printer technology can eliminate those expensive fabrication techniques when the dimensions are in hundreds of microns. This chapter also provides the research aim, research focus and the research objectives.

In Chapter 2, a literature reviews related to this research work and a theoretical background is discussed and elaborated. The chapter starts with a theoretical background of the optical waveguides, its various types and the type of common materials from which the waveguides are fabricated. A brief description of losses involved in the optical waveguides are also reported. It also provides a review of polymer-based waveguide with different techniques involved for fabricating and its implementation for various sensing applications. This chapter also provides the literature review of 3D printing DLP technology and its advantages for printing micron scale structures. In the end, the purpose for choosing the resin as a material to fabricate the waveguide and its swelling characteristics due to vapor/alcohol-polymer interaction in application field is discussed.

Chapter 3 reviews various numerical methods used in the analysis of waveguide design and discusses the comparison among them. It begins with providing the basic introduction of the Maxwell's equations and its wave equations for EM fields. It also discusses the fundamental theory of numerical analysis used in this study, particularly the Finite Element Method for calculation of modes and its solution to optical waveguide problems in general.

Chapter 4 discusses the concept used for designing the waveguide and the fabrication techniques involved. The implementation of FEM numerical method calculation to check the field distribution for the fundamental mode in the ridge section of the designed waveguide structure before the actual fabrication is also detailed. The fabrication process and its post-processing methods after

obtaining the desired structure is explained step by step. The roughness of the surface acquired in designed waveguide structure is from printers resolution that results in scattering is also evaluated and explained in this chapter. The waveguide is later tested initially with isopropanol as a vapor element to check its response and its transmitted optical power and its possibility to implement as an alcohol detection sensor.

In the chapter 5, the fabricated single step tower-shaped waveguide is further extended by a gap in the middle of the tower-shape waveguide structure i.e., in horizontal line. By making use of the roughness of the surface acquired by the 3D printer based DLP technology, a number of waveguides with a different gap dimensions were fabricated. It is then distinguished for optimizing the confinement of light at the ridge area that is utilized by the re-coupling of light principle that arises from gap. The occurrence of swelling effect characteristics of the polymer resin when it interacts with Isopropanol alcohol resulting in diffusion of alcohol molecules is discussed and reported. With this principle, the fabricated tower-shape gap waveguide is implemented as alcohol-concentration sensor. Also, optimization of the gap parameter of the waveguide structure is explained. The fabricated waveguide gap structure is then tested and analyzed with different volumes of Isopropanol alcohol for checking the system sensitivity. The sensitivity of the system is distinguished with the wanted value of detection given by National Institute for Occupational Safety and Health.

In Chapter 6 an overall conclusion in general is discussed that outlines the accomplished work in this work and presents the potential expansion of the

present work for upgrading the execution of the tower-shaped waveguide based on polymer material for using them in sensing applications as in detecting other family of alcohol with its detection possibility at lowest standards/amounts.



CHAPTER 2

LITERATURE REVIEW

Optical waveguides are spatially inhomogeneous structure for guiding light. A typical waveguide structure contains a section of higher refractive index, compared to its surrounding medium/cladding region. The guidance of light is also possible by the use of reflections at metallic interfaces that involves plasmonic effect at metal interface (Chin et al., 2005). Optical waveguides are the basic component for confinement and transmission of light over various distances, ranging from tens or hundreds of micrometers. It displays an advantage in semiconductor lasers as a passive and active device. These devices can be waveguide couplers and modulators (Mookherjea, 2004). “Optical waveguiding was first referred to as light piping in 1880” by Wheeler. Today, it is known as fiber optics technology as transmission of light through a glass pipe medium was displayed (Hong et al., 2002). Optical waveguides are the structures for guiding the electromagnetic waves in the optical radiation range band. Typically, a waveguide consists of three regions with different refractive indices: the cladding (n_{clad}), the core (n_{core}) and the substrate (n_{sub}). However, guided wave optics depends on the phenomenon of the total internal reflection (TIR) where light gets trapped inside the waveguide with the material surrounded by lower refractive index as shown in the figure 2.1. Most waveguides exhibit the direction of propagation of guided light in one medium (Vassallo, 1991).

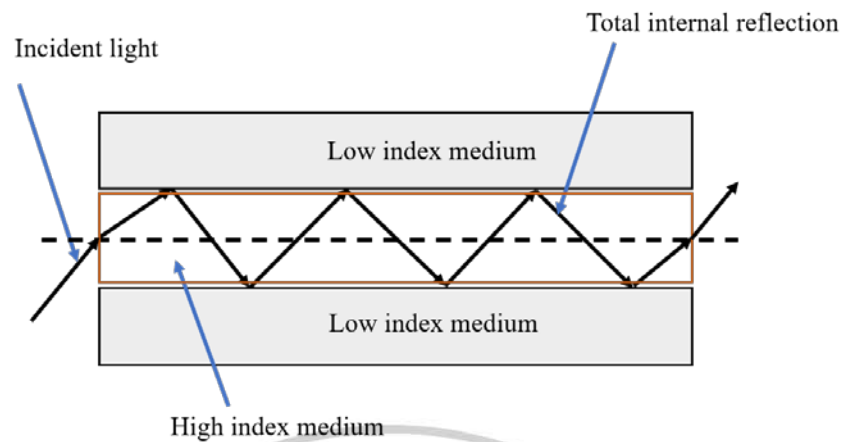


Figure 2.1: Principle of light guidance at the optical interface at the entrance and exit of an optical waveguide

2.1 Waveguide Types

There are different types of waveguides, out of which it can be classified into two categories: planar and non-planar waveguide. Planar waveguide has the light confinement is only in one direction, i.e., the core is sandwiched between the cladding layers. In non-planar waveguide, the core is surrounded by cladding layers in all transverse directions (e.g., channel waveguide and optical fiber).

2.1.1 Planar Waveguide

Here, the sheet beams utilization is involved and are confined in one dimension. This propagates in any direction parallel to the surface of the high index guiding layer. By introducing a thin film with the higher refractive index than the substrate, the light can be trapped inside the film and waveguiding's are

produced. Figure 2.2 shows a typical design of a planar waveguide.

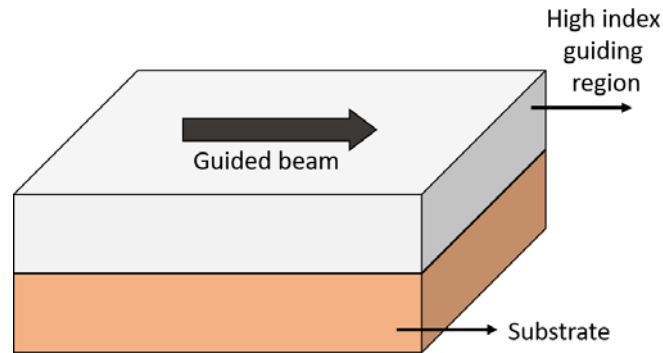


Figure 2.2: Typical structure of the planar waveguide

To fully understand the light propagation in an optical waveguide the study of electromagnetic waves is important. For ease of understanding, a planar waveguide that confines the light in one-dimension is presented. The optical ray model is used to describe the propagation of guided waves in a medium without handling the Maxwell equations (Reed, 2008). This model involves the implementation of Snell's Law to explain the behavior of propagating waves in a medium with the RI (refractive index) n_1 between two regions with the RI n_2 . The relationship between the RI's and the angles of incidence θ_1 and refraction θ_2 is defined as:

$$n_1 \sin \theta_1 = n_2 \sin \theta_2 \quad (2.1)$$

The refractive index difference Δn is used to express the relative difference in refractive index of the core (n_1) and cladding (n_2) which describes the light guidance of the structure. For example, planar waveguides with a very low index contrast ($\Delta n \ll 1$) are considered weakly guided mediums.

$$\Delta n = \frac{n_1 - n_2}{n_1} \quad (2.2)$$

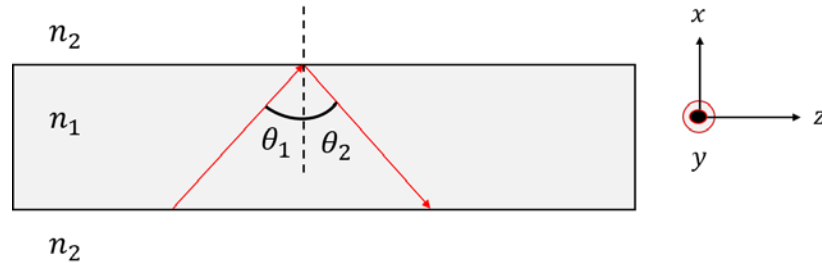


Figure 2.3: Concept showing the TIR at the two interfaces of a slab waveguide

In figure 2.3, the refractive index of the layer 1 (n_1) is larger than the surrounding layers (n_2). According to the Snell's law it can be stated that for an angle of incidence greater than the critical angle θ_c , total internal reflection (TIR) occurs and light is successfully guided. Hence,

$$\sin \theta_c = \frac{n_2}{n_1} \quad (2.3)$$

This concept outlines how the light is confined by TIR and propagates along the z-direction.

There is a condition that the waveguide differs, that is a waveguide is said to be symmetrical if the same boundary conditions will apply at the upper and lower interfaces. On the other hand, the waveguide is said to be asymmetrical if it contains two different layers, e.g., the substrate is made of Si (n_2) and the upper layers is air (n_3). The approximation of the geometrical optics is sustainable when the dimensions of the core area are much larger than the wavelength of the light. If smaller than the wavelength of the light, the approximation is not rational and the light is considered as true nature (EM wave) and the investigation of the

waveguide is justified by Maxwell's equations.

A waveguide mode is a field pattern whose amplitude and polarization profiles remain constant along the longitudinal direction of propagation and depends on the operating wavelength, geometry and material of the waveguide. Modes are characteristics where light propagates inside a guided area. Each mode has a propagation constant (β) that represents the light amplitude and phase. The propagation constant (β) is the product of the effective index (n_{eff}) and the vacuum wavenumber (k_o) given by (Snyder and Love, 1983):

$$\beta = k_o \cdot n_{eff} \quad (2.4)$$

where $k_o = \frac{2\pi}{\lambda}$

The effective index, (n_{eff}), is a property of optical components such as optical waveguides. It varies with the wavelength and mode inside the waveguide guiding area. Its value relies on the overall design of the waveguide and is evaluated by Finite Element Method (FEM) that is presented in chapter 3. There are two types of modes: longitudinal modes (parallel to \vec{k}) and transverse modes (perpendicular to \vec{k}). Transverse electromagnetic modes (TEM) have neither electric nor magnetic field in the direction of propagation (z). In a dielectric waveguide, TEM waves cannot propagate, since Maxwell's equations do not allow a non-zero electric field at the boundaries (Pavesi & Guillot, 2006). Therefore, only transverse electric (TE) and transverse magnetic (TM) modes are possible. These two polarizations differ by the non-zero field component in the

z-direction. As shown in figure 2.4, in TE modes or H modes, the electric field (E field) is parallel to the interface. TM modes have only a non-zero E field component perpendicular to the interface, and are also referred to as E modes (Reed, 2008), (Pavesi & Guillot., 2006).

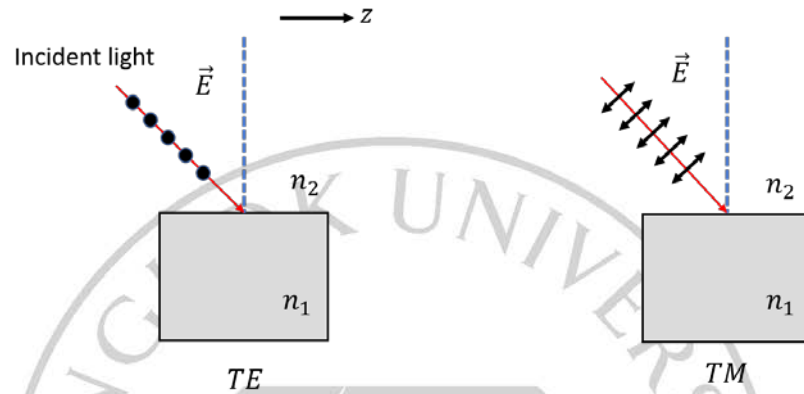


Figure 2.4: Wave representation of TE and TM modes in a planar waveguide (Pavesi & Guillot, 2006)

Based on the Fresnel's equation, the description of reflected and transmitted light at uniform planar interfaces is possible. The reflection coefficients r_{TE} and r_{TM} for the TE and TM polarization are written as follows (Pavesi & Guillot, 2006):

$$r_{TE} = \frac{n_1 \cos \theta_1 - n_2 \cos \theta_2}{n_1 \cos \theta_1 + n_2 \cos \theta_2} \quad (2.5)$$

$$r_{TM} = \frac{n_2 \cos \theta_1 - n_1 \cos \theta_2}{n_2 \cos \theta_1 + n_1 \cos \theta_2} \quad (2.6)$$

Using Snell's law, for incident angles greater than θ_c and an imposed phase shift ϕ of the reflected wave denoted and the equations can be transformed as followed:

$$r = e^{i\phi} \quad (2.7)$$

$$\phi = kz \pm \omega t \quad (2.8)$$

$$\phi_{TE} = 2 \tan^{-1} \frac{\sqrt{\sin^2 \theta_1 - \left(\frac{n_2}{n_1}\right)^2}}{\cos \theta_1} \quad (2.9)$$

$$\phi_{TE} = 2 \tan^{-1} \frac{\sqrt{\frac{n_1^2}{n_2^2} \sin^2 \theta_1 - 1}}{\frac{n_2}{n_1} \cos \theta_1} \quad (2.10)$$

Furthermore, the phase of a wave varies with time (t) and distance (z) and can be quantified by the time and spatial derivation which can be written as:

$$\left| \frac{\partial \phi}{\partial t} \right| = \omega = 2\pi f \quad (2.11)$$

$$\frac{\partial \phi}{\partial z} = k = \frac{2\pi}{\lambda} \quad (2.12)$$

where k is the wavevector or propagation constant of the wavefront and related to the wavelength λ in the medium. In free space k, is referred to as k_0 , whereby k and k_0 are related by the refractive index n of the medium and λ_0 the wavelength in free space which is given by:

$$k = nk_0 = n \frac{2\pi}{\lambda_0} \quad (2.13)$$

Now, light is propagating in z-direction through a planar waveguide with RI n_1 , a height h, a lower cladding n_2 and an upper cladding n_3 . The wavevectors in z (propagation constant β) and y-direction are given as follows:

$$k_z = \beta = n_1 k_0 \sin \theta_1 = [\text{rad/m}] \quad (2.14)$$

$$k_y = n_1 k_0 \cos \theta_1 \quad (2.15)$$

Theoretically, a standing wave is formed by reflection at each interface across the waveguide in x-direction. So, the total phase shift ϕ_t is defined as:

$$\phi_t = 2n_1 k_0 h \cos \theta_1 - \phi_u - \phi_l = 2m\pi \quad (2.16)$$

ϕ_u and ϕ_l are referred as the phase shift at the upper and lower cladding.

Corresponding to the integer m and each polarization there will be a series of discrete angles θ_1 , for which equation (2.16) can be solved and light propagates. Therefore, a discrete transverse field mode is formed in the x and y direction with propagating constants k_z (β) and k_y which describes the velocity and wave propagates in z- and y-direction respectively.

2.1.2 Non-planar Waveguide

Non-planar waveguide is defined as a rectangular waveguide. It can be classified into ridge waveguide, rib waveguide, strip loaded waveguide, immersed waveguide, metal waveguide, and buffered metal waveguide as shown in figure 2.5 (Iizuka,2002). The basic principle of the waveguides is similar. The difference lies in its structure and the optical confinement where the light is trapped in the core which has the higher refractive index. Ridge and rib waveguides (see figure 2.5 (a) and (b)) are similar because these two waveguide structures have a high requirement of surface smoothness. For the strip-loaded waveguide (see figure 2.5 (c)), the strip on the top has a lower refractive index than the core material underneath leading to the confinement of the light in the core material under the strip. The immersed waveguide is totally buried (see figure 2.5 (d)) in the cladding

and it is simple for balanced designing.

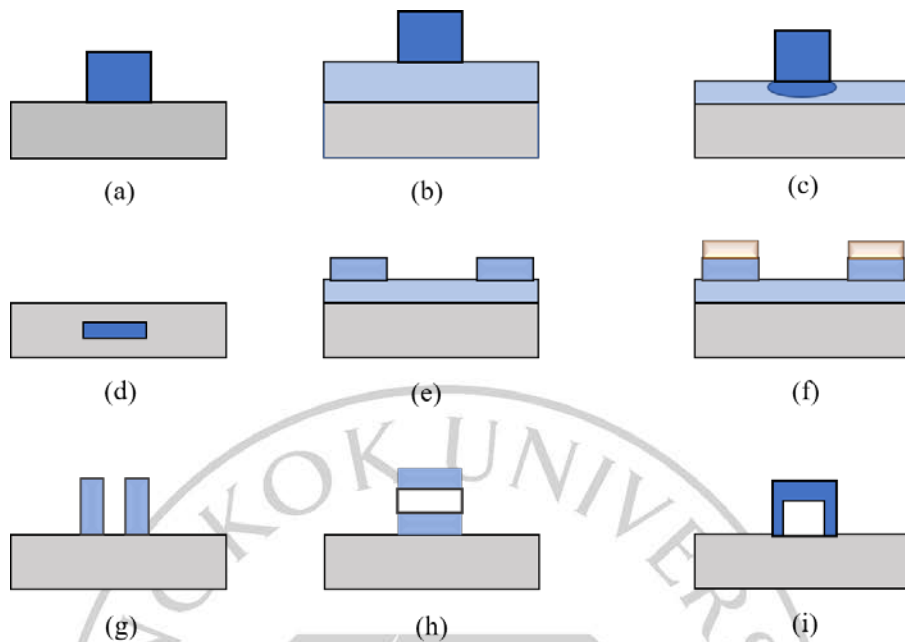


Figure 2.5: Various types of waveguides: (a) ridge waveguide; (b) rib waveguide; (c) strip-loaded waveguide; (d) immersed waveguide; (e) metal waveguide; (f) buffered metal waveguide; (g) vertical slot waveguide; (h) horizontal slot waveguide; (i) hollow waveguide (Iizuka, 2002)

Metal waveguide can be assembled with buffered metal waveguide (see figure 2.5 (e)) i.e., the light is confined in the core material without metal cladding on it. The difference is that there is a dielectric layer between metal and thin film. There exist other kinds of waveguides that confine light in the low refractive index region of the waveguide. It was first discovered and explained by Duguay in 1986 (Duguay et al., 1986).

There are two common structures: slot waveguides and hollow

waveguides, shown in figure 2.5 (g), (h) and (i) separately. Figure 2.5 (g) and (h) show the basic structures for horizontal and vertical slot waveguides. Slot waveguides strongly confine light in a low refractive index region by total internal reflection. For hollow waveguides, they also have a lower refractive core region than cladding. In this case, there is no total internal reflection but leaky waves in the waveguide. The above describes some basic structure of optical waveguide and there are various devices built based on this waveguide types for example: Mach-Zehnder interferometer, directional coupler, micro-ring resonator, etc. (Dell'Olio & Passaro, 2007).

2.2 Losses in an Optical Waveguide

Losses in an optical waveguide is always associated with its design and the quality of the material in any the techniques during fabrication (Reed, 2008). The optical waveguide losses are scattering losses (volume scattering, surface scattering), absorption losses, radiation losses or bending losses and conversion losses or dispersion losses (Pavesi & Guillot, 2006).

Generally, an actual loss L , e.g., an optical return loss, is represented by dB unit given by:

$$L = 10 \exp\left(\frac{I_0}{I}\right) = db \quad (2.17)$$

where I_0 is the initial and I the returned intensity.

For the optical loss L in a photonic structure, an exponential loss coefficient α (loss per unit length) is associated. Here, the intensity at any point z

of the waveguide is given by:

$$I(z) = I_0 \exp(-\alpha z) \quad (2.18)$$

where I_0 is the initial intensity at the distance $z = 0$. Combining equation (2.19) and (2.20) leads to the attenuation coefficient α (equation (2.21), which is involved in all the different loss mechanisms. It is given by:

$$L = 10 \log \left(\frac{I_0}{I} \right) = 10 \log [\exp(\alpha * z)] \quad (2.19)$$

$$L = 10 \log(e) * \alpha * z \quad (2.20)$$

$$\alpha = 4.34 * \alpha' = \text{dbcm}^{-1} \quad (2.21)$$

Here, the loss is expressed in dB/cm which is $4.34 * \alpha'$, whereby the unit for α' is cm^{-1} . The most accepted range for loss is of the order of 1 dB cm^{-1} (Reed, 2008).

Scattering in an optical waveguide can result from surface scattering and volume scattering. Volume scattering is caused by imperfections in the bulk material of the waveguide, e.g., crystalline defects. In the bulk material, Rayleigh scattering is the dominant loss mechanism that exhibits a λ^{-4} dependence and in the case of wavelengths longer than the correlation length a λ^{-3} dependence can be observed.

Furthermore, the interband absorption and free carrier absorption are the two sources of absorption losses in the waveguides (Reed, 2008). Here, the material of the waveguide design acts a major role. In case of photon absorption,

an electron excitation occurs from the valence to the conductive band. For example, the wavelength band of Si (Silicon) is approximately $1.1\mu\text{m}$, above which Si acts as guiding layer and below it displays a strong absorption property.

However, radiation losses are caused by the dissipation of the energy in the guided mode that goes into the upper and lower cladding. To avoid the radiation losses, optimization in the fabrication process of the photonic structure with correct radius of curvature is recommended. Theoretical analysis reports that the radiation loss coefficient depends exponentially on the radius of the bend (Miller, 1964). In most typical dielectric waveguide structures, radiation losses occur due to the minimum bending radius (Goell, 1974).

2.3 Waveguide Materials

There exist multiple materials available for fabricating optical waveguides. From Si and its compounds such as SiO_2 , SiC, SiN, SiON to the various polymers such as PDMS, SU-8, Photosensitive resin and etc. The key parameters for designing optical waveguide are, its properties of materials (refractive index), its optical transparency range, optical loss, fabrication feasibility, and mechanical property (Hunsperger,1995).

2.3.1 Material Properties

2.3.1.1 Optical Properties

An electromagnetic wave can be described in different ways i.e., by energy (eV), by wavelength (λ), by frequency (Hz). The relationships between

these three different units are given by:

$$E = hc/\lambda \quad (2.22)$$

$$v = c/\lambda \quad (2.23)$$

where h is a constant and its value is $6.62607015 \times 10^{-34}$ *joule second*.

Furthermore, the properties involved are described below:

- (a) **Refractive index:** When designing a waveguide, the refractive index is a dominating factor. The reason is that if the waveguide is used to transmit light/energy, high refractive index leads to a better confinement of light in the core region. In addition, if the waveguide is used for sensing applications, especially in case of evanescent sensing, it is necessary to keep a certain amount of light outside the waveguide core region. Then it is best to choose a refractive index difference when designing the waveguide (Melloni et al., 2009).
- (b) **Loss:** Another important factor to consider for optical waveguide is the optical loss characteristics. There are three different types of losses involved in the optical waveguide. They are: scattering, absorption, and radiation. For designing a waveguide, the main losses involved is scattering and absorption. The scattering losses is highly observed in dielectric waveguides and the absorption in semiconductors and other crystalline materials (Hunsperger, 1995).
- (c) **Transparent range:** This is another factor which determines the light to be used in the waveguide where there is low absorption rate. Therefore, it is

necessary to choose the proper wavelength according to materials which can reduce unnecessary optical losses.

- (d) **Mechanical properties:** The mechanical properties need to be considered because of the process for depositing layers of different materials in waveguide fabrication. When this process is implemented, a stress is induced by temperature which may lead to cracks in the layer. Therefore, the fabrication process must design and optimize the parameters to avoid such problems.
- (e) **Fabrication feasibility:** The fabrication feasibility of material to the substrate is a key element for optical waveguides. The fabrication needs to ensure repeatability and stability. These process sequences are crucial factors when designing a waveguide.

2.3.1.2 Typical Optical Waveguide Materials

There are various materials used for fabricating waveguides. In this section, a brief description of different types of materials for waveguide fabrication is presented. Silicon is the basic material that is widely used in fabricating waveguides. It is an important material for its good micromachining property and is used for huge number of applications. It is transparent to infrared light with wavelength above $1.1\mu\text{m}$ and has a high refractive index of ($n=3.5$) (Hoffmann & Voges, 2002).

The other types of materials that is used for fabricating waveguides are discussed below.

- (a) **Porous silicon:** It is a spongy nanoscale composite structure with a pore

dimensions ranging from below 2nm and above 50nm. With an effective refractive index between air and silicon, they can easily be fabricated in multilayer structures (Tong, 2016). The fabrication method for such waveguide involves electrochemical etching in hydrofluoric acid (HF) (Ohji et al., 2000). The porosity of the silicon (Si) wafer relies on the refractive index (Theiss, 1997). The refractive index of the porous layer of silicon ranges from 3.4 to 1.0. The theoretical and experimental results of porous silicon waveguide biosensors by surface plasma resonance (SPR) displays a high sensitivity (Saarinen et al., 2005).

- (b) **SiO₂ (Silicon dioxide):** Here, SiO₂ acts as an isolation layer between the waveguide and Si for preventing a leakage of optical signal. The different methods to fabricate SiO₂ are: thermal oxidation, Atmospheric Pressure Chemical Vapor Deposition (APCVD), Plasma-enhanced Chemical Vapor Deposition (PECVD) and Low-Pressure Chemical Vapor Deposition (LPCVD). Moreover, the refractive index of SiO₂ ranges from 1.44 to 1.47 and it depends on the type of fabrication used.
- (c) **SiC (Silicon carbide):** SiC is another material used for fabricating waveguides. There is single crystal, poly, and amorphous SiC. The commonly used are poly SiC and amorphous SiC. There are different ways to grow silicon carbide including APCVD, LPCVD, PECVD, etc. APCVD and LPCVD are usually used to deposit poly-SiC at high temperatures, above 800⁰C, whereas sputtering and PECVD are employed to form amorphous SiC at lower temperature, below 700⁰C (Arrand et al., 1998).

- (d) **ZnO** (Zinc oxide): ZnO is a semiconductor material with a wide broad-band gap of 3.4eV. It is transparent in a visible range and is characterized by a high value of the refractive index, $n \approx 2$ (Struk et al.,2009), which is an important feature of the waveguide for applications in integrated optics (Struk et al., 2014). The fabrication of the waveguides based on using ZnO material can be done using spin coating (Mohan, 2015) and magnetron sputtering (Wu et al., 1989), etc.
- (a) **SU-8**: It is a commonly used epoxy-based resin (Bêche et al., 2004). Since SU-8 has good optical transparency, it has been used as the waveguide material in various integrated optical systems (Pelletier et al., 2007). It can be mass-produced via polymer molding also called UV-LIGA process (Shew et al., 2008). The refractive index of SU-8 is highly dependent on the processing temperature, so that the core and cladding of the waveguide can all be fabricated from SU-8 with different treatment (Hsieh et al., 2005).
- (b) **PDMS**: Polydimethylsiloxane (PDMS) is an optical material with excellent optical and elastic properties. It shows high transparency in the spectrum range, and it is formable by imprinting techniques (Gaso et al., 2014). In the field of PDMS based optical waveguides there are two approaches for fabrication process, i.e., (1) where the index contrast between the core and cladding is generated by curing the same material at different temperatures (Chang et al., 2005) and (2) it comprises two distinct materials for the core and cladding for curing process (Neyer et al., 2005). Generally, the typical method for fabrication process is to first construct the patterned channel and then fill

the channel with a higher-index material such as PDMS. This is later cured at different temperatures or by using a UV curable resin placed in a UV chamber (Hosseinkhannazer et al., 2008).

2.4 Polymer-Based Waveguide

Since polymer resin materials have attracted a lot of attention in micron scale, nanotechnology and in optical network applications due to their unique properties, it has the capacity to produce them at low cost (Shen et al., 2009). Based on these advantages, this work considers fabricating and designing waveguide based on polymer resin material and it will be discussed in Chapter 4.

Polymer-based waveguide offers the possibility of low-cost fabrication and soft lithography replication (Chiang, 2010). It is considered as a promising candidate to address the requirement of optical interconnects especially on the board level and card-to backplane level (Glebov et al., 2007). The use of polymer has increased the compatibility with printed board circuits and flexible substrates (Dou et al., 2010). It has a large transparent operating window from the visible to infrared spectrum range that is compatible for a wide range of applications. Polymer material can also be synthesized to give rise to a special characteristic, such as thermo-optic effect (Wang et al., 2006), electro-optic effect (Shi et al., 2000), photochromic effect (Rodriguez et al., 2001), and light emission (Friend et al., 1999).

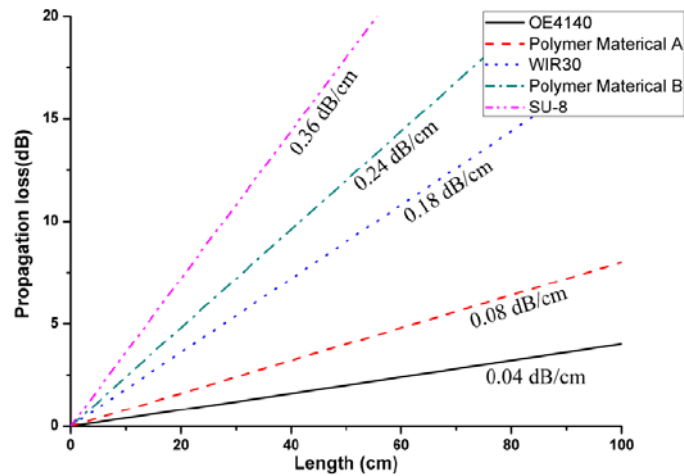


Figure 2.6: Propagation loss of various polymer waveguides with different polymer materials at difference length (Bamiedakis et al., 2009; Wang et al., 2010; Kim et al., 2003; Jiang et al., 2013 and Papakonstantinou, 2008)

The quality of the polymer waveguides that used to form the transmission medium is very important to a polymer-based optical link technology and is characterized by the optical propagation loss of the polymer waveguides (Hashim et al., 2011). Figure 2.6 shows a comparison of the propagation losses of several reported polymer waveguides with different polymer materials at 850 nm wavelength. The polymer material OE4140 that is reported are taken from Dow Corning (Bamiedakis et al., 2009), WIR 30 Series from ChemOptics (Wang et al., 2010), SU-8 from MicroChem (Kim et al., 2003) and other polymer materials (Jiang et al., 2013) and (Papakonstantinou, 2008). From the above data, a conclusion can be drawn that polymer-based waveguide offers low loss for optical interconnect applications.

2.4.1 Fabrication Techniques For Polymer-Based Waveguides

In this section a brief explanation of fabrication techniques of polymer-based waveguides is presented. The conventional methods involved have been well documented and reported in open publication (Eldada et al., 1996) and will not be detailed here. In this section, 3D printing DLP technology is discussed in detail and reports its advantages for fabricating the micron scale structures based on polymer materials since our work focuses on this technique.

Polymer waveguide devices can be fabricated by various techniques. Such techniques include laser direct writing, reactive ion etching (Eldada et al., 1996), electron-beam lithography (Wong & Pun, 2001), photolithography (Tung et al., 2005), soft lithography (Rogers & Nuzzo, 2005) and 3D printing DLP technology (Swargiary et al., 2020). The following mentioned techniques are briefly described below:

Laser direct writing offers a rapid prototyping without a process of a mask production (Eldada & Shacklette, 2000), however it has a limitation for writing speed and materials selection.

Reactive ion etching involves many processing steps and it is very complex and time-consuming fabrication method. It is a technique used in microfabrication process (Eldada et al., 1996).

Electron-beam lithography is a technique that is specially used for high-resolution micro-nano structures fabrication process which are time consuming and expensive.

On the other hand, photolithographic process has advantageous over these techniques, which is a powerful and dominant technique for microfabrication and is suitable for radiation-sensitive materials such as photoresists on flat glasses or semiconductor surfaces.

Soft lithography is a non-photolithographic microfabrication method. It uses a stamp or mold to generate microstructures, making it a fast and inexpensive technique. It can be used for three-dimensional structure has been the most widely used material because of its biocompatibility, low toxicity, durability and mechanical flexibility.

In this work, a waveguide based on polymer of dimension (few micrometers) is fabricated by 3D printer based DLP technology which offers an alternative fabrication scheme (Swargiary et al., 2020). This technique can develop an optical integrated waveguide by printing multiple active components as one object with an easier way (Holtrup, 2015). Since 3D printing DLP technology is employed in this work, emphasis is given to this technique. A brief description of this is provided in the next section.

2.5 3D Printing DLP Technology

3D printing is a promising technology used for making micron scale products in the future. It has the potential to manufacture products that are not possible to build with other techniques (Hopkinson et al., 2005). A promising method is 3D DLP printing which is an additive manufacturing technique that employs rapid prototyping of any object (Huang et al., 2017). This is one of the

vat polymerization SLA (Stereolithography) technique that works by projecting images to a polymer resin in layered fashion (Bogue, 2013). This technology uses a UV (ultra violet) light source that projects light on a Digital micromirror Device (DMD), which reflects the light with millions of microscopic mirrors resulting in an image formation. On the spot where the image projects, a photo polymerization process is formed and thus cures the polymer resin. In the DLP printers, a photopolymer resin is used as its material. This resin is composed of monomers, oligomers and additives/photoinitiators (Ali & Jianyong, 2019). Finally, by moving the build platform, a new layer is cured and a 3D product is obtained when the process is completed.

2.5.1 DLP Technology

In general, the concept of 3D printing technology was first described in 1986 by Charles W. Hull (U.S. Patent 4,575,330A). This concept was named as SLA (Stereolithography), that prints multiple layers by ultraviolet light to create 3D structures. In recent years, with the development of AM (additive manufacturing) technology and material science, various 3D printing methods have emerged.

As discussed in Chapter 1, there are two common types of 3D printing methods. These include, nozzle-based and light-based 3D printing technology. For the nozzle-based printing, the materials are extruded and deposited (printed) onto the print platform. For the light-based printing, DLP technology, laser assisted printing, selective laser melting (SLM), and selective laser sintering (SLS)

are its types.

Table 2.1: Comparison of various 3D printing technologies

Properties	Materials	Printing process	Resolution (μm)	Speed
(Nozzle based printing) Extrusion	Thermoplastic polymer	Serial (line by line)	50	Slow ($\mu\text{m/s}$)
(Nozzle based printing) Inkjet	Thermoplastic polymer	Serial (drop by drop)	50	Medium (mm/s)
(Light based printing) DLP	Photosensitive polymer	Continue plane (layer by layer)	6	Fast (mm^3/s)
(Light based printing) Laser assisted	Photosensitive polymer	Serial (dot by dot)	~ 1	Medium (mm/s)
(Light based printing) SLS/SLM	Metals, ceramic and polymer	Serial (dot by dot)	80	Slow ($\mu\text{m/s}$)

The DLP and laser assisted printing methods work using photopolymerization reactions. During the process of SLM and SLS, material powders are melted and reshaped at high temperatures which are induced by a laser. These various types of 3D printing platforms have significant differences and properties in printing mechanism, speed, material selection, and its resolution (Ngo et al., 2018), (Ligon et al., 2017). A comparison between DLP printing technology and other 3D printing technologies are shown in Table 2.1.

When DLP 3D printing technology was first invented in 2006, the researchers successfully manufactured 20 μm structure (Ngo et al., 2018) and in 2013, Yi *et al.* fabricated structures with various topologies. The resolution of DLP

3D printing partially depends on the selected material. When the 3D structures are printed using polyethylene glycol diacrylate (PEGDA MW = 700 da) solely, the XY resolution of the structure nearly reached $6 \times 6 \mu\text{m}$. On the other hand, the resolution is about $17 \mu\text{m}$ with bio-ink containing 10% gelatin-methacrylate (GelMA). It has been also reported that Dai *et al.* used a high precision DMD (each micromirror is $10.8 \mu\text{m}$) to build the projection-based 3D printing platform. Saha *et al.* combined the advantages of two-photon lithography (TPL) with DLP printing method to develop a femtosecond projection TPL (FP-TPL) technique. By this method, complex 3D structures of 500nm feature size can be printed rapidly (Saha et al., 2019).

Recently, a faster DLP 3D printing method which is computed axial lithography, has been developed (Kelly et al., 2019). Using this method, light is reflected onto the photosensitive material in the form of a 2D image and generates energy causing the material to change into the originally designed 3D structure. This offers a relatively large additive manufacturing volume and works faster than conventional 3D printing methods.

The materials for 3D printing DLP technology are photosensitive polymers which transforms into solid from liquid when exposed to UV light. The monomers are photoinitiator of this polymer and it emits harmful vapors. For that, researchers have modified some polymer materials to non-toxic and harmless and can be used for DLP-based 3D printing. Photopolymer such as PEGDA and GelMA are widely used specially for bioprinting applications as it holds good polymerization process and offer biocompatibility. Furthermore, it is always

recommended to use biocompatibility and non-toxic photosensitive polymers for 3D DLP printing to avoid health hazards. With the favorable properties, such as: printing speed of the printer, accuracy, and materials, DLP 3D printing technology has great benefits for the rapid fabrication of precision products.

DLP technology is a new way to project and display information (Holtrup, 2015). This technology was developed by Texas Instruments for applications such as: projectors, spectroscopy, 3D scanners, integrated optical devices, machine vision, head-up displays and medical applications, (Texas Instruments, 2015).

This method uses a set of chips based on optical micro-electromechanical technology to process the UV light to photosensitive materials as shown in figure 2.7. The main part is a Digital Micro Mirror Device which consists of a matrix of millions of microscopic mirrors. These mirrors rotate to control the path of light and then project onto the photosensitive resin vat during the printing process. The pixels of the micromirror are only a few microns. Thus, the DLP technique has a relatively high resolution (15-100 microns), which is at the micron scale (Ngo et al., 2018), (Zhang et al., 2020). When light is projected onto the vat of polymer resin using DLP technology, the entire layer is printed immediately at once. Hence, with this technology fast printing can be achieved (Lu et al., 2006), (Ngo et al., 2018).

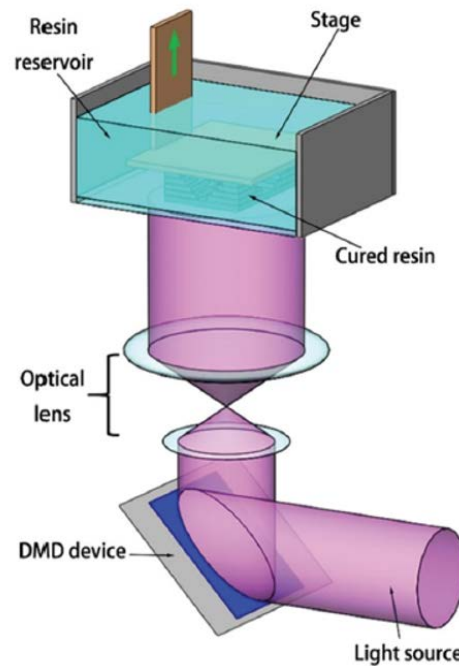


Figure 2.7: Schematic diagram of the DLP based 3D printing technology (Ngo et al., 2018)

The biggest advantages compared to other techniques is curing of whole layer at once. This reduces the errors in the XY-plane and limits the mechanical movements. The resolution of 3D printed parts using DLP printing technique is considered to be very high and smooth surface finishing (Kadry et al., 2019). Since in DLP printing, the diameter of vertical oriented objects is smaller, the supports are a lot thinner than in FDM technology (Holtrup, 2015).

The photopolymer resins that are used for DLP printing are quite expensive (around €80 per liter) and the shelf life of the material is limited (around 1 year depending on the manufacturing company) (Kadry et al., 2019). The build size is limited to the power of the light source and the area of the projection onto the LCD. Generally, in most of the DLP printers, the build size is between

50x40mm to 100x80mm and the cost of a DLP printer is more than 50% higher than standard FDM printers, although not as expensive as SLS or 3D inkjet printers. DLP printing also uses very bright UV light, which is harmful to the eyes henceforth, protection is required.

2.5.2 Materials for DLP-Based 3D Printers

The materials used for the DLP based 3D printers are photopolymer resin which is very sensitive to the ambient light. They can change their state from liquid substance to solid substance during photopolymerization. Only the area exposed to UV-light hardens and the unexposed parts remain liquid. Some of the common type of polymer bases for photopolymers are polyvinyl cinnamate, polyamide (PA), polyisoprene, polyimides, epoxies, acrylics etc. Photopolymers, are also referred to as photopolymer resins or UV resins and they are based on epoxy and acrylic chemistry. Usually monomers, oligomers and additives are also used along with the photopolymers which can be selectively polymerized and crosslinked upon image-wise exposure by light radiation such as UV light (Sheridan, 2013).

2.5.3 Photopolymerization

Photopolymerization is the processes of using photosensitive photopolymers as their main materials. These photopolymers react while exposing to the UV light and it undergoes a chemical reaction to become solid (Gibson et al., 2015).

Photopolymers were developed in late 1960's and it became quickly popular in wide range of commercial sectors. In the mid 1980's, Charles Chuck Hull developed a similar type of laser printers by using a UV curable material by exposing them to a scanning laser. By curing one layer over another layer, a solid 3D part was fabricated (Gibson et al., 2015). This was the beginning of stereolithography technology which is later the concept was also known as DLP technology.

There are various types of radiation used to cure commercial photopolymers that includes gamma rays, X-rays, electron beams, UV light and visible light (Gibson et al., 2015). In DLP systems, UV light radiation are used most commonly. There are basically two types of reaction mechanisms during curing process of photopolymer resins. They are, the cationic polymerization through epoxy groups and free radical polymerization through double bonds for example (Meth)Acrylate. In the cationic curing (epoxides, vinyl ethers etc.), a photo initiator is exposed to light and with the right amount of energy, it releases a Lewis acid. These acids react with epoxy groups and results in polymerization (Crivello & Reichmanis, 2014).

2.5.4 Monomer and Oligomers

In photochemistry-based 3D printing, printable materials are mainly composed of monomers, oligomers, and photoinitiating systems (Xing et al., 2015). During the 3D printing process, radicals or cations are produced by a photochemical reaction under light irradiation which reacts with monomer and

oligomer units. Monomers and oligomers can be photopolymerized (in the presence of suitable photoinitiators) during the 3D printing process and displays the final properties of the 3D printed objects or structures.

There has been reports that the combinations of commercial monomers have been used for 3D printing. For example, a combination of Sartomer (CN2920 & CN981) and trimethylolpropane triacrylate, are used for continuous liquid interface production of 3D objects (Tumbleston et al., 2015). However, not all the commercial photopolymerizable monomers, oligomers can fulfill the properties of the 3D printed objects. For these reasons, it is needed to design and develop the monomers and oligomers for 3D printing. This is done by modifying it with required properties (Zhang & Xiao, 2018). Many monomers, oligomers are used in 3D printing. One such type is the acrylates that has a property for curing faster and these are used mostly for rapid prototyping. In Appendix B, Table B.1 describes curing properties for various acrylic monomers (3Dprinter.wikidot, 2011) (Idacavage, 2012) and in Table 2 of the Appendix B, properties of oligomers are shown.

2.5.5 Photoinitiators

The photoinitiator converts the physical energy of the incident light into chemical energy. It exhibits a strong absorption at the laser emission wavelength, and undergoes a fast photolysis to generate the initiating species (Decker C, 1995). With these behaviors, they can generate radical polymerization, or reactive cationic species that can initiate polymerization among the epoxy molecules

(Crivello & Dietliker, 1998).

Photoinitiators are very sensitive to specific wavelengths. The peak absorbance of the chosen photoinitiator must match with the projected light that will be used in the photopolymer-based 3D printer. In the presence of specific liquid monomers, photoinitiators generate reaction intermediates that give rise to the production of solids from liquids, (i.e., polymerization). There are two types of photoinitiators, Type I photoinitiators which produce reactive intermediates directly after light absorption and Type II photoinitiators are the type requiring a second compound, i.e., co-initiator, to produce such reaction intermediates.

A variety of commercially available UV-light-sensitive photoinitiators used in 3D printer applications are shown in Table 2.2 and it can be used in the photopolymer-based 3D printers with UV light as the irradiation source.

During the UV light exposure (delivered from the 3D printer), commercial photoinitiators as given in the Table 2.2. TPO, BAPO, Irgacure 184, and Irgacure 369 (Ganster et al., 2008) and (Schafer et al., 2004), inhibits free radical photopolymerization of the resin for 3D printers. This effect can thus enable the continuous formation of a solid-liquid interface and avoid the traditional 3D printing process based on the step-by-step or layer-by-layer fashion printing. Thus, it can accelerate the 3D printing processes (Tumbleston et al., 2015).

Table 2.2: Commercial UV- light sensitive photoinitiators for 3D printing

Photoinitiators	Light absorption (λ)
 TPO	~ 380 nm
 BAPO or Irgacure 819	~370 nm
 Irgacure 184	~246 nm
 Irgacure 369	~324 nm

2.5.6 Photopolymer

The photopolymer used in this work is Hex-polymer (PX-8880) and Monocure 3D rapid clear resin. Both the resins have significant suitable properties that meet the aforementioned points as discussed above. These polymers are very sensitive to ambient light and their polymerization falls between 225nm to 420 nm. It provides detailed objects with high precision and excellent accuracy (given in Appendix C). Both resins are optimized to work for the low power 3D printers that works with DLP technology. In this work, two types of resin are chosen for the 3D printer based on DLP technology (Wanhao Duplicator D7 Box) which uses UV light. The details of the DLP printer used in this work are provided in Chapter 4.

Both the resin is in the liquid form when purchased from Sync Innovation 3D printing Company, Thailand (Hex-polymer PX-8880 and Monocure 3D rapid clear resin). It has an excellent speed, precision and toughness. This resin is specially made for 3D DLP printer technology which possess different optical and physical properties. The physical and optical properties of Hex-polymer PX-8880 and Monocure 3D rapid clear resin is shown in Table 2.3.

Table 2.3: Property parameters of photopolymer resin

Resin	Viscosity	Color	Refractive index	Spectrum	Shore hardness	Toughness performance
Hex-polymer PX-8880	500 CPS (25°C)	Extremely transparent (clear)	1.4759	365~420 nm	85D	Light and tough (rigid)
Monocure 3D rapid clear	(500-600) CPS	Extremely transparent (clear)	1.5017	225~420 nm	70D	Light and tough (rigid)

These are the properties in general for the resin that is used in this work. But apart from these, the polymer resin material has one more interesting property, i.e., swelling characteristics. This property of polymer attracted researchers to implement in various applications. One of the applications is development of an optical waveguide as a sensor for the detection of different alcohol solutions based on its swelling behavior (Nagata et al., 2007).

This behavior of the polymer resin relies on the concentration of the alcohols and water molecules (Muto et al., 2003). It has been reported a polymer material named: Poly-ethylen-vinyl-alcohol (PEVA: $n=1.495$) and Novolac resin ($n=1.61$) swells when it is revealed to alcohol solutions. These polymers were used as a sensing layer in the POF (plastic optical fiber) where it was coated on the waveguide core, resulting in a decrease in the cladding index of refraction than the core. Thus, the sensor changes from leaky to guide type and helps in alcohol

detection by measuring the intensity at the output area (Morisawa et al., 2001), (Muto et al., 1998).

On the other hand, certain rubber-type polymers namely, Polyisoprene, when immersed in alkanes cause swelling (Uchiyama et al., 1997). He reported that, to check the changes in index of refraction by polymer swelling behavior, in acetone solution, the film is soaked instead of alkane as the acetone concentration in water is easy to control. Figure 2.8 shows the temporal change in refractive index of the film measured using Abbe's refractometer, that is equivalent to the acetone concentration.

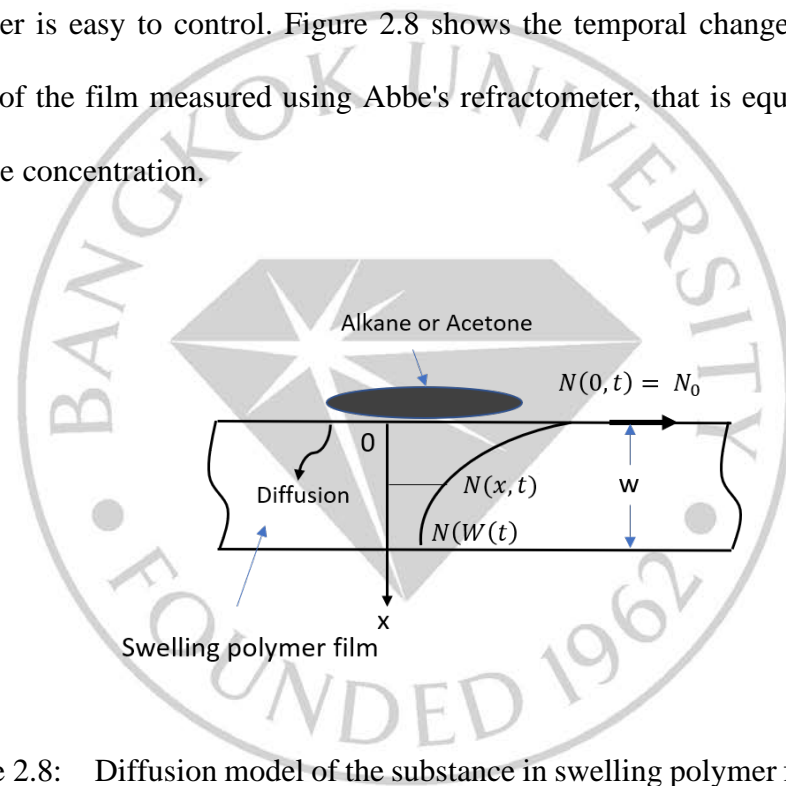


Figure 2.8: Diffusion model of the substance in swelling polymer film (Muto et al., 1998)

The refractive index changes from $n_D = 1.52$ to 1.47 . These attributes are investigated theoretically and the model displayed in figure 2.8. When small amount of substance is poured in the surface of the film, its concentration, $N(x, t)$ at position x from the surface at time t is given by the following one-dimensional

diffusion equation:

$$\frac{\partial N(x, t)}{\partial t} = D \frac{\partial^2 N(x, t)}{\partial x^2} \quad (2.24)$$

where D is a diffusion coefficient.

Assuming the initial condition of $N(x, 0) = 0$ and $N(0, t) = N_0$, the solution of Equation 2.24 is converted as:

$$N(x, t) = N_0 \left(1 - \frac{2}{\sqrt{\pi}} \int_0^{\frac{x}{2\sqrt{Dt}}} e^{-\omega^2} d\omega \right) \quad (2.25)$$

As the reduction of the polymer density by swelling is almost proportional to the value of $N(x, t)$, the index of refraction of the film $n(x, t)$ at x and t decreases with increasing $N(x, t)$. Therefore, $n(x, t)$ is given as follows:

$$n(x, t) = \frac{n_0 n_\infty}{(n_0 - n_\infty)N(x, t) + n_\infty} \quad (2.26)$$

where n_0 is the initial value of the refractive index at $N(x, 0)$ and n_∞ is the final value at $N(x, \infty) = N_0$. By substituting the equation 2.26 in equation 2.25, the temporal change in the index of refraction of the polymer swelling film is acquired.

Furthermore, the swelling mechanism of the polymers and its operation can be investigated by ray tracing method as reported by *Muto et al.* Here, the POF sensor portion is coated by the polyisoprene film and is operated as a layer of cladding in the core with 1mm diameter and moderately lower index of refraction comparing to polyisoprene. The core fiber, nonbornene polymer, ARTON™ (Fujitsu

Chemical Ltd.; $n_D = 1.510$) was used. The swelling mechanism analysis is shown in figure 2.9.

In this model, it is demonstrated the reduction of the index of refraction in the polymer cladding portion shows a change in the fiber structure from leaky to guided type which makes the transmitted light intensity to increase remarkably. With the ray tracing method, it is demonstrated that under the condition of $n(W, t) \geq n_1$, the sensor head operated as a leaky waveguide and then a small part of the ray power $P(\theta)$ is reflected from the boundary of core and clad with the reflection coefficient $r(\theta)$ determined by $n(W, t)$, n_1 and the ray angle θ .

The output power is then given by:

$$P(out) = \sum_{\theta=0}^{\theta_c} P(\theta)r^m(\theta) \quad (2.27)$$

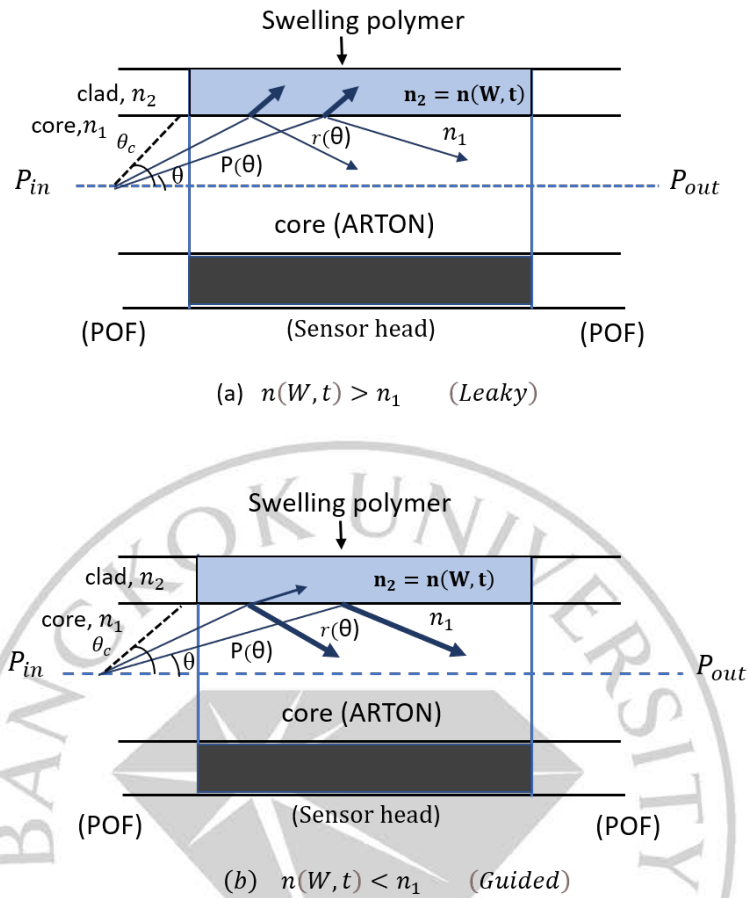


Figure 2.9: Swelling mechanism by ray tracing model (Muto et al., 1998)

where $\theta_c = \frac{\pi}{2} - \cos^{-1}\left(\frac{n_2}{n_1}\right)$ is the critical angle in the input-side POF and “m” is the number of reflections from the core diameter and length of the sensor head. On the other hand, when $n(W, t)$ becomes lower than n_1 by swelling process, the sensor head changes to the guided structure. So, in this case, the total output power is given by:

$$P(out) = \sum_{\theta=0}^{\theta_{cs}} P(\theta) + \sum_{\theta=\theta_{cs}}^{\theta_c} P(\theta) r^m(\theta) \quad (2.28)$$

where $\theta_{cs} = \frac{\pi}{2} - \cos^{-1} \left(\frac{n(W,t)}{n_1} \right)$ is the critical angle in the sensor head.

With these theoretical investigations, the swelling characteristics of the polymer resin can be analyzed and can be used as an application in the sensor field. There are very limited literatures on this mechanism. But taking this property of polymer resin, one such type of application is implemented in our study which is presented in Chapter 5.



CHAPTER 3

NUMERICAL METHODS

This chapter provides the evaluation of waveguides theoretical investigation with a review of Maxwell's Equations and its forms. For solving the light propagation in the waveguide, there exist a several numerical techniques to solve them. The Maxwell's Equations are essential for understanding EM field propagation inside the optical structures. The traditional analytical techniques fail to completely design the waveguide devices. For that, the numerical methods show an advantage to solve a solution. A number of numerical methods for example, Finite Difference Method (FDM), Finite Difference Time Domain (FDTD), and Finite Element Method (FEM) are discussed briefly. The advantages of FEM over supplemental techniques, the FEM's elemental theory and the investigation of the fundamental mode of the desired waveguide structure are also presented prior to the fabrication process and experiment testing.

3.1 Basic Equations

The evaluation of the optical waveguides demonstrates the process of uncovering the field profiles of the modes that can propagate in the waveguides. For the FEM application in the evaluation of optical waveguide and investigation of the characterization of propagation, the supplemental electromagnetic field (EM) equations are examined. In particular, the Maxwell's equations along as well as its boundary conditions are taken into account.

3.1.1 Maxwell's Equation

The supplemental equations, in particular Maxwell's Equations forms the foundation of EM theory. These are the four sets of partial differential equations that represents the EM wave laws.

In the Maxwell's Equations, the four vectors quantities are: the electric field intensity **E** (Volts/meter), the magnetic field intensity **H** (Amperes/meter), the electric flux density **D** (Coulomb/meter²) and the magnetic flux density **B** (Tesla). The time independent fields are in differential or integral shape for free source. The differential shape of Maxwell's equations is given as:

$$\nabla \times \mathbf{E} + \frac{\partial \mathbf{B}}{\partial t} = 0 \quad (\text{Faraday's law}) \quad (3.1)$$

$$\nabla \times \mathbf{H} = \frac{\partial \mathbf{D}}{\partial t} + \mathbf{J} \quad (\text{Ampere's Circuital law}) \quad (3.2)$$

$$\nabla \cdot \mathbf{D} = \rho \quad (\text{Gauss's law}) \quad (3.3)$$

$$\nabla \cdot \mathbf{B} = 0 \quad (\text{Gauss's law for magnetic}) \quad (3.4)$$

where **J** is the current density and ρ is the electric charge density (coulombs per cubic meter).

For non-conductive and isotropic media, **E** and **D** and **B** and **H** are related by the constitutive relation which can be written as:

$$\mathbf{D} = \epsilon \mathbf{E} \quad (3.5)$$

$$\mathbf{B} = \mu \mathbf{H} \quad (3.6)$$

where ϵ and μ is permittivity and permeability of the medium and it is given as:

$$\epsilon = \epsilon_0 \epsilon_r \quad (3.7)$$

$$\mu = \mu_0 \mu_r \quad (3.8)$$

Here, ϵ_0 is permittivity of the free space and ϵ_r is relative permittivity of the vacuum. And μ_0 is permeability of the free space and μ_r is relative permeability of the vacuum respectively.

EM waves carry an energy when travelling in an empty space. The electric and magnetic fields is associated with an energy density and the amount of energy flow per unit area is given as:

$$S = E \times H \quad (3.9)$$

The above equation is Poynting vector and it is a vector product. It is the cross product of the electric and magnetic fields. Its unit is given by W/m².

3.1.2 Boundary Conditions

Boundary conditions are essential at a boundary surface for separating two media with different material parameters: in particular, permittivity and permeability (medium 1 and medium 2). In the given figure 3.1, the normal vector \mathbf{n} , is lead from medium 1 to 2. Then the boundary conditions surface currents ($J=0$) and surface charges ($\rho=0$) are given as:

- 1) The electric field are continuous for the tangential components. So,

$$\mathbf{n} \times (\mathbf{E}_1 - \mathbf{E}_2) = 0 \quad (3.10)$$

Therefore,

$$E_{1t} = E_{2t}$$

- 2) The magnetic field are continuous for the tangential components. So,

$$\mathbf{n} \times (\mathbf{H}_1 - \mathbf{H}_2) = 0 \quad (3.11)$$

Therefore, $H_{1t} = H_{2t}$

3) The electric flux is continuous for the normal component and it is given as:

$$n \cdot (D_1 - D_2) = 0 \quad (3.12)$$

Therefore, $D_{1n} = D_{2n}$

4) The magnetic flux density is continuous for the normal component and it is given as:

$$n \cdot (B_1 - B_2) = 0 \quad (3.13)$$

Therefore, $B_{1n} = B_{2n}$

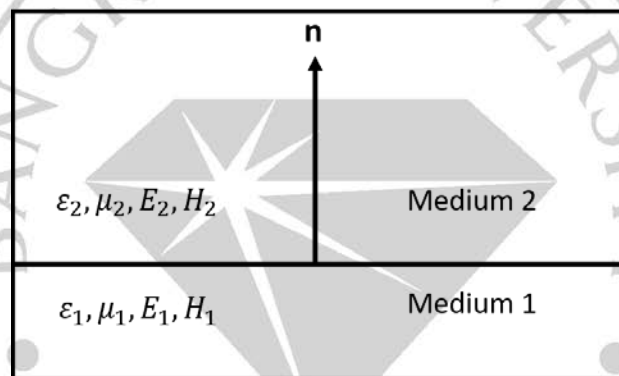


Figure 3.1: Index of refractive medium of the boundaries between two medias with \mathbf{n} as the unit vector

When one medium transforms to a perfect electric conductor, an electric wall boundary condition occurs and is displayed below:

$$\mathbf{n} \times \mathbf{E} = 0 \quad \text{or} \quad \mathbf{n} \cdot \mathbf{H} = 0 \quad (3.14)$$

This condition establishes the normal component continuity of the electric field vector, \mathbf{E} , and the magnetic field vector, \mathbf{H} .

Likewise, when one medium transforms to a perfect magnetic

conductor, a magnetic wall boundary condition occurs and is displayed below:

$$n \times H = 0 \quad \text{or} \quad n \cdot E = 0 \quad (3.15)$$

The above equation offers that the electric field \mathbf{E} diminishes by ensuring the progression of the magnetic field, \mathbf{H} normal component in the boundary.

3.1.3 Wave Equations

The two important results of Maxwell's Equations are the wave equations and the EM waves. If we consider the regions, both the charge density ρ and current density \mathbf{J} diminishes and it can be assumed that the medium is a homogenous as well as isotropic. Hence, the wave equation for the field vector \mathbf{E} is given as:

$$\nabla^2 \mathbf{E} - \mu\epsilon \frac{\partial^2 \mathbf{E}}{\partial t^2} + (\nabla \ln \mu) \times (\nabla \times \mathbf{E}) + \nabla(\mathbf{E} \cdot \nabla \ln \epsilon) = 0 \quad (3.16)$$

And the magnetic field vector \mathbf{H} wave equation is given as:

$$\nabla^2 \mathbf{H} - \mu\epsilon \frac{\partial^2 \mathbf{H}}{\partial t^2} + (\nabla \ln \epsilon) \times (\nabla \times \mathbf{H}) + \nabla(\mathbf{H} \cdot \nabla \ln \mu) = 0 \quad (3.17)$$

The gradient of the logarithm of ϵ and μ diminishes inside a homogenous and isotropic medium. Then, the wave equations for electric and magnetic fields are given as:

$$\nabla^2 \mathbf{E} - \mu\epsilon \frac{\partial^2 \mathbf{E}}{\partial t^2} = 0 \quad , \quad \nabla^2 \mathbf{H} - \mu\epsilon \frac{\partial^2 \mathbf{H}}{\partial t^2} = 0 \quad (3.18)$$

These equations are known as Helmholtz wave equations.

The standard EM wave equations is represented by a plane wave equation and is given as:

$$\psi = Ae^{j(\omega t - \mathbf{k} \cdot \mathbf{r})} \quad (3.19)$$

here A , is the amplitude and the magnitude of the wave vector \mathbf{k} is related by:

$$k = \omega\sqrt{\mu\epsilon} \quad (3.20)$$

Since the field is a sinusoidal function of time and it has the same value for coordinates \mathbf{r} and \mathbf{t} . Then it is satisfied by the equation:

$$\omega t - \mathbf{k} \cdot \mathbf{r} = \text{constant} \quad (3.21)$$

The above equation determines a plane normal to the wave vector \mathbf{k} at any instant \mathbf{t} . This plane is called a surface of constant phase travelling in the direction of \mathbf{k} with a velocity whose magnitude is given by:

$$v = \frac{\omega}{k} \quad (3.22)$$

This is called the phase velocity of the wave $\lambda' = \frac{2\pi}{k}$ where λ' indicates the wavelength of light inside the medium. λ_0 is wavelength of light in a vacuum. The value of the phase velocity in a medium can be expressed in terms of the dielectric constant ϵ and the magnetic permeability μ which is given by:

$$v = \frac{1}{\sqrt{\mu\epsilon}} \quad (3.23)$$

And the phase velocity in a vacuum is given by:

$$c = \frac{1}{\sqrt{\mu_0 \epsilon_0}} = 2.997930 \times 10^8 \text{ m/s} \quad (3.24)$$

whereas, the phase velocity in a medium is:

$$v = \frac{c}{n} \quad (3.25)$$

Here, the index of refraction of the medium is denoted as n .

3.2 Brief Comparison of Different Numerical Methods

A waveguide of micron scale dimension waveguide is a complex structure. For designing and fabricating steps, it consists of materials having different composites of index of refraction. For this purpose, the attributes of the light propagation in this kind of waveguide can be investigated by Maxwell's Equations and a numerical method. There are various methods for solving these problems. This includes: Finite Difference Time Domain (FDTD), Finite Difference Method (FDM), and Finite Element Method (FEM). A brief description of commonly used numerical method is presented and discussed in terms of behavior modelling in the next sections.

3.2.1 Finite Difference Method

FDM is the oldest and frequently employed numerical method in the problems that arises in the dielectric waveguide. This method is appropriate for modelling inhomogeneous media and complicated boundary in a rectangular box where the dielectric guide is positioned. This is also called a finite cross-section.

The surrounded cross-section is break and divided into a bunch of rectangular mesh. On the mesh locality, the nodes are situated for its association. An eigenvalue issue is raised at the E-field and H-field interface when continuity and discontinuity conditions are employed. With these, the modal field profiles are solved. However, the exactness of these method relies on the dimension of the mesh. Therefore, computational time may be very long and high memory usage is inevitably required (Wexler, 1969).

3.2.2 Finite Difference Time Domain Method

FDTD method is used to model the finite slabs with arbitrary internal structure and different material combinations. FDTD advantage is to obtain the transmission properties over a wide spectral range with a single calculation. In general, time dependent Maxwell's Equation is solved using FDTD. A set of finite difference equations is also used for solving the various field components at a certain point. Even so, the prime drawback of this method is the high memory requirement and its algorithm complexity (Tsuji & Koshiba, 1996).

3.2.3 Finite Element Method

A solution to range of waveguide guiding problems is solved with FEM method. It is a robust numerical technique for analyzing structures complex issues, for example: optical waveguides that is employed in several other engineering applications. The differential equations in FEM method are altered by variational principle. The optical waveguides cross-section is cleaved into small elements of

triangular shape. A polynomial expression is employed for approximation by suitable field components. With this method, a non-overlapping patchwork of triangular elements is formed by cleaving the region with an issue. In this method, a full vectorial \mathbf{H} -field formulation is considered to be commonly used for designing an optical waveguide as it offers effortless solving boundary conditions present. A 2-dimension, 3-dimension or any random shaped waveguide have the possibility to investigate using FEM method. (Zeinkiew & Taylor, 1977).

FEM method is taken as the most preferable one for light propagation in micron scale waveguide structure over the other numerical methods as discussed in the earlier sections. FEM has the potential for adaptation to complex structure boundaries for its triangular-shaped elements advantage. With this advantage, the structure can be fitted easily and the discretization of elements can be varied in the desired regions where variation of rapid field is present.

In the present work, FEM is chosen for investigating the light propagation in the micron scale designed resin based-waveguide, specifically to determine the presence of fundamental mode field distribution in core section by neglecting the other modes (high order and low order) and also to solve a waveguide problem. Further, the detailed explanation of the FEM's fundamental and its implementation is provided and discussed in the next section.

3.3 Fundamental Of Finite Element Method

FEM, the robust numerical method is widely employed for obtaining an approximate solution of differential equation problems. In other way, a continuous

system approximation by a discretized model is also known as FEM method. Therefore, algebraic issue is formed by implementing a different approach in FEM. Here, the finite elements having complex equations are being resolved for obtaining uncomplicated shape (Zeinkiew & Taylor, 1977). The fundamental of FEM is the patchwork approximation by representing any random cross-section areas which can be divided into triangular or quadrilateral shapes, called elements. Different materials are formed from each element, for example, non-linear, lossless, anisotropic, is described by arbitrary permittivity and permeability tensors, $\hat{\epsilon}(x, y)$ and $\hat{\mu}(x, y)$ respectively. Towards the longitudinal z-axis, it is presumed that the waveguide has a consistent shape. Its time and axial dependencies are given by $e^{j\omega t}$ and $e^{-\gamma z}$ where, ω is the angular frequency and γ is the complex propagation constant. A cross-section of arbitrary shapes composing of different materials in x-y plane is shown in figure 3.2.

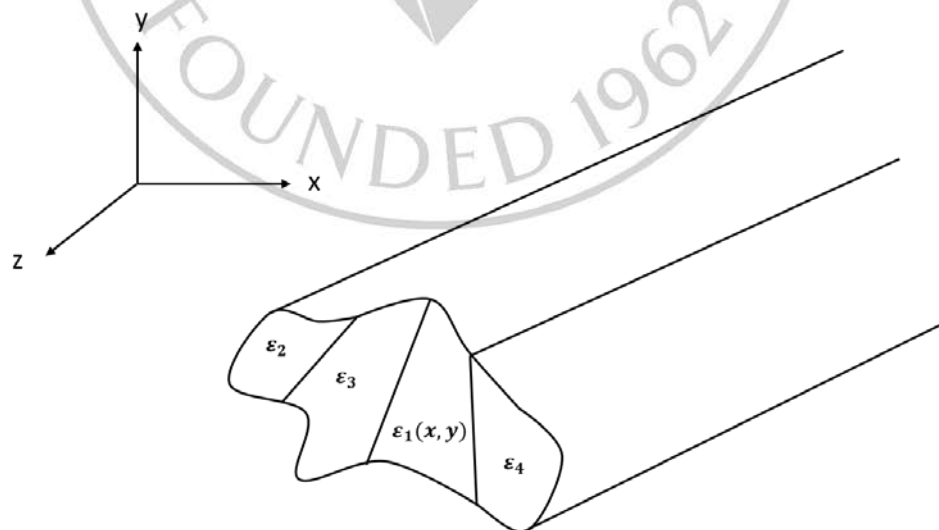


Figure 3.2: Random shape of optical waveguide having contrasting materials

Considering that the wave propagates along the waveguide whose index of refraction is constant, angular frequency is ω and propagation constant, β . Then, \mathbf{E} and \mathbf{H} of the waveguide is written:

$$\mathbf{E}(x, y, z, t) = \mathbf{E}(x, y)e^{j(\omega t - \beta z)} \quad (3.26)$$

$$\mathbf{H}(x, y, z, t) = \mathbf{H}(x, y)e^{j(\omega t - \beta z)} \quad (3.27)$$

where $\mathbf{E}(x, y)$ and $\mathbf{H}(x, y)$ are spatial time-domain-independent \mathbf{E} and \mathbf{H} fields. So as to the confinement of the two-dimensional optical waveguide, the propagations are not perfectly TE and TM modes.

3.3.1 Variational Formulations

As discussed in section 3.1, FEM applications in the investigation of an optical waveguide issues, fundamental Maxwell's equations, boundary conditions and wave equations are examined.

In this section, for the formulation of FEM for optical waveguides, the variational or Raleigh-Ritz approach is also examined for investigating the optical waveguide issues. Here, the \mathbf{E} and \mathbf{M} field are expressed as scalar, i.e., one field component (Mabaya et al., 1981). On the other hand, the \mathbf{E} and \mathbf{M} field are also expressed as vector, i.e., two field components.

FEM formulations mostly implemented give rise to a standard eigenvalue issue (Rahman & Davies, 1984a) and it is given by:

$$[\mathbf{A}]\{x\} - \lambda[\mathbf{B}]\{x\} = 0 \quad (3.28)$$

Here, A and B are real symmetric scant matrices, and positive definite is given by B. Depending on the formulation, the eigenvalue λ , could be chose to β^2 or k^2 . These eigenvalues portray the nodal field values of the finite-elements.

3.3.2 The Scalar Approximations

This approximation is applied where the field are described as TE or TM mode and it is expressed in terms of the longitudinal components. It is used for the figuring of homogeneous waveguide issues and for the investigation of anisotropic waveguides (Koshiha, 1992).

For the quasi-TE modes over a region Ω , E_x is the dominant field component and its formulation is written as (Mabaya et al., 1981):

$$L = \iint_{\Omega} \left[\left(\frac{\partial E_x}{\partial x} \right)^2 + \left(\frac{\partial E_x}{\partial y} \right)^2 - k_0 n^2 E_x^2 + \beta^2 E_x^2 \right] d\Omega \quad (3.29)$$

Here, β is the propagation constant and n is the index of refraction.

For the quasi-TM modes over a region Ω , H_x is the dominant field component and its formulation is written as (Mabaya et al., 1981):

$$L = \iint_{\Omega} \left[\frac{1}{n^2} \left(\frac{\partial H_x}{\partial x} \right)^2 + \frac{1}{n^2} \left(\frac{\partial H_x}{\partial y} \right)^2 - k_0 H_x^2 + \frac{1}{n^2} \beta^2 H_x^2 \right] d\Omega \quad (3.30)$$

3.3.3 Vector Formulations

The formulation of scalar is insufficient for handling inhomogeneous

issues. A more accurate representation of general waveguide fields is much needed with two components and this is the reason where the formulation of vector comes in the picture. Many authors have proposed a number of vector formulations dealing with optical waveguide issues. Yet, few of it are affected by non-physical spurious solutions. Therefore, many types of methods are proposed for overcoming these issues.

The first formulation in the FEM investigation is E_z and H_z (Mabaya et al., 1981). This formulation fails to handle general anisotropic issues without dismantling the eigenvalue equation (3.28) canonical form. In addition, it also fails to evaluate the issues of arbitrary dielectric distribution rising in a waveguide. With this point of view, the axial field components \mathbf{E} and \mathbf{H} fields are of minimal important.

The \mathbf{E} field vector formulation (Koshiba et al., 1985) can handle general anisotropy. This is also implemented for resolving solution of optical waveguides of different versions. Here, the boundary conditions fit to magnetic wall and imposes ($\mathbf{n} \times \mathbf{E} = 0$) as its boundary condition.

The \mathbf{H} field vector formulation is appropriate for issues in dielectric waveguide as the magnetic field is continuous. Hence, boundary conditions forces are not required.

The desired formulation is now written as (Rahman & Davies, 1984a):

$$\omega^2 = \frac{\int (\nabla \times H)^* \cdot \hat{\epsilon}^{-1} \cdot (\nabla \times H) d\Omega}{\int H^* \cdot \hat{\mu} \cdot H d\Omega} \quad (3.31)$$

Here, the natural frequency is ω , cross-section of the waveguide is Ω and

permittivity and permeability are given by $\hat{\epsilon}$ and $\hat{\mu}$.

Yet, the formulation discussed above, give rise to a spurious solution, as divergence condition, $\nabla \cdot \mathbf{H} = 0$ doesn't satisfy. Hence, the penalty coefficient method (Koshiba et al., 1985) is proposed for eliminating these types of solutions.

The formulation of variation of transverse \mathbf{E} or \mathbf{H} field components is proposed for the solution of issues in the optical waveguide (Hayata et al., 1986). Here, the two field components are employed. By doing this, $\nabla \cdot \mathbf{H} = 0$ divergence condition is being approved and the lossy structures are handled precisely. By looking at the other side, it leads to complex limited and non-symmetric matrices that increases its computational time. Hence, an effort is implemented to develop an efficient sparse matrix (Fernandez et al., 1991) to solve these kinds of problems.

3.4 Outline Of Finite Element Formulation

As mentioned earlier, FEM is a numerical technique for obtaining approximate solutions of boundary value issues and finding the answer of complex structures. In FEM, differential equation based on Raleigh-Ritz variational method and Galerkin method of weighted residuals are implemented. Here, a cross section of arbitrarily shaped waveguide is divided into a patchwork of elements (figure 3.3). The cross-sectional area of the waveguide is given by Ω and the boundary is Γ . The boundary has an electric wall Γ_e and magnetic wall Γ_m with tangential \mathbf{E} and \mathbf{H} fields as zero. Assuming the core and cladding of the waveguide, the wave equation for \mathbf{H} -field is displayed that is based on Maxwell's equations (Koshiba, 1992):

$$\nabla \times ([\epsilon_r]^{-1} \nabla \times \mathbf{H}) - k_0^2 \mathbf{H} \quad (3.32)$$

where ϵ_r , is the relative permittivity of the medium.

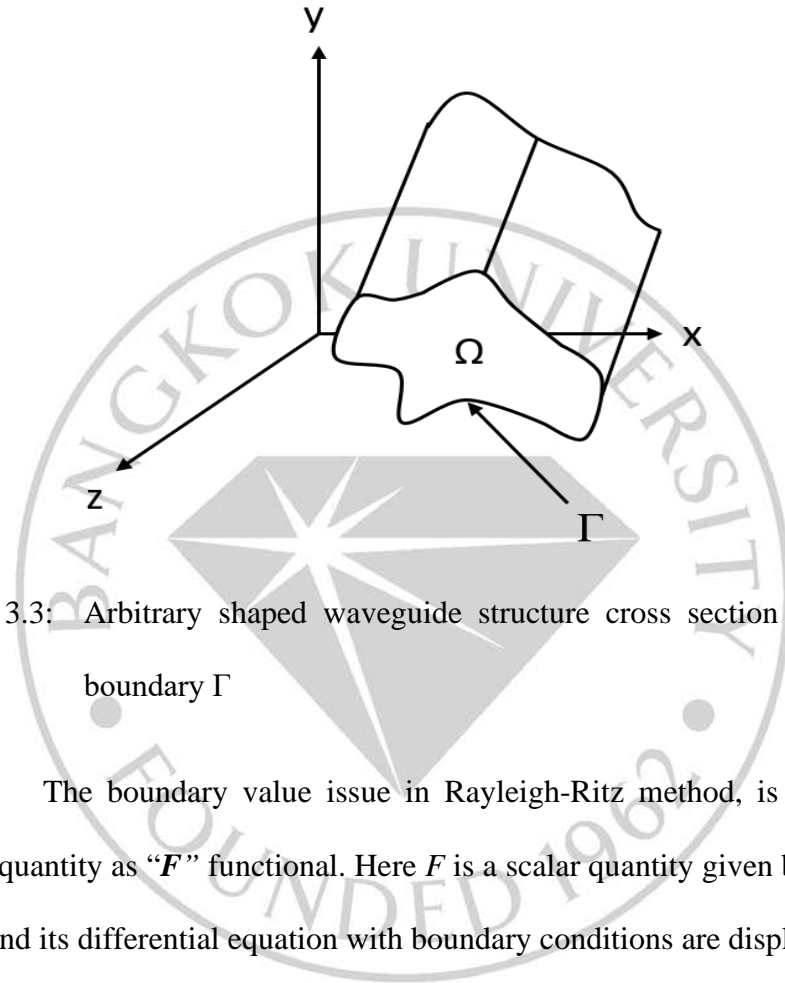


Figure 3.3: Arbitrary shaped waveguide structure cross section area Ω and boundary Γ

The boundary value issue in Rayleigh-Ritz method, is expressed in scalar quantity as “ F ” functional. Here F is a scalar quantity given by an integral form and its differential equation with boundary conditions are displayed as:

$$F = \iint_{\Omega} (\nabla \times \mathbf{H})^* ([\epsilon_r]^{-1} \nabla \times \mathbf{H}) d\Omega - k_0^2 \iint_{\Omega} \mathbf{H}^* \cdot \mathbf{H} d\Omega \quad (3.33)$$

In the equation 3.33, the wave equation is the \mathbf{H} field obtained from the unknown function that describes the F as constant stationary with a minimal change given by δH . This type of changes is exhibited and expressed by Euler’s equation (Koshiba, 1992):

$$\partial F = 0 \quad (3.34)$$

Now by employing Gauss' divergence theorem from the first variation ∂F , Euler's equation is written as (Koshiba, 1992):

$$\delta F = \iint_{\Omega} \delta \mathbf{H}^* \cdot \left[\nabla \times \left([\epsilon_r]^{-1} \nabla \times \mathbf{H} \right) - k_0^2 \mathbf{H} \right] d\Omega - \int_{\Gamma} \delta H^* \cdot \left[\mathbf{n} \times \left([\epsilon_r]^{-1} \nabla \times \mathbf{H} \right) \right] \delta \Gamma \quad (3.35)$$

Here, unit normal vector is given by \mathbf{n} with boundary as Γ . Then the expression $\mathbf{n} \times ([\epsilon_r]^{-1} \nabla \times \mathbf{H})$ depicts the tangential \mathbf{E} field.

It is observed from the equation 3.35, that by employing variational principle in equation 3.33, the equation 3.34 equates with equation 3.32.

The condition of the boundary $\mathbf{n} \times ([\epsilon_r]^{-1} \nabla \times \mathbf{H}) = 0$ is proved along Γ_e boundary. Hence, it is taken as the natural boundary condition. The equation 3.35 fail to satisfy the condition of boundary on the \mathbf{H} boundary wall given as Γ_m . Hence, a condition of forced boundary of $\mathbf{n} \times \mathbf{H} = 0$ is obtruded.

The cross section Ω is sub-divided to a different type of elements.

Then, the \mathbf{H} is given by:

$$H = \sum_{i=1}^m N_i H_i \quad (3.36)$$

where, m is the number of nodes, H_i is the nodal \mathbf{H} field for each node of the elements, and N_i is a set of known basis functions (Davies, 1989).

The equation 3.36 is expressed in matrix notation and is given by:

$$H = [N]^T \{H\}_e \quad (3.37)$$

where, T denotes transpose and $[N]^T$ and $\{H\}_e$ is the matrix basis functions and the element column vector of the nodal field values.

Substituting the value of \mathbf{H} in the equation 3.33, the waveguide issues are resolved and the obtained equation is given as:

$$\iint_{\Omega} \left(\nabla \times [N]^T \{H\}_e^* [\varepsilon_r]^{-1} \nabla \times [N]^T \{H\}_e - k_0^2 [N]^T \{H\}_e^* [N]^T \{H\}_e \right) d\Omega = 0 \quad (3.38)$$

By arranging the above equation 3.38 and transforming it into a matrix form, the issues is resolved to a standard eigenvalue problem as (Rahman & Davies, 1984a; Koshiba, 1992):

$$[A]\{H\} - k_0^2 [B]\{H\} = 0 \quad (3.39)$$

Here, k_0^2 is the eigenvalue and $\{H\}$ is the eigenvector. A complex Hermitian is given by A matrix and symmetric real is given by B matrix.

As discussed in the above sections, the optical waveguide issues are resolved by employing FEM numerical investigation which is expressed as standard eigenvalue equation (equation 3.39). A and B are matrix of an element, for each triangular element of the optical waveguide. These matrices are assembled to form a global matrix where the eigenvalue issue is resolved.

By employing FEM investigation, it is also possible to acquire the type of modes available in the optical waveguide structure of complex index of

refraction. In the Appendix A, the A and B element matrix establishment and its global matrix are given with broad discussion.



CHAPTER 4

DESIGN AND FABRICATION OF THE WAVEGUIDE

The following chapter gives a discussion about the design, concept and the fabrication of the proposed integrated single-step elevated or tower-shaped optical waveguide using 3D printer DLP technology. The chapter starts with providing the concept of the structure then the flow chart for its design using the FEM technique to obtain the field distribution for fundamental mode in the structure is presented. After the desired structure modelling is performed, the fabrication of the structure is made using 3D DLP printer (Wanhao Duplicator D7 Box) with its desired parameters and matched with the numerical analysis. To conclude this chapter, this structure is used for sensing application as a vapor sensor and its performances are detailed.

4.1 Concept Of The Waveguide Structure

In this work, the concept of the structure is to design and develop a single step elevated or tower-shaped integrated polymer-based optical waveguide by making use of DLP technology-based 3D printer. Here, the substrate and the core part are of the similar substance i.e., polymer resin (Hexpolymer PX 8880). Having this design, high confinement of light is established in the ridge or core part when the light source is illuminated at the waveguide facet. Normally, for high confinement of light, the waveguide core part should possess a peak index of refraction comparing to the substrate part and its surroundings. This is acquired from the different methods such as lithography/imprinting and thin film deposition.

Yet, when the overall core part of the waveguide is fabricated from the similar substance with the same index of refraction, the generated modes are normally confined in the substrate area. This is not accepted in applications a definitive sensor.

In this work, the waveguide is designed by lifting the core region in upward direction making it to stand like a tower. This design reduces the index of refraction in the substrate area which includes the tower and surrounding cladding area. As a result, stronger confinement of light in the ridge area is acquired, thus making it more suitable for application a sensor. This detailed discussion is explained in the section 4.3. Figure 4.1 shows the concept of the designed structure showing the confinement of light for with and without tower shape structure using resin as a substance.

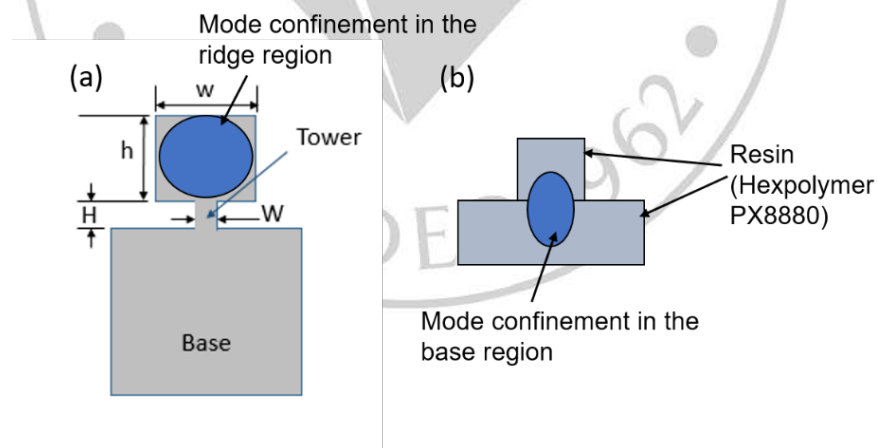


Figure 4.1: (a) Ridge area mode confinement in the tower-shaped waveguide structure (b) Base area mode confinement in the waveguide structure without tower

4.2 Flow Chart for Modelling The Waveguide Structure

In the figure 4.2, the programming steps in the MATLAB for modelling the waveguide structure is displayed. Firstly, the data is being loaded from the excel file and is proceeded for the meshing analysis where the material of the waveguide (ridge and the substrate region) are being assigned.

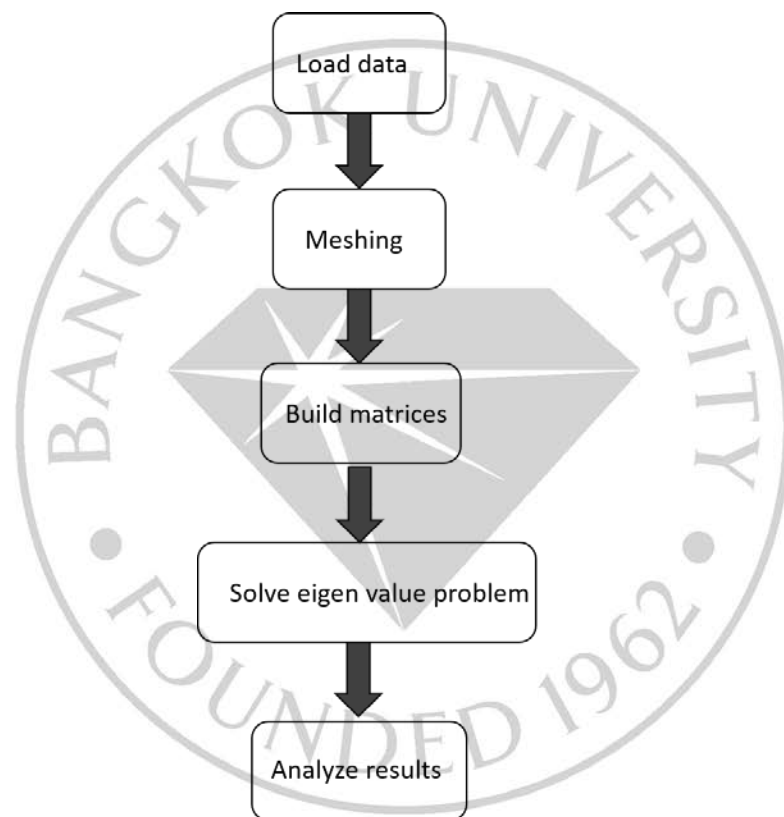


Figure 4.2: Flow chart of the FEM technique using MATLAB program to calculate the field distribution for fundamental mode in the tower-shaped waveguide structure

The next step is for building the matrices which is the core of the FEM technique to solve the eigen value problem that arises using the built-in function in

MATLAB. After the number of iterations are performed, the results are analyzed and plotted. The FEM simulation is performed in this work for the tower-shaped waveguide structure to check the field distribution for the fundamental mode prior to fabrication. The utilization of the FEM is lengthy and the detailed explanation is provided in Appendix A.

The FEM simulation was first performed with the traditional structure of the ridge waveguide by keeping the substrate and the guided region of the same material. The designed parameters for the tower-shaped waveguide structure are: $600\mu\text{m}$ for ridge height (h) and ridge width (w) and $200\mu\text{m}$ for the tower height (H) and tower width (W) and for the traditional waveguide ridge region parameters are kept the same as the ridge region of the tower-shaped waveguide. Figure 4.3 shows the simulation result of the traditional ridge waveguide structure when the substrate and the guided region are of same material (Hexpolymer PX8880).

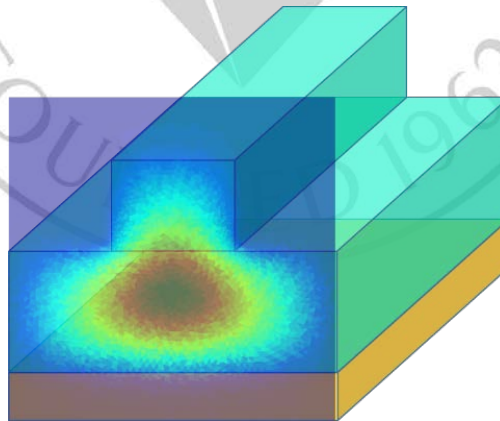


Figure 4.3: Traditional ridge waveguide structure field distribution for fundamental mode

From the figure 4.3, it shows that when the structure is designed with the similar

substance, the guided mode is mostly located in the substrate area. This is not accepted for an application a sensor, due to the low confinement in the core area. Therefore, the sensitivity is less in this ridge structure. In addition, for acquiring peak confinement in the core area for this traditional ridge structure, the fabrication involves two different layers and it will be challenging in order to make sensor affordable. To simplify the design, the tower-shaped waveguide structure was introduced as a one-piece structure that is fabricated using the same material (Hexpolymer PX8880) and the simulation result for the field distribution for fundamental mode is shown in the figure 4.4.

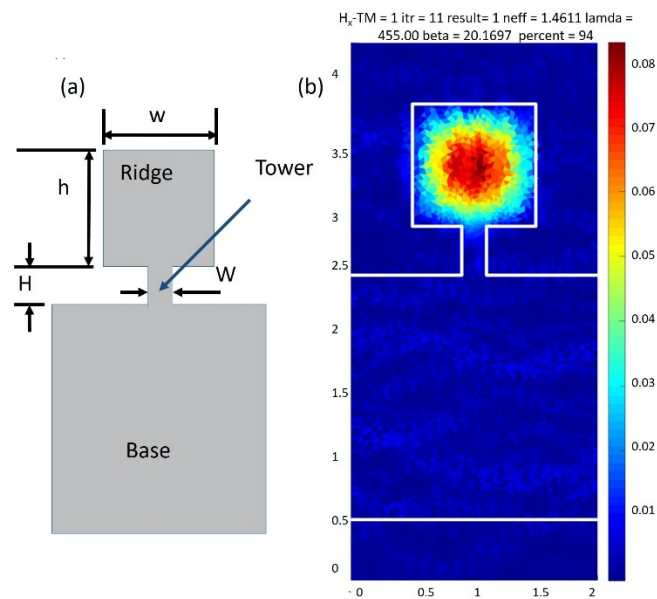


Figure 4.4: (a) Design parameters of the tower-shaped waveguide (b) Confinement of mode in the ridge area

It is noticed from the figure 4.4 that from the formation of lower index of refraction around the tower area and surrounding cladding area, peak confinement is acquired in the ridge area of the structure. This is made possible even if the structure is built with similar substance. The field distribution of the fundamental mode is confined in the ridge area by applying a FEM numerical technique. Having this, it makes easier for coupling of light and acquiring of data. With various iterations, it is noticed that the designed structure is sensitive to the variation in the surroundings. Thus, it can be utilized to work as an application in sensing system. With these simulation results, the fabrication of the tower-shaped waveguide is proceeded.

4.3 Fabrication Of The Tower-Shaped Waveguide Structure

The parameters were first defined and the tower region of the structure is extended from 80 μm to 200 μm by keeping the width (W) of the ridge area constant at 600 μm for different specimens. The reason for extending the dimensions of the structure is to investigate the minimum dimension of the tower region that can be achieved using DLP technology-based 3D printer. Table 4.1 shows the designed structure dimensions that is applied in this work.

Table 4.1: Different dimensions for the designed tower-shape waveguide

Specimen	Width of the ridge in μm	Height of the ridge in μm	Width of the tower in μm	Height of the tower in μm
Specimen 1	600	600	80	80
Specimen 2	600	600	100	100
Specimen 3	600	600	150	150
Specimen 4	600	600	200	200

In the figure 4.5, the steps of the fabrication of the designed structure are given depicting in a block diagram.

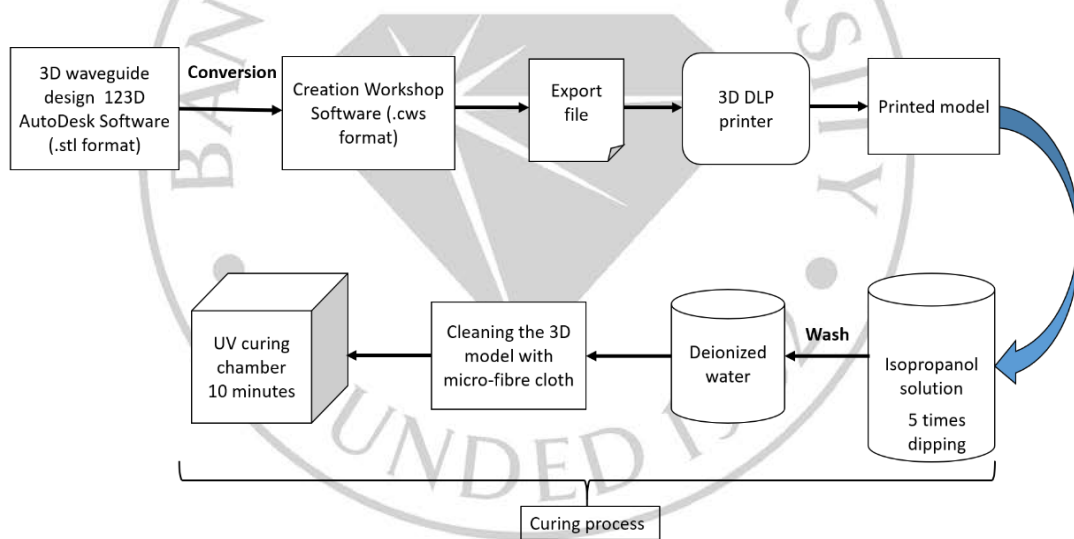


Figure 4.5: Fabrication steps of the tower-shaped waveguide structure

The different designs parameters for the waveguide structures are constructed using a CAD software (123D AutoDesk) that creates stl files. The next step is conversion of these stl file to a CreationWorkshop (.cws) file format. This is done as DLP based

3D printer accepts these formats. Figure 4.6 (a and b) shows the creation workshop platform specifically for the DLP printing to design and convert it to the supported file format (.cws) and figure 4.6 (c) shows the DLP based 3D printer used in this work.

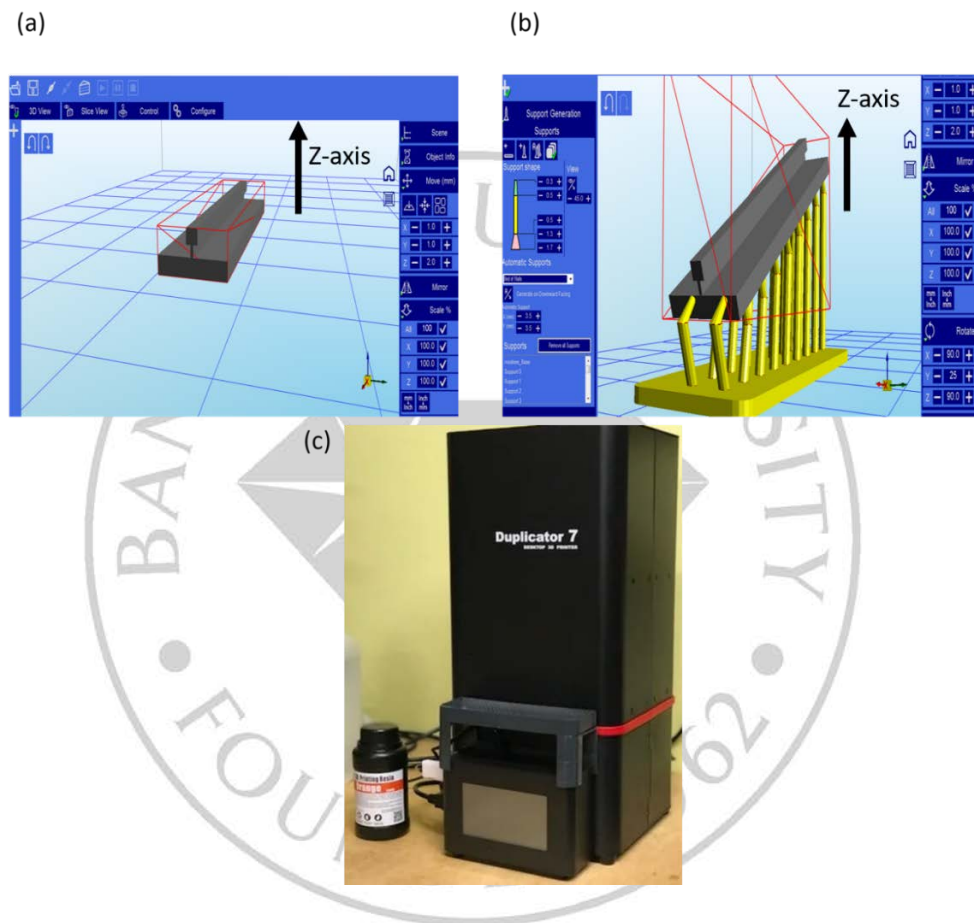


Figure 4.6: (a) Creation Workshop platform (b) 3D designed elevated waveguide with the support generation and rotated at 25 degrees by lifting towards Z-axis (c) DLP based 3D printer Wanhao Duplicator D7 Box

At first, the structure is placed in the area where it will be built by rotating it to 25 degrees and lifting in Z-axis direction. In the build area, the supports are given in the

structure so that it clasps tightly in the course of printing. In addition, it also assists in assembling correct 3D image pixilation in the 3D printer's LCD area. The illustrative diagram of 3D printer employed is given in figure 4.7.

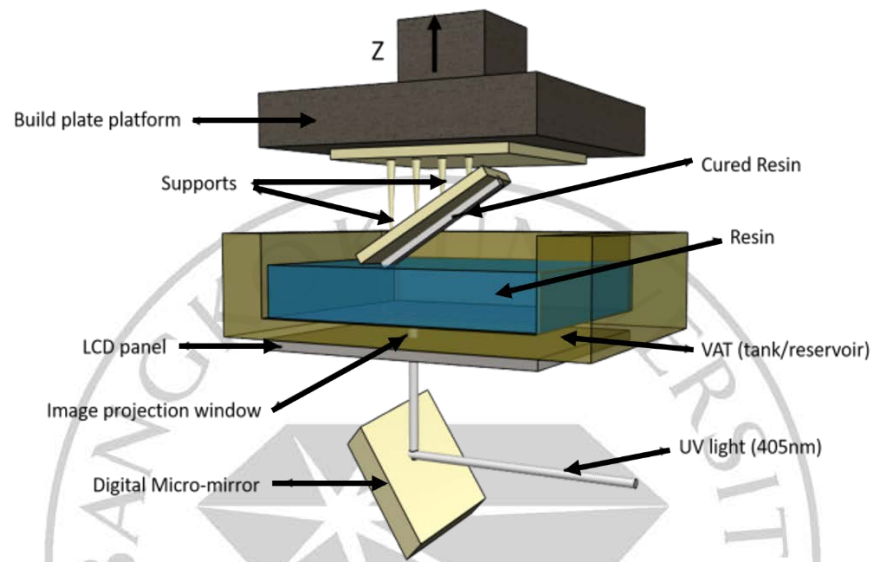


Figure 4.7: Illustrated diagram of the DLP based 3D printer

A DLP based 3D printer Wanhao Duplicator D7 box is employed where it uses liquid clear resin PX-8880 Hexpolymer and it is very sensitive to ambient light. When the 3D printer is switched on, at first the z-axis stage or the build plate of the printer is operated to move downwards into the pool of resin by maintaining a gap of 1mm at the bottom level for calibrating the machine. The plate at the base level is clear. When the UV light is made to fall into this plate through Digital Micro-mirror (DMD), the image or layer projected from DMD to LCD panel thicken. Later, the z-axis stage advances in upward direction for 50 μ m steps. This operation is continued till the final product is successfully printed. The print

quality of the first layer of the product relies on the time amount of UV light exposure from the printer. After the operation of printing is accomplished, the final printed product is separated from the build plate platform and postprocessing procedures are employed.

At first, in the isopropanol alcohol (IPA), the printed product is immersed for 5 times for washing the unwanted or uncured resin that is attached. After that the product is rinsed with deionized (DI) water. Employing this step cleanses the quality of the surface of the product and the fine details of the print quality is divulged. In the next step, the product wiped with the microfiber cloth and it is left for drying. In the end, the product is stowed in UV light chamber for final curing procedure to eliminate toxicity of the resin and perfect polymerization of the product. As in fact that the product is in micron size, the time limit for placing in the UV light chamber is 10 minutes. Exceeding this time limit may distort or break the product.

The surface of the product is polished with sand paper with 200, 400, 600, 800, 1000, 1200, and 2000 grits after the fabrication of the product i.e., the tower-shaped waveguide is concluded. It is done to eliminate the roughness that is generated by the printing angle and for minimal scattering. After finishing the postprocessing, the products are taken for characterization and matched up with simulation results.

4.4 Optical Characterization Of The Fabricated Structures

The tower waveguide structures ranging from (80 μ m to 200 μ m) are

printed for determining the highest peak confinement in the core area. In addition, the optical characterization is performed to achieve the minimum tower-shape structure from the DLP based 3D printing method and match with the simulation results. The design parameters are presented in Table 4.1. The illustrative characterization set-up for the different samples is shown in the figure 4.8. A LED driver is used to set the maximum intensity of a warm white LED to illuminate in facet of the waveguide ridge area.

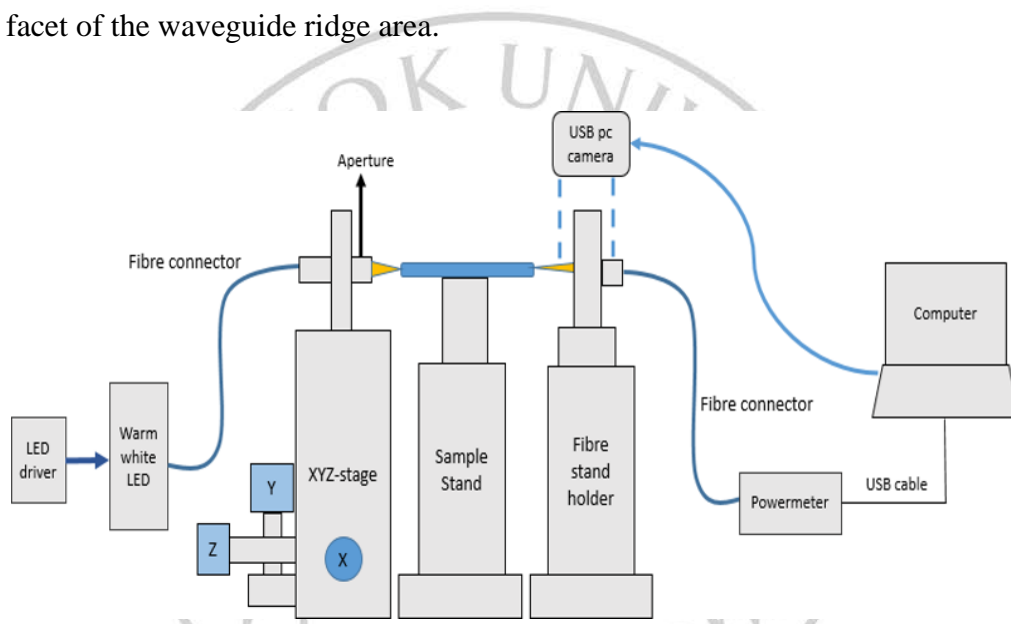


Figure 4.8: Illustrative optical set-up for investigation of confinement of light and transmitted power calculation

The XYZ translation stage is employed for strong alignment of the waveguide and the light that is illuminated. A small aperture is made where the illuminated light narrows down like a spot from the LED through optical fiber and let it fall at the facet of the waveguide ridge portion. Towards the receiver side, another optical fiber is allocated closely to the waveguide for evaluating peak intensity of light.

Finally, this optical fiber is attached to the powermeter and then to a computer through USB cable for further investigation.

For capturing the tower-shape waveguide images of its confinement of light in the ridge area, a USB based camera is operated. Before the investigation of the powermeter, the images were first are captured with the USB based camera and is displayed in the figure 4.9.

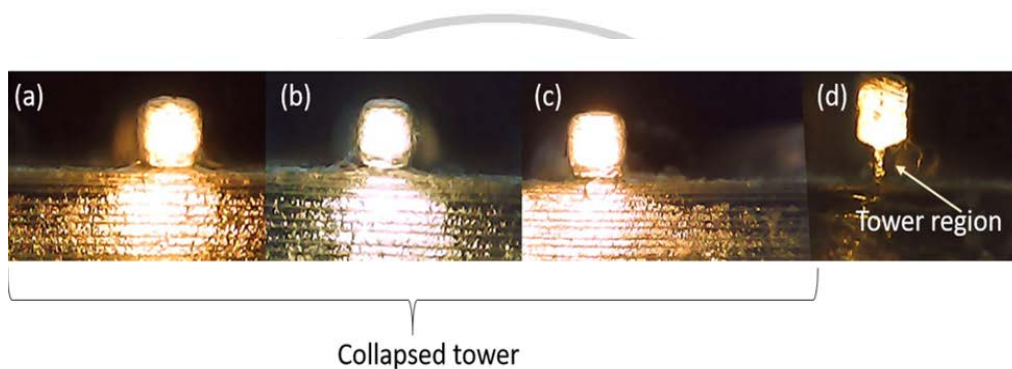


Figure 4.9: Captured images of the varying dimensions of the tower region confinement of light with 600 μm ridge area (a) 80 μm , (b) 100 μm , (c) 150 μm , and (d) 200 μm

As displayed in above figure 4.9 (a, b and c), the tower region dimensions from (80, 100, and 150) μm with 600 μm ridge area didn't print successfully. The reason behind it is from the poor mechanical stability of clasping the ridge area in the course of printing procedure, angle projection of the image from the DMD at this area and printer's resolution (50 μm). The leakage of light at the base area of the waveguide is at peak level in these tower region dimensions and for this reason the following dimensions are not studied. The prime idea for the development of

waveguide is to acquire the least height and width of the tower area so that it clasps stronger to the bigger ridge area. The least height and width of the tower area was chosen to support the less effective index in the tower region thereby increasing the confinement of light in the ridge area. Therefore, the larger width and height of the tower dimensions were not investigated. The confinement of light is at peak with 200 μm tower region and 600 μm ridge area than the rest. This feature dimensions were further investigated and it is discussed in the next sections.

4.4.1 Surface roughness quantification of the fabricated structure

The quantification of the roughness of the surface for fabricated structures are carried out by investigating the images that were captured for accuracy estimation. As described earlier, the roughness generation shows up from printers' resolution and slicing process during printing. The DLP based 3D printer has an LCD screen projector at the base. Obtruding the images of the structure to the base layer emerges as a pixel (bricks of small rectangular box) also called voxels. This causes scattering of light and can be implemented as an application as sensor that is described in the section 4.5.

The side view of the waveguide tower is shown in the figure 4.10(a). The slanted lines in the structure exhibit roughness of the surface and these lines are formed periodically from layer-by-layer trend of the printer. For determining the reoccurrence of the formed lines in the structure, the given equation computes the dimension of lines from the images obtained.

$$\Delta_x = \frac{\Delta}{\sin \theta}, \quad \Delta_y = \frac{\Delta}{\cos \theta} \quad (4.1)$$

where the printers' resolution is given by $\Delta = 50\mu\text{m}$ and the degree of rotation of structure angle printing is given by $\theta = 25$ degree.

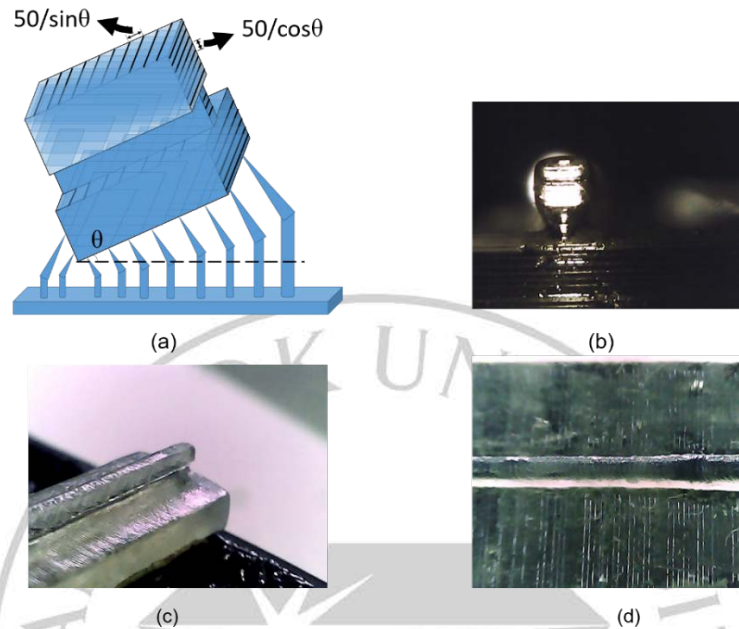


Figure 4.10: (a) Illustrative view of the waveguide tower structure with supports at the base with 25-degree print angle for appropriate pixelation and $50\mu\text{m}$ roughness of the surface. (b) Front view of the waveguide tower structure displaying its roughness of the surface. (c) Waveguide tower structure oblique view. (d) Top view of the waveguide tower structure floor region.

The $200\mu\text{m}$ tower area dimension accomplished from optimized selected criterion is displayed in the figure 4.10(b). The isometric and the top view of the waveguide tower structure is displayed in the figures 4.10(c) and (d) displaying its roughness of the surface. The given table 4.2 is displays the measuring and evaluated values for investigation roughness of the surface in waveguide tower structure.

Table 4.2: Differentiation between practical and theoretical value line size in the waveguide tower area and the floor area

Interpretations	Top view (micron)	Front view (micron)
Size of the lines calculated from the pixel of an image (practical value)	96.85	55.85
Calculated value of the size of the lines (theoretical value)	118.14	55.16
Standard deviation	9.03	5.79

The texture image investigation for the tower waveguide structure is carried out by gray-Level co-occurrence matrix (GLCM) (Haralick et al., 1973) for scattering of light from the roughness of the surface. This investigation contains GLCM contrast and the correlation evaluation of roughness of the surface in the floor and tower area of the structure.

The DCC1545M-CL monochrome CMOS microscopic camera (Thorlabs, Inc., USA) is used for the image accretion. The following figure 4.11 displays tower waveguide structure images employed for the investigation of the texture and line size evaluation.

The benefit of employing GLCM specifies the structure roughness of the surface with the metrics given: distance, intensity of the pixels and the orientation. The constancy of appearance of the gray level picture at certain

orientation and the distance is expressed by GLCM matrix. Four metrics of co-occurrence matrix have been used to estimate the surface roughness. These metrics were tested with multiple combinations. For 1-pixel step, it is tested for 0-degree, 45-degree, 90-degree and 135-degree, for 2-pixel step, 0-degree, 45-degree, 90-degree and 135-degree, for 5-pixel step, 0-degree, 45-degree, 90-degree and 135-degree and for 35-pixel step, only 90-degree angle is tested. The evaluated values are shown in Appendix E. Only contrast and correlation show quantifiable measurements for the surface with different roughness. Hence these two metrics with a pixel step of 35 and an angle of 90 degree were considered as valuable metrics to estimate the roughness of the surface.

From the figure 4.11 (c), the vertical patterns are in repetitive manner for the tower waveguide structures. Therefore, the parameters employed for GLCM are distance of 35-pixel step with 90-degree orientation.

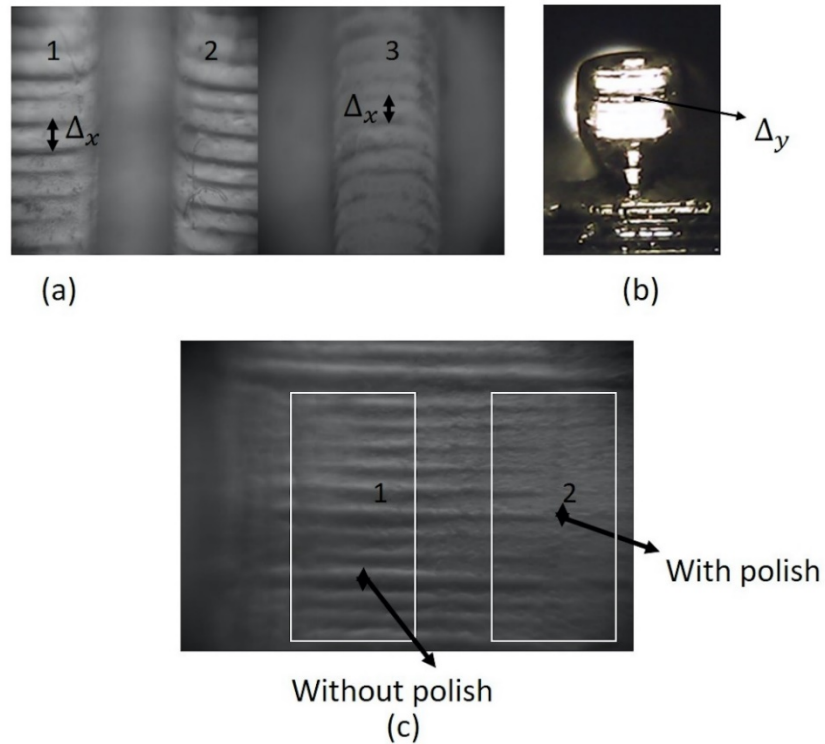


Figure 4.11: (a) Top view of the structure lines in the tower area (a-3) and in floor area (left area: a-1, right area: a-2) (b) Front view of the structure slicing lines. (c) Top view of the floor area of the structure (c-1) polished area and (c-2) non-polished area

The polished and non-polished area images of the structure is displayed in the figure 4.11 (c). With this figure, the second-order statistical texture metrics are evaluated and is given as:

$$Constrast = \sum_{i,j} |i - j|^2 p(i,j) \quad (4.2)$$

$$Correlation = \sum_{i,j} \frac{(i - \mu_i)(j - \mu_j) p(i,j)}{(\sigma_i, \sigma_j)} \quad (4.3)$$

where $p(i,j)$ is the normalized GLCM value in the location i,j . The evaluated GLCM value at the location i, j . μ_i and μ_j is given by $p(i,j) = \frac{P(i,j)}{\sum_{i,j} P(i,j) \cdot P(i,j)}$. The row means and sums of the column are given by μ_i and μ_j . Finally, the standard deviations are σ_i are σ_j .

The evaluated contrast elucidates the difference of local gray-level quantity in an image. Here, the wrinkle kind of texture is displayed by a high value. The low frequency value is given by a contrast of low value. The dependency of the gray level with linear trend describes the correlation matrix.

The texture evaluation of the fabricated waveguide images has been executed on three waveguides. The two polished structures are displayed in the figure 4.11 (a-1) and (a-2) and the non-polished structure is displayed in the figure 4.11 (a-3). The last one is the two structures displayed in the figure 4.11 (c-1); polished area and (c-2); non-polished area. The achieved results from the above evaluation are given on table 4.3. This gives the distinction between them. The results are: contrast of the polished area is higher by 5 times displayed in the figure 4.11 (a-1) than unpolished area displayed in the figure 4.11 (a-3). Similarly, polished area is 2.6 times higher than unpolished area as displayed in the figure 4.11 (c-1) and figure 4.11 (c-2).

Table 4.3: Evaluation of GLCM metrics of polished and un-polished structures

Figure references	4.11 (a-1)	4.11 (a-2)	4.11 (a-3)	4.11 (c-1)	4.11 (c-2)
GLCM parameters: 35 Pixel step, 90 degree					
Contrast	0.958	1.295	0.182	0.775	0.291
Correlation	0.072	-0.184	0.632	-0.040	0.052

The above two figures 4.11 (a-3) and (c-2) have low values of contrast and have an even surface. Similarly, for the given figures 4.11 (a-1), (a-2) and (c-1), the values of contrast are higher and display a wrinkle texture. The given other correlation metrics also display a matching behavior. With these achieved results, the GLCM matrices exhibit the potential for quantifying the waveguide surface evenness. The next section discusses the investigation of loss of power.

4.4.2 Power Attenuation Analysis

The fabricated structures were carried out for power attenuation evaluation in vertical direction. The four types of structures having a range of tower dimension: 80 μm to 200 μm were investigated. The investigation of the different structures is proceeded by evaluating the transmission of light at different spot by the powermeter positioned at the base area (output) as displayed in the figure 4.12. The attenuation is determined by the given equation:

$$I_{out} = I_{in} [e^{-2\alpha L} \cdot \eta] \quad (4.3)$$

where I_{out} is the light transmitted intensity, I_{in} is the light incident intensity, attenuation coefficient is α , thickness or length of the structure is L , and the efficiency of coupling is η .

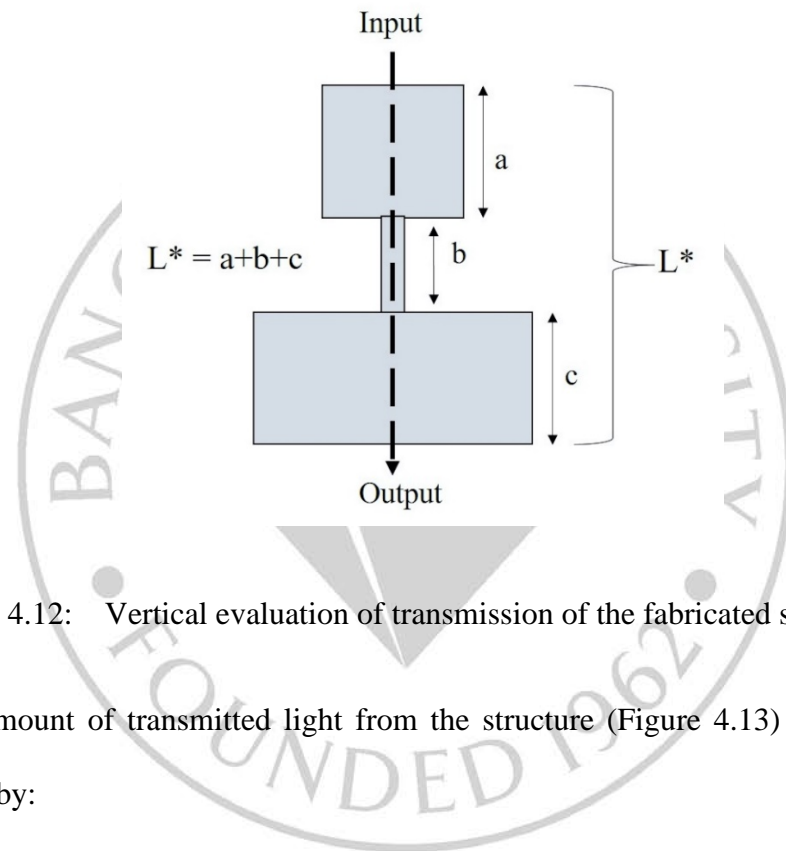


Figure 4.12: Vertical evaluation of transmission of the fabricated structures

The amount of transmitted light from the structure (Figure 4.13) evaluation is given by:

$$T = \{1 - (1 - R) R\} e^{-2\alpha L^*} \quad (4.4)$$

Where the transmittance and reflectance are given by T and R , L^* is the length of the structure. Reflectance is given by $R = \left(\frac{n-1}{n+1}\right)^2$. Here, n is the structures index of refraction ($n=1.4759$).

The fabricated structures power attenuation coefficient is given by:

$$\frac{I_{out}}{I_{in}} = T. e^{-2\alpha L} \quad (4.5)$$

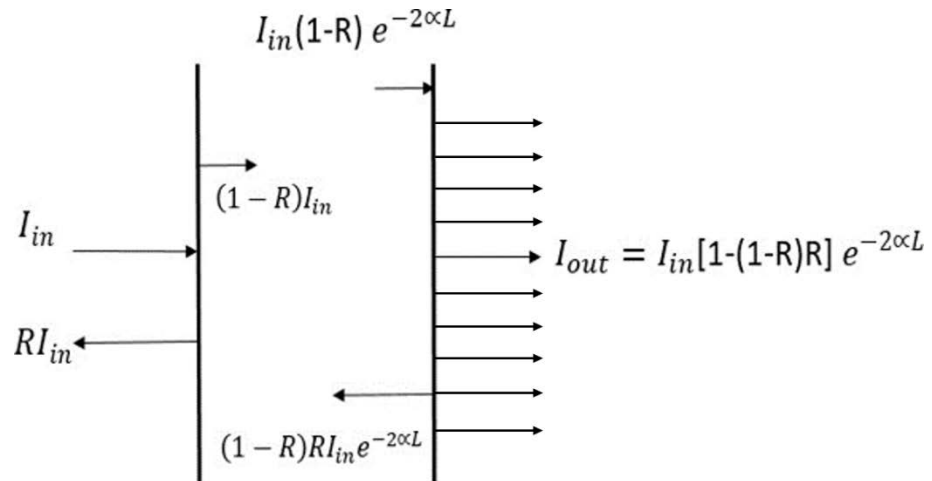


Figure 4.13: Approximation evaluation of the structure's attenuation coefficient by the incident light at vertical position and its different acquired positions

The input light illuminated vertically is fixed at $3.43\mu w$ for different fabricated waveguide structures. The transmitted intensity of light at the output side were acquired at the different positions for evaluating the attenuation coefficient. The illustrative is displayed in the figure 4.13.

The acquired results from the evaluation of the different structures are plotted in the figure 4.14, displaying the attenuation from the several positions. A histogram shape is formed that is Gaussian in nature having an attenuation coefficient of $1 cm^2$.

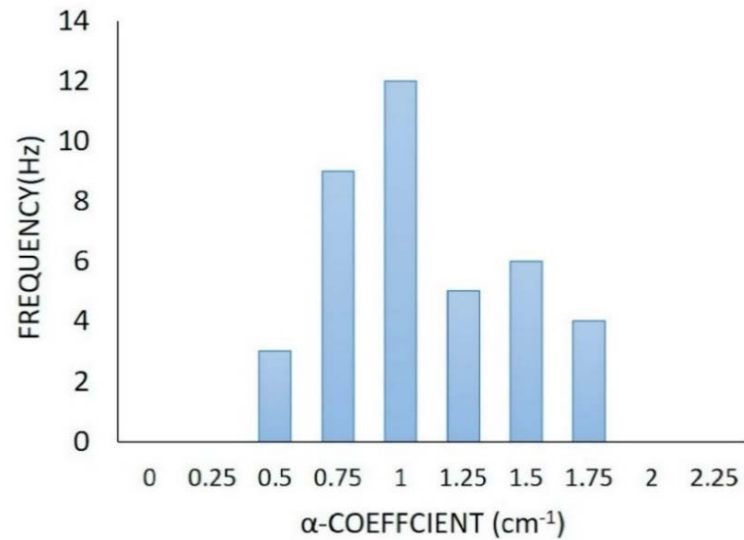


Figure 4.14: Attenuation coefficient of several fabricated waveguide structures

The investigation is further proceeded with the evaluation of the α coefficient along the length of the structure. This is operated by illuminating the light at the facet or ridge area of the several structures. The experimental investigation offers the reduction of the α coefficient with the increase in the tower dimension of the structure. The lesser attenuation is seen in tower dimension of $200\mu\text{m}$. This is fixed as minimal tower dimension of the fabricated structure comparing to other dimensions. The power transmitted at the output is maximal for tower dimension of $200\mu\text{m}$. The variation in light transmittance and tower dimensions α coefficient is displayed in the figure 4.15.

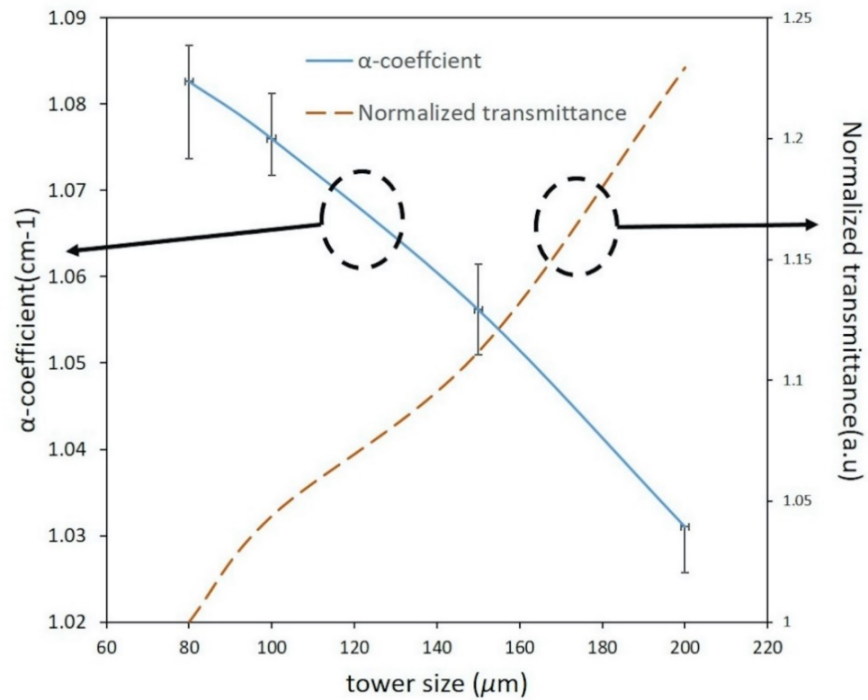


Figure 4.15: Tower dimensions α coefficient Vs normalized transmittance

4.5 Response Of The Single-Step Elevated Waveguide Structure

After the several investigations, the tower dimension of $200\mu\text{m}$ fabricated waveguide structure is further evaluated for vapor sensing by making use of the property of scattering concept. A vapor chamber is designed by 3D printing method i.e., fused deposition modeling (FDM) technology. Here, the 3D printer used in this work is Geetech Prusa I3 Pro W DIY. This designed vapor chamber holds a strong mechanical alignment of the components during experimental execution.

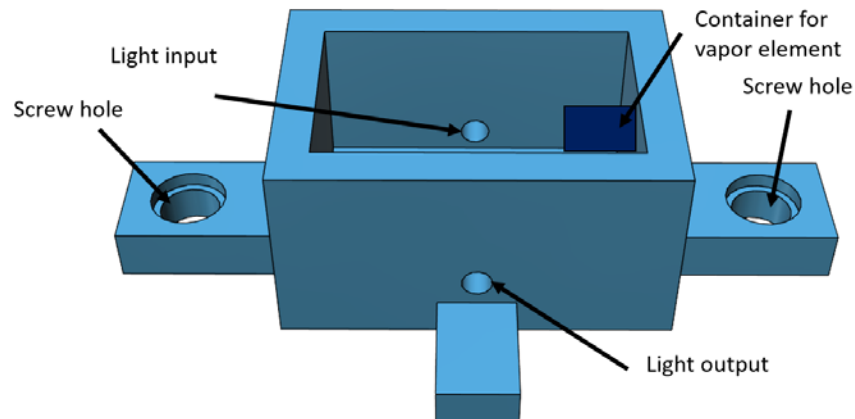


Figure 4.16: The 3D designed vapor chamber using Autodesk 123D CAD software for sensing analysis

The CAD of the chamber is implemented on the AutoDesk 123D software and is shown in figure 4.16. The designing involves the accurate mechanical alignment at the input and output section of the chamber where the fiber optic cables is used for signal collection. A small container of volume 8cm^3 is designed to deposit the different isopropanol alcohol ($\text{C}_3\text{H}_8\text{O}$) amounts. Here, the isopropanol alcohol (IPA) is taken as a vapor essential to distinguish the degree of changes in the environment inside the vapor chamber.

The block diagram for detection of vapor inspection is shown in figure 4.17. In this experiment, a warm white LED of 3000K is used to illuminate at the front side of the waveguide (i.e., the ridge region) that is placed inside the vapor chamber. The light is directed at the input section with the help of an fiber optic cable and the same is acquired at the output section using another fiber optic cable. The behavioral reading is taken using a powermeter (PM100USB, Thorlabs,

USA).

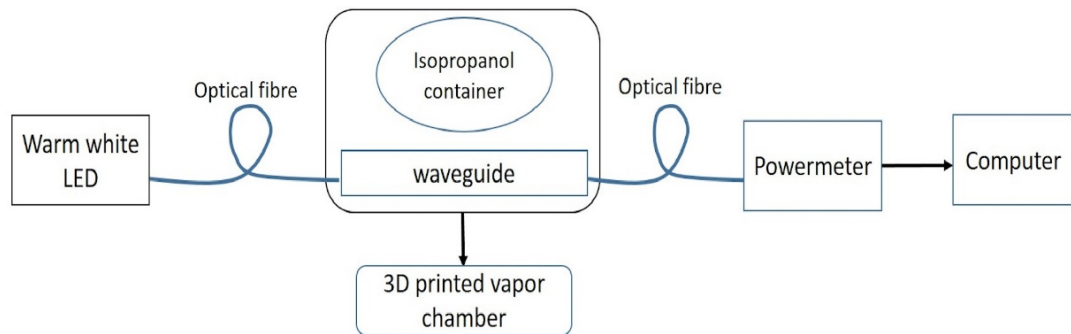


Figure 4.17: Block diagram for the experimental setup of vapor detection investigation

The investigation of vapor detection involves a 50 μ l and 100 μ l IPA amount/concentration. The IPA is dripped into the box container one at a time with pipette that ranges from (1-1000) μ l, and its acquired optical readings were stored using powermeter.

At first, the transmitted light is stored with air at an ambient room temperature for 5 minutes. After that, the IPA is dripped and enclosed with the 3D printed lid and the power is taken continuously until a saturation level is reached i.e., complete dissipation of IPA amount inside the vapor chamber. Later, the 3D printed lid is detached and the power is taken for another 5 minutes time. The figure 4.18 gives the evaluation from the powermeter of the transmitted power documented with time for 50 μ l and 100 μ l IPA amount.

The resulted graph below displays the immediate rise of the optical power after the vapor essential is dripped in the vapor chamber i.e., at around 200 seconds.

Yet, it displays a deliberate rise in the optical power that produces from the swelling property of the polymer resin i.e., Hexpolymer PX8880. This behavior comes in the picture from the diffusion IPA amount in the waveguide structure during interactivity among polymer and alcohol inside the vapor chamber. This is applied in this work as it is one of its unique property.

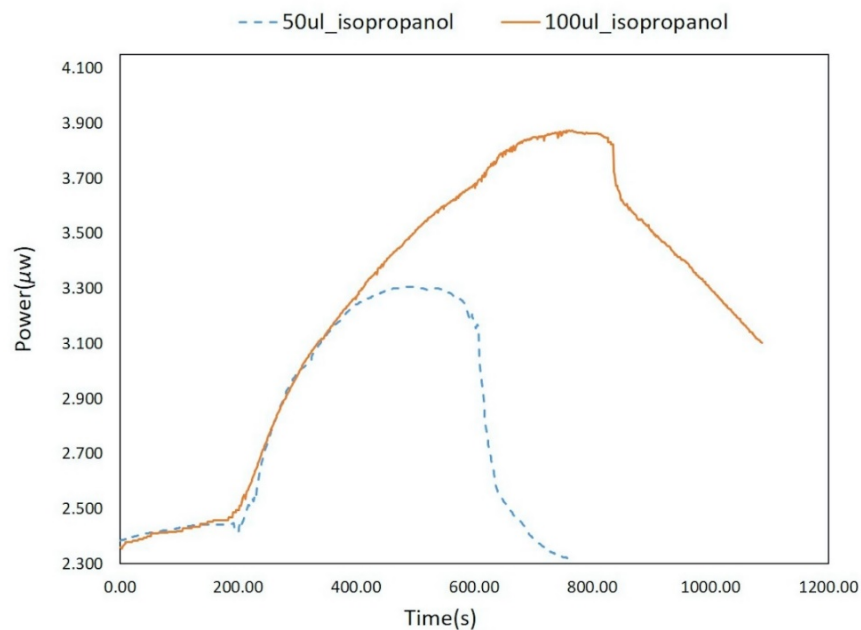


Figure 4.18: Optical power evaluation graph of 200µm dimension waveguide structure using 50µl and 100µl IPA amount

From the figure 4.18, it is noticeable that for 50µl IPA amount, the required time for the polymer swelling is short (i.e., transmitted power rise to complete saturation level) compared to 100µl IPA amount. The polymer swelling kicks off at the waveguide surface for both the IPA amount and it rises at a slower rate depending on the IPA amount used till it a saturation level is reached. The meaning

of this phenomenon is the structure of the waveguide index of effective in the tower and surrounding region decreases. Hence, the leakage of the transmitted power due to scattering which is generated from the surface roughness of the structure reduces and in the ridge part, peak increase of transmitted power is attained. With the achieved results, when different IPA amount is dripped, the fabricated optical system gave rise to variations in the transmitted optical power with time after a change in the ambience inside the vapor chamber is detected.

A clear light intensity variation is attained from a structure that is fabricated using a resin (Hexpolymer PX8880) by DLP technology. This technology excludes the expensive fabrication processes which involves a wide range of sophisticated process. The tower shaped waveguide structure of 200 μ m dimension provides a promising result in confinement of light in the ridge part comparing with different structure dimensions. The light scattering from the waveguides rough surface is also enumerated by image texture investigation.

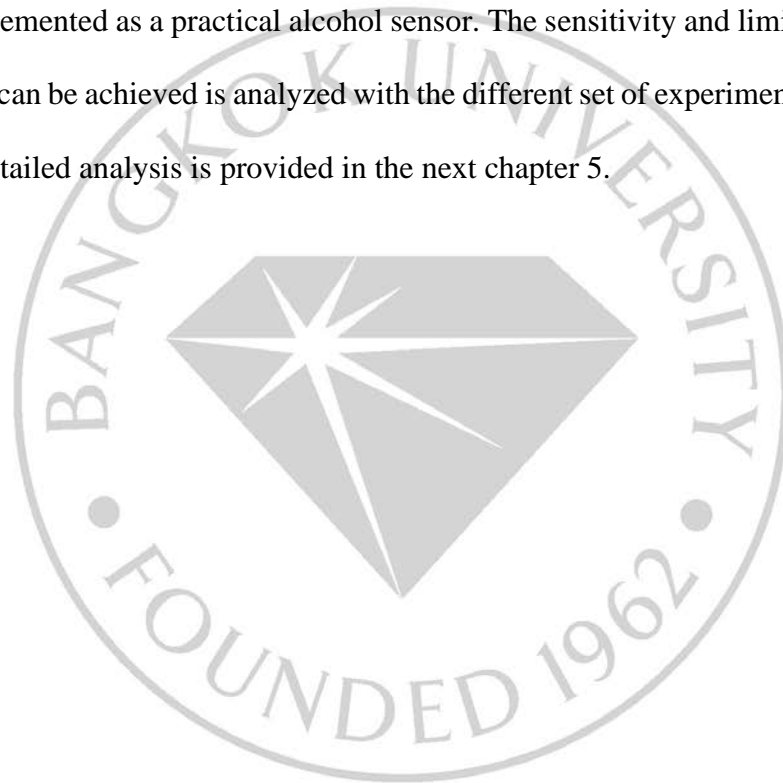
Ultimately, the 3D printed waveguide structure is also advanced for investigating the detection of vapor by a vapor essential i.e., IPA. The acquired results are for 50 μ l IPA amount, transmitted power increase is 39% and for 100 μ l IPA amount, transmitted power increase is 44%. The percentage of transmitted power increase is calculated by:

$$\%Power = \frac{Power_{increase} - Power_{initial}}{Power_{initial}} \times 100 \quad (4.6)$$

From this math, the light intensity variation was acquired from change of the

scattering that comes in picture when interaction between resin and vapor arises. This depicts that the 3D printed waveguide can perform as a definitive sensor. Even though the outlined feedback time is extensive, with thorough optimization it is possible to achieve a feasible time of operation.

Based on the aforementioned results, the tower-shaped waveguide structure is further developed by introducing a gap between the waveguide and it is implemented as a practical alcohol sensor. The sensitivity and limit of detection which can be achieved is analyzed with the different set of experiments conducted. The detailed analysis is provided in the next chapter 5.



CHAPTER 5

SINGLE-STEP TOWER-SHAPE GAP WAVEGUIDE STRUCTURE

A new design introducing a gap in the middle of the waveguide, i.e., along the horizontal region is presented in this chapter. It is based on the single step integrated optical system which is developed using 3D printer DLP technology that is presented in chapter 4. Using this configuration, an investigation is carried out with different gap dimensions and the structure with no gap. The study involves re-coupling of light concept, light scattering in the waveguide structure guiding region and swelling property of the material (i.e., photopolymer resin). The concept, fabrication and the experimental investigations are discussed in this chapter. The fabricated structure is also implemented as practical sensor without needing a vacuum system. The investigated criterion is the waveguide gap structures, the sensor chamber dimensions and the amount of IPA. The solutions for acquiring high sensitivity of the gap structure are its competence to achieve maximal confinement of power in the guided region when an interactivity occurs between the light, material and the IPA amount.

5.1 Design Of The Tower-Shaped Gap Waveguide Structure

The design approach for the tower-shaped gap waveguide is illustrated in the figure 5.1. Here, the tower shape one-piece structure is kept the same i.e., the ridge section height and width is $600\mu\text{m}$ and tower region height and width is $200\mu\text{m}$. The only modification implemented is introducing a gap which separates

the waveguide along the horizontal line in the ridge section. This gap is extended from (250-500) μm for choosing of minimal gap dimension that can be achieved by operating 3D DLP printer.

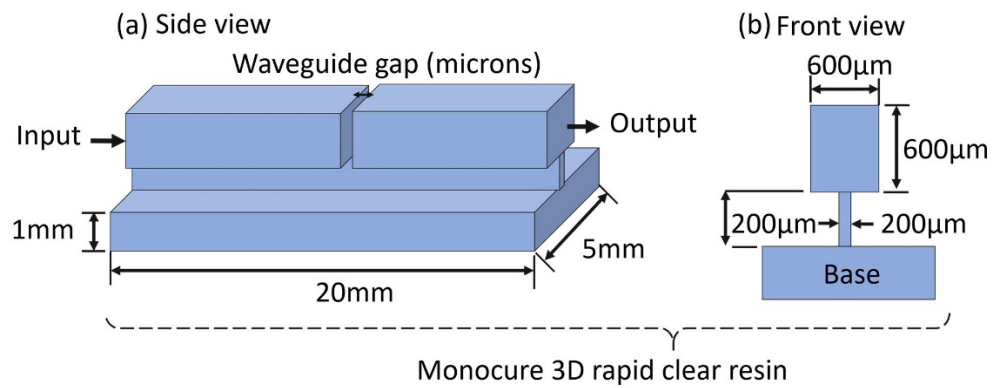


Figure 5.1: Design concept of the tower-shaped gap waveguide structure

In this work, the reason for introducing a gap is to make use of the light re-coupling principle that increases light confinement at the output when it interacts with the change of the refractive index at its surroundings. This concept is also combined by the swelling characteristics of the photopolymer resin which is detailed in section 5.4. The overall schematic and its designing concept of the gap waveguide structure with its size dimensions are shown in the above figure 5.1. Later, it is proceeded for fabrication using 3D printing DLP technology. In this work, the same 3D printer is used from the chapter 4 where liquid photosensitive clear photopolymer resin (MonoCure 3D rapid clear) with index of refraction, $n=1.50$ is taken. Since, the resolution of the 3D DLP printer in our work is of 50 microns, anything above these range can be printed. Table 5.1 shows the

dimensions of the gap that were set to design and fabricate.

Table 5.1: Discrete gap dimensions of the waveguide

Specimens	Width of ridge in μm	Height of ridge in μm	Width of tower in μm	Height of tower in μm	Dimension of gap in μm
Specimen 1	600	600	200	200	250
Specimen 2	600	600	200	200	300
Specimen 3	600	600	200	200	400
Specimen 4	600	600	200	200	500

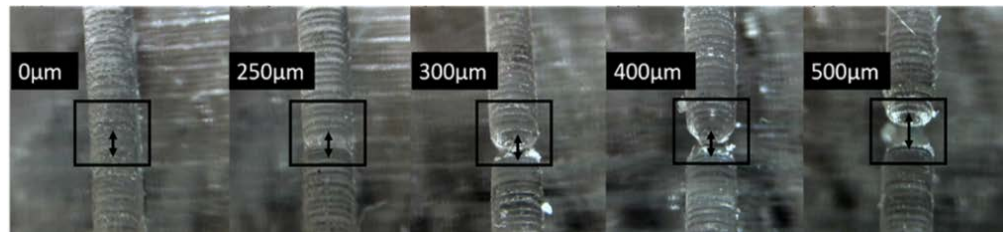
The 3D designed gap structure in the middle of the waveguide is extended from (250-500) μm for the choosing the minimum gap dimension that is possible to attain using 3D printer DLP technology.

5.2 Fabrication Of The Tower-Shaped Gap Waveguide Structure

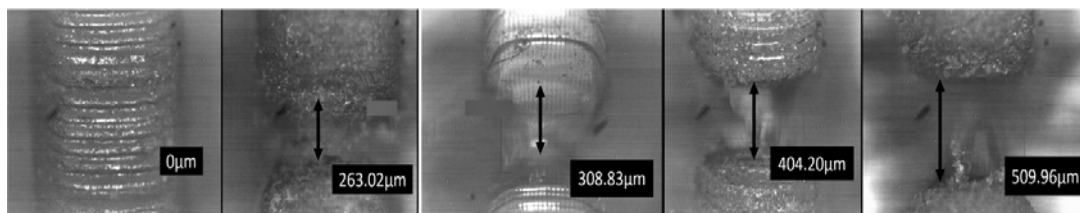
The fabrication steps involved are the same as detailed in the chapter 4 for tower-shape structure. This procedure is executed for all the different structures with a gap. For optimizing the designed parameters of the structure. Firstly, a CAD model is sketched and stored in .stl file format. Later, it is transfigured to .cws file format for 3D printing.

The 3D printed structures from the Wanhao Duplicator D7 Box 3D printer are shown in figure 5.2 (a) recorded using an USB type camera, (b) recorded using an OLYMPUS BX60 optical microscope (BX60F model) with 5x magnification at NECTEC (National Electronics and Computer Technology

Center), Thailand for measuring the original gap dimensions.



(a) Images from USB type camera



(b) 5X magnification images from optical microscope

Figure 5.2: Captured images of both designed and measured printed gap structures

The likeness of five different 3D designed gap and the original measured structures gap dimensions are displayed in the table 5.2.

Table 5.2: Likeness of the structures gap dimensions (3D printed)

No of specimen	3D designed gap dimensions in μm	Original measured gap dimensions in μm
Specimen 1	0	0
Specimen 2	250	263.02
Specimen 3	300	308.83
Specimen 4	400	404.20
Specimen 5	500	509.96

5.3 Design Of The Sensor Chamber

The goal of the fabricated structures with a gap is to implement it as a sensor for the practical use. Here, the gap structures were investigated as an alcohol-concentration sensor specifically for Isopropanol alcohol (IPA) detection. For this experiment, the printed structures are placed in a chamber for experimental measurements. The chamber is 3D designed with distinct dimensions for detecting IPA amount below 400ppm as stated by the National Institute for Occupational Safety and Health requirement. The distinct dimensions for the designed chamber are kept as 4cm x 2.5cm x 2cm (where volume is 20 cm^3 or 0.020 L). The 3D structure is shown in figure 5.3 that is designed using Autodesk 123D software and printed using 3D printer (Geetech Prusa i3 Pro W DIY, Shenzhen Getech Technology Co., Ltd, China). This 3D printer has a printer bed dimensions of 200x200x180mm with nozzle diameter of 0.3mm.

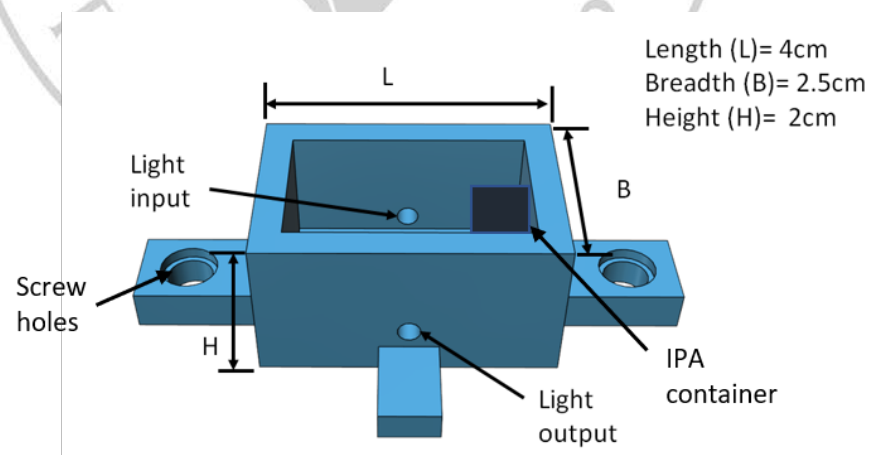


Figure 5.3: 3D designed sensor chamber structure with overall volume of 20 cm^3

The 3D printer employed in this work perform on FDM technology. Here, the designed structure prints in a layer-by-layer manner. The material used for printing is thermoplastic filament which is non-toxic and environmentally friendly. This chamber provides strong mechanical alignment stability at end to end when collecting the signal by the optical fiber cable where the fabricated gap waveguide is placed for the sensing analysis. In the sensor chamber, a small section is also made with the 3D printer for dropping the IPA. When performing the measurements, the IPA is deposited in that container and covered with a lid (3D printed). Since sensor chamber volume is 0.020L (converting it to liters), table 5.3 shows the IPA amount conversion from μL to ppm that is distinguished investigation of detecting alcohol by meeting the health standards. Here, PPM in numbers represents as quantity of isopropanol in $\mu\text{L} / 0.020 \text{ L}$.

Table 5.3: Isopropanol alcohol conversion (μL to ppm)

IPA amount (in μL)	CONVERSION	IPA amount (in ppm)
2.5		125
5		250
10		500

5.4 Principle Of Operation For The 3D Designed Waveguide Gap Structure

The detection principle of IPA concentration described in this section is to operate the 3D designed structure as an alcohol-concentration sensor. The

interactivity of photopolymer resin and alcohol in the 3D designed waveguide gap structure is examined by placing different IPA amounts inside the 3D designed chamber. In this work, the detection mechanism is intensified by an introduction of a gap in the middle of the designed waveguide. By doing so, the re-coupling of light from one waveguide to another is implemented. In addition, the detection mechanism of the structure is also applied on the basis of scattering concept which occurs due to surface roughness generated from the 3D printing process and secondly from the property of swelling of the polymer. The transmitted light intensity variation is noticed when an interactivity of photopolymer resin and alcohol occurs. Thus, the structure changes from a leaky to a guided mode waveguide. The technique of implementing this principle of operation is shown in the figure 5.4.

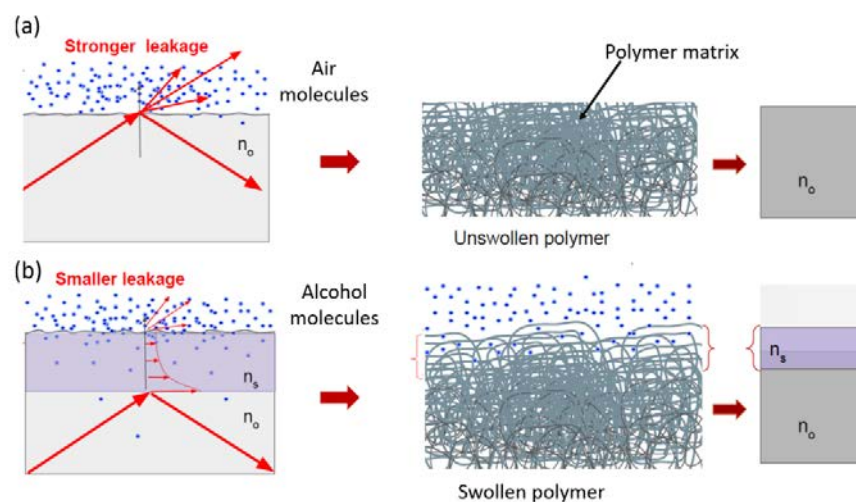


Figure 5.4: Concept of scattering and swelling property of polymer (a) Interaction process between polymer and air (b) Interaction process between polymer and alcohol

The structure encounters huge scattering when not exposed to alcohol due to surface roughness. This results in massive leakage of transmitted light. When the structure is introduced to alcohol, the two important process occurs. (1) During the structures introduction to alcohol, the minute molecules of alcohol get immersed inside the polymer (where the polymer refractive index is n_0). This gives rise to swelling of the polymer that occurs inside the polymer matrix thus leading to a new cladding layer construction (where the cladding refractive index is n_s) in the upper portion of the structure. In general, a photopolymer consists a polymer matrix which has an empty space in them. When alcohol diffuse inside the polymer, they fill up the empty space in the polymer matrix and results in swelling. The cladding layer (n_s) formed from the polymer swelling has comparatively small refractive index than that in the core layer of the structure.

(2) The transmitted light leakage i.e., mainly due to forward scattering decreases due to the construction of new cladding layer and its increase in thickness from the swelling property of the polymer. Prior to that, the degree of intensity of light lessens to reach the surface of the structure thus induces the light far better into the core layer.

This mode of operation is carried out in this work and in the figure 5.5, it is shown that by introducing a gap in the middle of the 3D designed structure, the light is induced strongly to the next portion of the waveguide structure which follows the re-coupling of light concept. With this, the overall index of refraction of the cladding area including the area near the tower portion decreases. This furnishes the waveguide structure to a guided type and at the end of the output

area, higher transmitted light is observed. Implementing this principle of operation, the alcohol detection can be evaluated from the variation in the intensity of light when dripping different amounts of alcohol inside the sensor chamber.

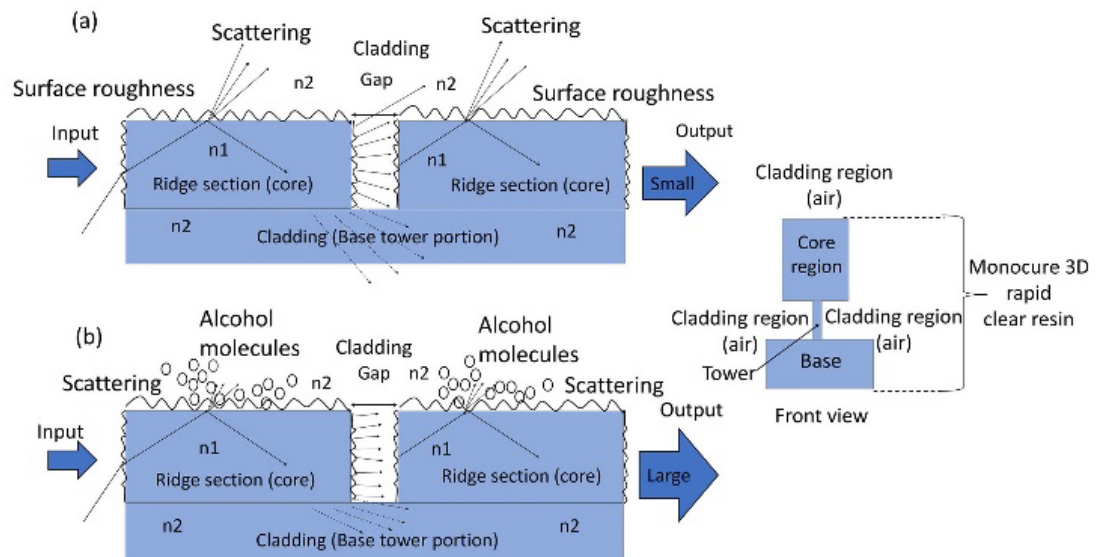


Figure 5.5: Operating principle of 3D designed waveguide gap structure (a) Leaky-type gap structure (b) Guided-type gap structure

5.5 Response Of The Tower-Shaped Waveguide Gap Structure

The developed waveguide gap structures are tested by placing the structure inside the sensor chamber. The experimental setup for the testing of the waveguide gap structure is shown in figure 5.6.

The sensor chamber with the waveguide structure placed inside is connected via fiber optic patch cable that has a diameter of $200\mu\text{m}$. This fiber optic patch cable is attached both in the input and output side of the chamber. A 3000K warm white LED light being excited by a LED driver (LED1BB, Thorlabs,

Newton, NJ, USA) at certain intensity of current at 0.7A is directed at the input side through fiber optic patch cable. The transmitted light intensity from the waveguide structure is acquired with the fiber optic patch cable at the output side which is connected to a powermeter (PM100USB, Thorlabs, Newton, NJ, USA). Finally, the data is investigated using a computer.

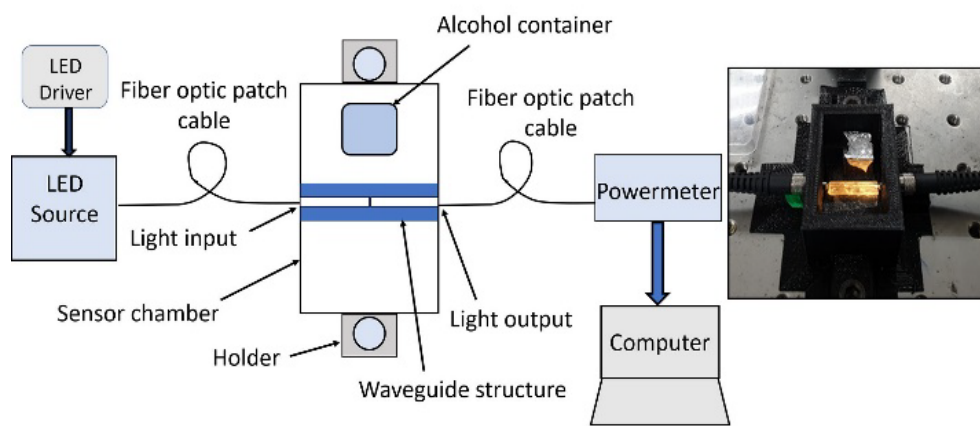


Figure 5.6: Experimental setup and schematic diagram for testing waveguide gap structure

For sensing of the developed samples, three volumes of IPA amount of $2.5\mu\text{l}$, $5\mu\text{l}$ and $10\mu\text{l}$ are placed onto the alcohol container inside the chamber for the investigation. All the three volumes of IPA amount were tested and compared for each waveguide gap structures ranging from $250\mu\text{m}$ to $500\mu\text{m}$ including the waveguide without gap structure. Due to the limitation of the 3D printer and its resolution of 50 microns, the waveguide gap structure of dimension $100\mu\text{m}$ and $200\mu\text{m}$ failed to print. Therefore, the waveguide gap structures above $200\mu\text{m}$ are investigated in this work thereby selecting the minimum gap dimension upon

performing numerous experiments. The whole system (sensor chamber) is adjusted by exciting the LED light for 200 to 300 seconds. This is done every time by a pipette before setting down the different IPA amount in the alcohol container inside the sensor chamber.

After placing the required IPA amount, the sensor chamber is covered with the lid that is designed by 3D printer FDM method. The transmitted light intensity from the waveguide structures is then acquired using a powermeter till the optical power reaches a saturation level. After that, the lid is then removed and decreasing optical power is seen which slowly decrease to its original power when measured with air. The IPA amount is placed again inside the chamber when the optical power decrease to its original power. This entire process is performed three times to investigate the repeatability feedback of the waveguide structures for the different IPA amounts.

5.5.1 Repeatability Response Trend Of The Tower-Shaped Waveguide Structure

The structure without the gap is initially tested first with the three different concentrations of IPA and it is recorded using powermeter. Figure 5.7 shows the responses of the waveguide during interaction process of alcohol-photopolymer resin inside the sensor chamber.

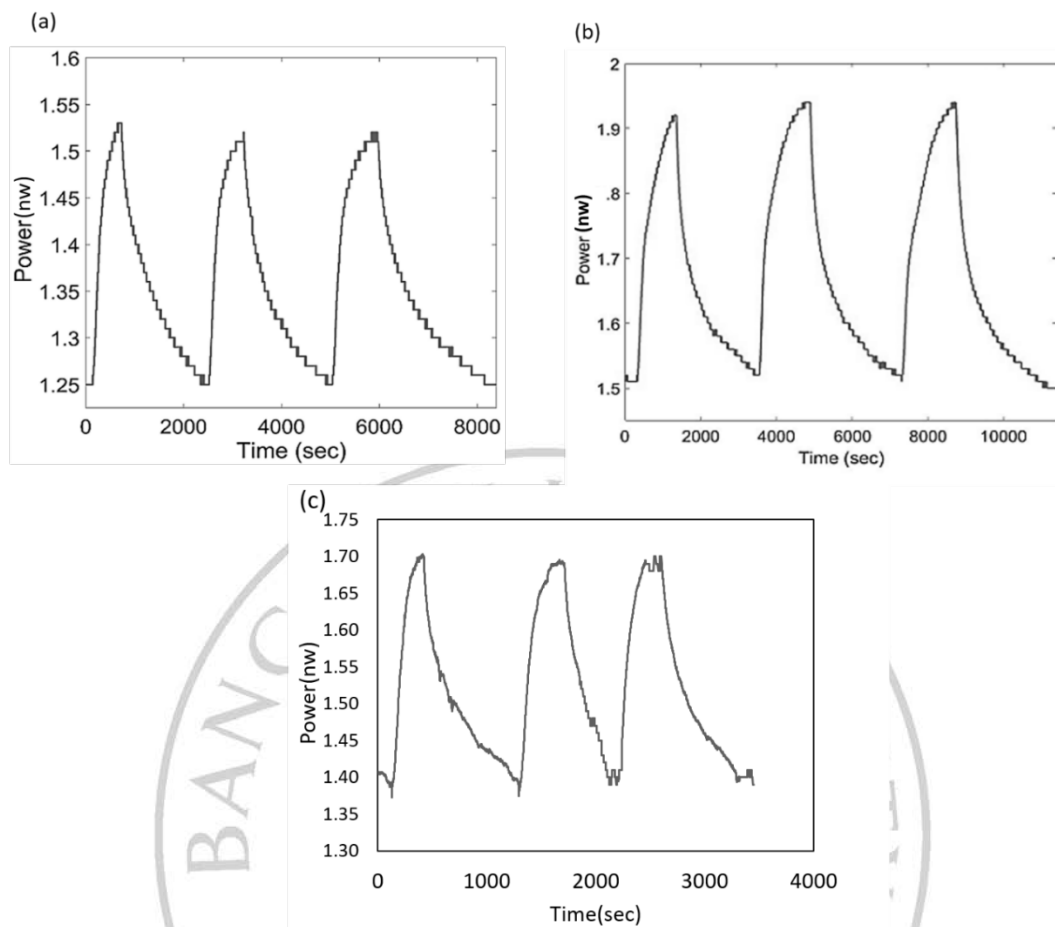


Figure 5.7: (a) Repeatability response of the sensor with 125 ppm concentration of IPA (b) Repeatability response of the sensor with 500 ppm concentration of IPA (c) Repeatability response of the waveguide with 250ppm concentration of IPA

From these responses, it can be observed that every time when IPA is deposited in the sensor chamber, there is an increase in optical power until it reaches its peak. This means, the swelling effect of the polymer resin can be observed when interacting with IPA resulting in different change in the transmitted power for different concentrations. Removing the sensor chamber lid, a sudden change of

environment occurs resulting in decrease of the optical power and it settles to previous levels (similar level before dropping IPA).

5.5.2 Response Of The Different Tower-Shaped Waveguide Gap Structure

For all the different waveguide gap structures, firstly a testing is carried out with 5 μ l or 250ppm IPA amount to examine the behavior of the structures response and its capability of detecting IPA below 400ppm as per National Institute for Occupational Safety and Health.

The light is kept constant for testing all the different waveguide gap structures and is launched in the chamber. After that, the desired IPA amount is placed in the allotted area which is inside the chamber. The experimental results acquired from testing the different waveguide gap structures with 250ppm IPA amount are shown in the figure 5.8.

It is noticeable that there is a variation in the rise of the optical power for all the different waveguide gap structures. The response time variation of increase in optical power for the different gap structures is shown in figure 5.8. From the graph, it is seen that the increase in optical power is highest for the structure with a gap of 300 μ m when comparing with the other gap dimensions.

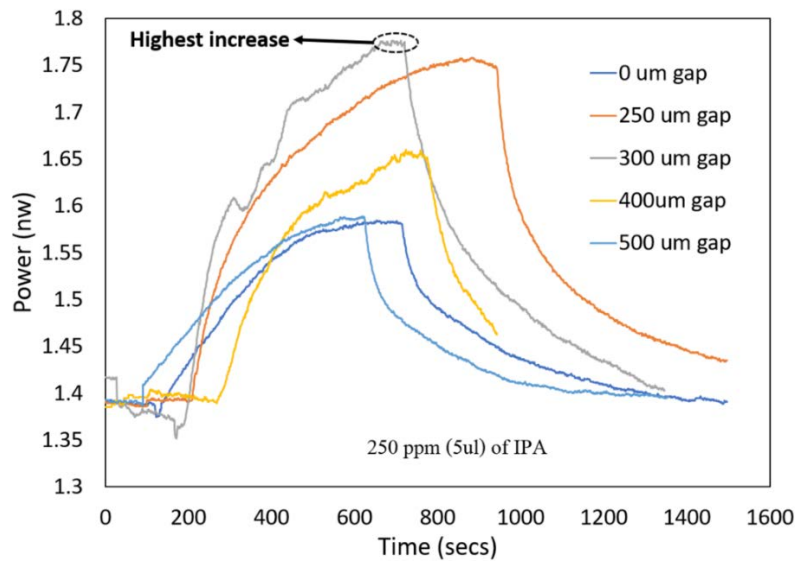


Figure 5.8: Response time variation of the different gap sizes of the waveguide structures with 5 μ l (250ppm) concentration of IPA

From the above graph, it is observed that for the different waveguide structural gap sizes, its response behavior is similar. The optical power rises till it becomes stable after every deposition of IPA amount in the allotted place of the chamber. When removing the chamber lid, gradual decrease in the value of the optical power is observed which later restores to its original value i.e., value of the optical power before dropping IPA amount. The nature of this behavior shows a reversible process. In addition, it also displays a type of sensing response, that comes into an effect because of the swelling characteristics of the material (photopolymer resin) as well as light re-coupling and scattering effect.

When the chamber lid is removed, the structure of the photopolymer matrix transforms to its original form. This occurs from the evaporation of IPA molecules in the room temperature. However, the rising and the falling time graph

vary because of the size of the gap for the particular IPA amount.

Based on the above figure 5.8, it is clearly observable that the fabricated structures responded lower than 400ppm limit of IPA amount. To analyze the possibility of structure that responds to much lower concentration, further experimental analysis is executed for different IPA amount for different sizes of the gap. The experimental work was repeated for three times for the different size of the gap, including the structure without a gap. This was executed to check the repeatability behavior of the response of each different structure. The obtained increase in average percentage optical power for each different structure is shown in the table 5.4.

The calculation involved to obtain increase in percentage optical power of different structures for different IPA amounts is given by:

$$\%Power = \frac{Power_{increase} - Power_{initial}}{Power_{initial}} \times 100 \quad (5.1)$$

where, $P_{increase}$ is the highest rise in the power after depositing IPA amounts and $P_{initial}$ is the initial power recorded with air for a certain amount of time before depositing IPA amounts. Here the value of $P_{initial}$ is between 1.36nw to 1.42nw.

Table 5.4: Comparison table between different waveguide gaps (in percentage) to different IPA amounts

Amount (μl or ppm)	% Power increase (250 μm gap)	% Power increase (300 μm gap)	% Power increase (400 μm gap)	% Power increase (500 μm gap)	% Power increase (No gap)
2.5 or 125	20.95	26.66	16.11	11.17	15.17
5 or 250	29.75	30.61	18.76	17.70	21.60
10 or 500	44.99	64.14	22.25	28.59	27.40

With the above obtained results, the structure with the different sizes of gap displays a variation in optical power. And it leads to an agreeable IPA-concentration sensor with its nature of operation. However, for choosing a best sensor, a precise gap size of the waveguide with fast response time for variation in the optical power immediately after dropping IPA and higher system sensitivity must be taken into account. For these mentioned points, a deep analysis is needed. The waveguide gap structure of 300 μm size is the most promising one to that of other structures as shown in table 5.4. The other structures show a reduction of optical power. To explain the physical phenomenon, the following figure 5.9 is shown.

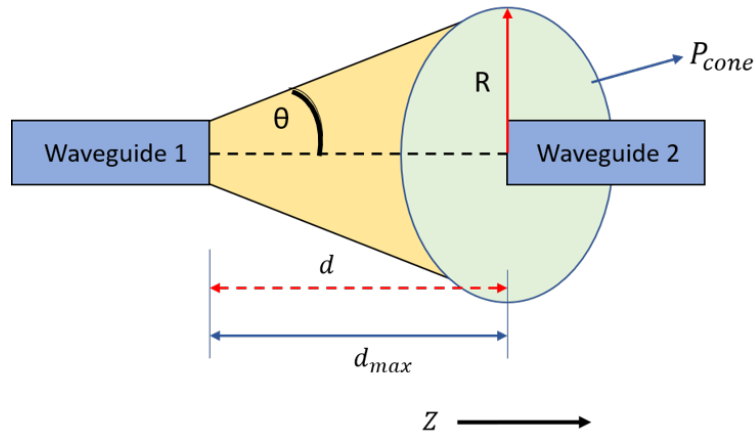


Figure 5.9: Schematic showing the light coupling and numerical aperture effect from the waveguide 1 to waveguide 2

Assuming that the transmitted light/power emitted from the 1st waveguide (size of 600 μm) is diverging in a cone shape and have an intensity over a certain distance. Then, the power of the cone shape is defined as:

$$P_{\text{cone}} = I_{\text{intensity}} \times A_{\text{cone}}$$

$$P_{\text{cone}} = I_{\text{intensity}} \times \pi R^2 \quad (5.2)$$

where A_{cone} is the area of the cone shape. When the 2nd waveguide is placed in between the area of the cone shape, the power guided (P_{guide}) inside the 2nd waveguide from the 1st waveguide is defined as:

$$P_{\text{guide}} = I_{\text{intensity}} \times A_{\text{wg}} \quad (5.3)$$

where A_{wg} is the area of the waveguide 2. The coupling efficiency (η) is related due to the gap (specific distance). It is measured from the 1st waveguide (emitted

light) to the 2nd waveguide (where the light is coupled). The obtained equation from this measurement is given by:

$$\eta = \frac{P_{guide}}{P_{cone}} = \frac{A_{wg}}{\pi R^2} \quad (5.4)$$

Where $R = d_{max} \tan \theta$ is the radius of the cone and 'θ' is the acceptance angle of the numerical aperture and it is obtained by exciting white light in the waveguide.

The different sizes of gaps were selected in order to support enough coupling of power from the input side of the waveguide i.e., from the waveguide 1 to the waveguide 2. This is defined by the maximum gap, d_{max} where the coupled power is reduced to $\frac{1}{e}$ or e^{-1} from the 1st waveguide input.

This is given by, (from equation 5.4)

$$\eta = \frac{P_{guide}}{P_{cone}} = e^{-1} = \frac{A_{wg}}{\pi (d_{max} \tan \theta)^2}$$

So,

$$d_{max} = \frac{A_{wg}}{\tan \theta \sqrt{\pi e^{-1}}} \quad (5.5)$$

The experimental calculation of the numerical aperture acceptance angle (θ) is carried out with a number of readings with varying distance (d) along the z-direction till the intensity is faded.

The experiment is performed by measuring the diverged light coming out from the waveguide on a piece of paper. The distance from the waveguide and the diverged light (waveguide area on a piece of paper) was measured with a scale. The data were taken till the intensity of light faded at certain distance (approx.

1cm). the obtained graph is shown in the figure 5.10.

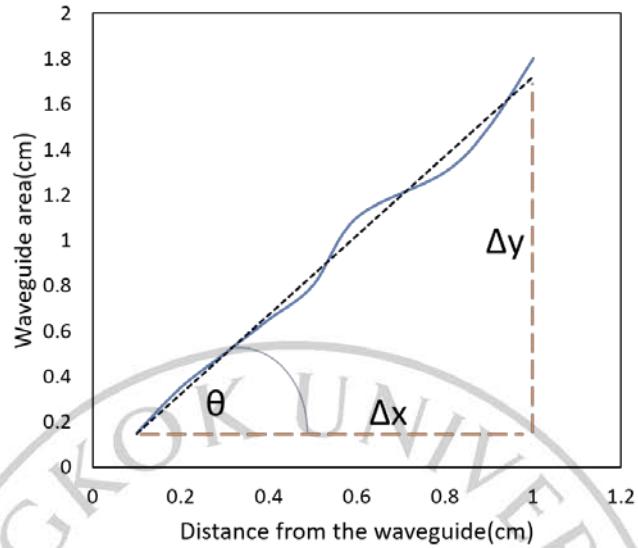


Figure 5.10: Acceptance angle calculation from the measured number of readings

The calculated numerical aperture acceptance angle (θ) is (from the slope of the line):

$$\tan \theta = \frac{\Delta y}{\Delta x} = \frac{y_2 - y_1}{x_2 - x_1} = \frac{1.8 - 0.15}{1 - 0.1}$$

$$\tan \theta = \frac{1.65}{0.9} = 1.833333$$

$$\theta = 61.344 \quad (5.6)$$

Putting the value of θ in the equation (4), the d_{max} is calculated as:

$$d_{max} = \frac{600}{\tan 61.344 \sqrt{\pi e^{-1}}} = 305.0486 \mu\text{m}$$

From the obtained $d_{max} = 305.0486 \mu\text{m}$, it is noticeable that the light coupling

is possible within this distance (gap) and above that the optical power will reduce. This corresponds to our designed waveguide structure of $300\mu\text{m}$ gap.

Based on the numerical aperture calculation and size of the designed waveguide, the maximum feature size of the structure is found to be of $300\mu\text{m}$. Therefore, the waveguide gap of $300\mu\text{m}$ were further experimented for its validation as a practical sensor.

The waveguide gap of $300\mu\text{m}$ was tested with different concentrations of IPA. On the other hand, humidity and temperature were also monitored simultaneously. For that, a DHT 11 commercial sensor was connected in the 3D printed chamber using Arduino board. The set-up is shown in the figure 5.11.

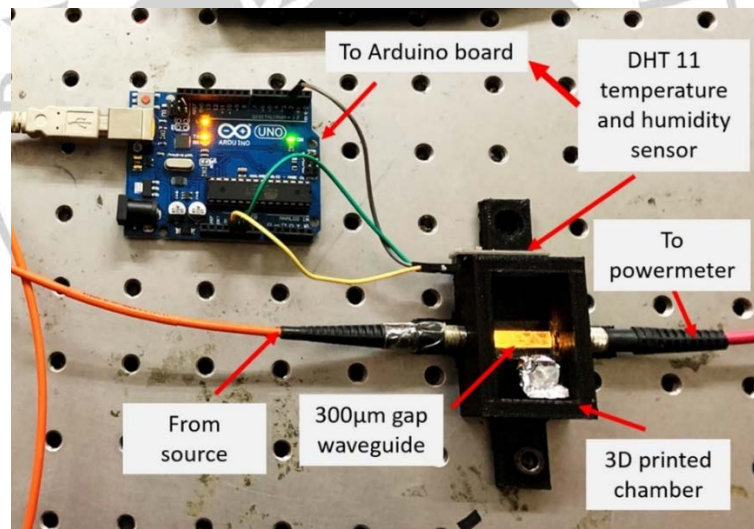


Figure 5.11: Experimental set-up of humidity, temperature and optical power measurement

The humidity and temperature measurement reading are shown in the figure 5.12. It is seen that the experimental measurement with the air for (200 to 300) seconds

displays around 1.40nw of optical power. This power is stable after every measurement performed with different IPA amounts. When the IPA amount is increased, the variation in the optical power, temperature and humidity is clearly observed. This shows an obvious effect with the increasing IPA amount inside the sensor chamber. This experiment was performed in the ambient room temperature at 22°C.

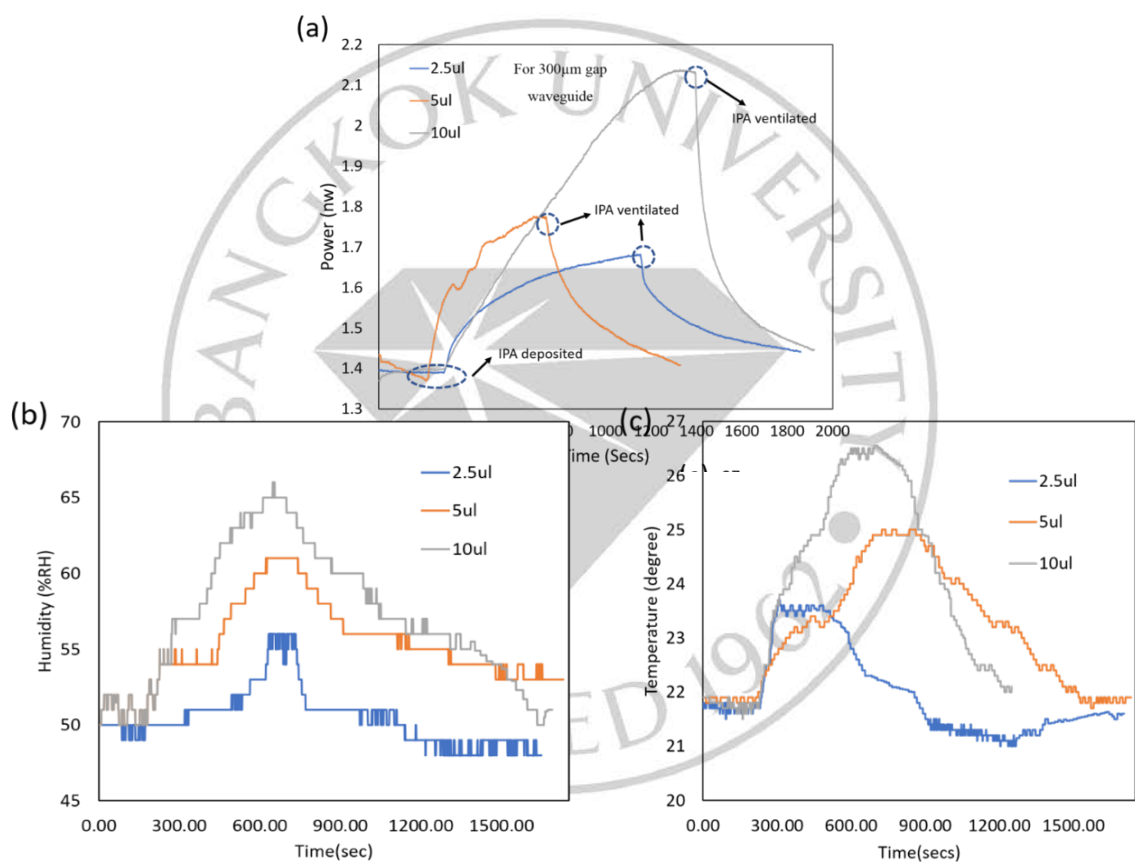


Figure 5.12: Response time measurement of waveguide gap structure of 300µm (a) Transmitted power (b) Humidity and (c) Temperature

The highest increase in transmitted power is seen when measuring with the amount

of IPA of 500ppm. As shown in figure 5.12, it is also possible to measure with the amount of IPA of 125ppm. Using this amount, the transmitted power is the highest when comparing with the other gap structure. Thus, this structure with a gap of 300 μm assures the potential of measuring and detecting lower than the amount of IPA of 400ppm as stated by the health standards presented in section 5.3. Furthermore, a complete comparison graph of different gaps with the increment in the transmitted power for all the concentrations of IPA is shown in figure 5.13.

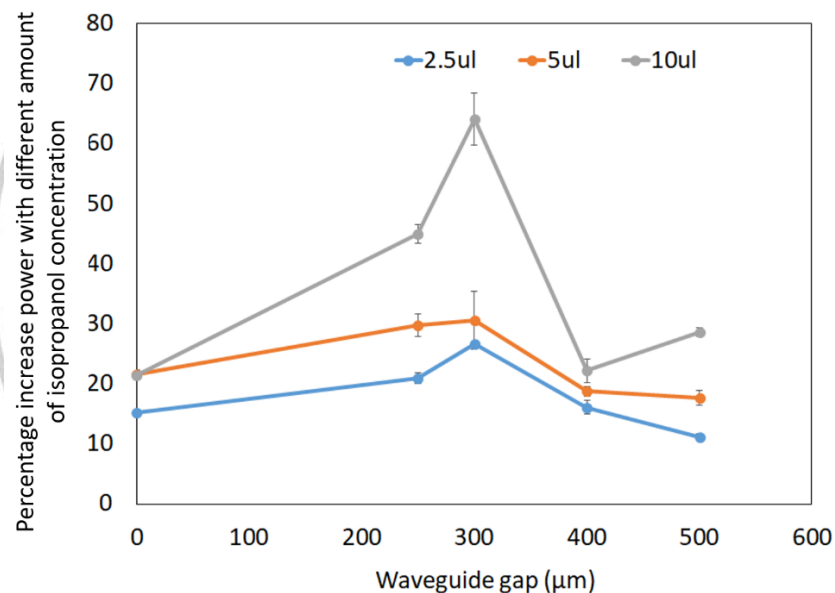


Figure 5.13: Comparison graph of different gap structures along with percentage increase power

From table 5.4 and figure 5.13, it can be seen that the maximum increment in the transmitted power is achieved with the waveguide gap structure of 300 μm when comparing it with the other gaps. The rise in the power occurs from the diffusion

of IPA molecules inside the structure. It differs with the amount of IPA used. With this characteristic, the light scattering is minimized and stronger light re-coupling is achieved with the presence of gap. Furthermore, with the amount of IPA of $10\mu\text{l}$ (500ppm), 65% increment of transmitted power displayed the highest among the other gaps. Also, with the lower amount of IPA of $2.5\mu\text{l}$ (125ppm), 27% increment of transmitted power displayed the highest among the other gaps.

With these results, the Limit of Detection (LOD) along with the sensitivity of different gap structure is performed using statistical analysis and the results obtained are shown in figure 5.14.

The calculation of LOD is repeated 3 times for all the different fabricated gap structures, that includes the structure with and without gap. This is performed for investigating the variation in the optical power of the fabricated structures for different concentrations of IPA in the allotted place inside the designed chamber. The calculated results are shown in table 5.5 for different fabricated waveguide gaps structures.

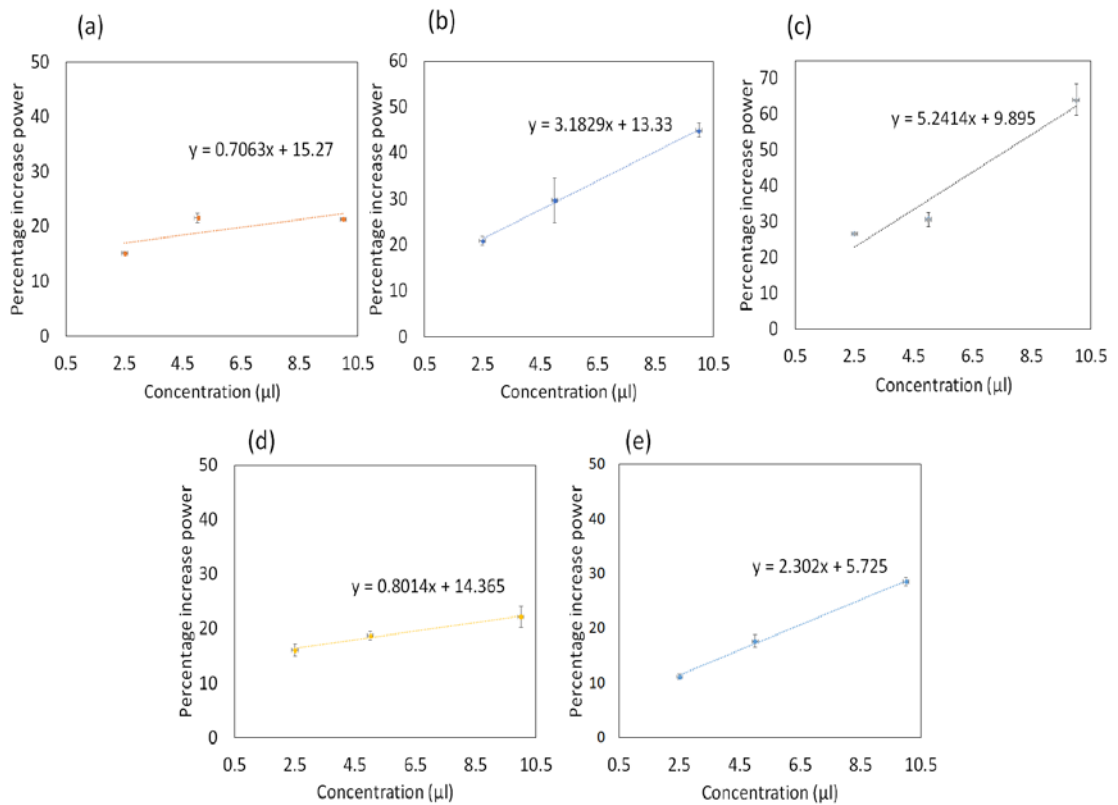


Figure 5.14: LOD calculations for different gaps: (a) $0\mu\text{m}$, (b) $250\mu\text{m}$, (c) $300\mu\text{m}$, (d) $400\mu\text{m}$, (e) $500\mu\text{m}$

The measurements of LOD for different gaps is calculated from 3 repeated times. This is done for all the different fabricated waveguides, i.e., waveguide without a gap and with a gap. The formula is as follows:

$$LOD = \frac{Std_{wg}}{S_{lcc}} \quad (5.7)$$

Where Std_{wg} is the standard deviation and S_{lcc} is the slope of the linear calibration curve of each of the measured waveguide gap. This is performed for investigating a variation in the optical power displayed by different waveguide gaps that is

produced by depositing different concentrations of IPA in the allotted place inside the designed chamber.

Table 5.5: Limit of Detection (LOD) of different fabricated gap dimensions

Waveguide gap dimensions (μm)	LOD in amounts (μl)
0	1.142
250	1.515
300	0.366
400	2.450
500	0.508

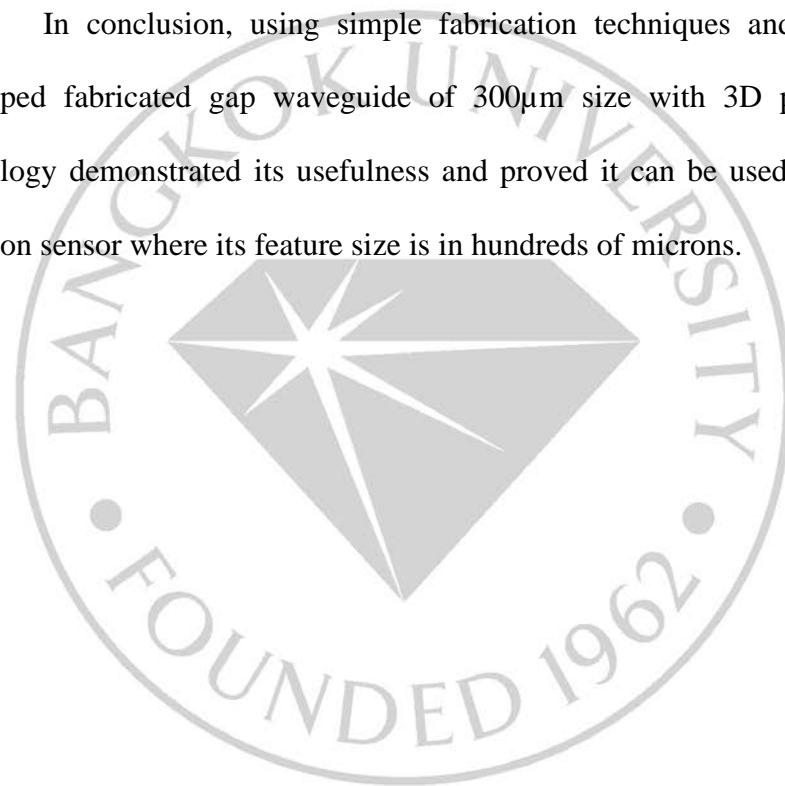
From the calculated results, the waveguide gap of $300\mu\text{m}$ size acquired the LOD of $0.366\mu\text{l}$ which is best of all the other gaps. The $300\mu\text{m}$ size displays a change in the intensity of transmitted light at a least amount of $0.366\mu\text{l}$ that is considered as a favorable one for detecting a variation in the optical power. This also corresponds to the sensitivity that a developed system produced.

Moreover, the faster response time in the increase of transmitted optical power after depositing IPA in the sensor chamber is achieved due to the change in the surroundings. It occurs from swelling characteristics and diffusion of IPA molecules in the fabricated gap structure of $300\mu\text{m}$ size. This gap displays the measurement response about 5 seconds faster than all the different amounts of IPA compared with different waveguide gaps and waveguide without a gap.

Based on these results, it is validated that the operating principle of

photopolymer resin-based tower-shape gap waveguide performed in this work is found to be effective. The given waveguide structure of 300 μm gap dimension demonstrated as valid alcohol detection sensor by encountering the conditions (limit of detection based on alcohol amounts, stronger confinement of light, highest increasing transmitted optical power and faster detection time response which below 400ppm amount of IPA exposure limit).

In conclusion, using simple fabrication techniques and design, the developed fabricated gap waveguide of 300 μm size with 3D printing DLP technology demonstrated its usefulness and proved it can be used as a alcohol detection sensor where its feature size is in hundreds of microns.



CHAPTER 6

CONCLUSIONS AND FUTURE WORK

In this research work, the design, fabrication and characterization (theoretical and experimental) of a 3D printed polymer-based optical waveguide for sensing applications, were performed and presented. Two different types of polymer-based optical waveguides were investigated using 3D printing DLP technology.

In the first design, an elevated/tower-shaped waveguide structure is fabricated. This structure, i.e., the guiding region and substrate region is fabricated with same material. By doing so, higher confinement of light is achieved in the guiding region when light strikes at the face of the waveguide. In the second design, the structure is an extension of the tower-shaped waveguide where the modification occurs with the introduction of a gap between the ridge section (guiding region) of the waveguide (along the horizontal line). Using this design, higher confinement of light and higher transmitted light intensity is achieved at the ridge section than the first designed approach by employing light re-coupling principle and polymer swelling behavior upon the interaction with analyte.

In the first approach, the designing of the tower-shaped waveguide is a new approach where the guide and the substrate region are fabricated as a one-piece structure using 3D printing DLP method incorporating resin (Hex-polymer PX8880) as its material having refractive index of $n=1.4759$. A FEM numerical approach is conducted to check the field distribution of the modes in the ridge

section of the fabricated waveguide structure by optimizing and varying the parameters for the tower region in order to obtain the least feature size. A 200 μm tower size gave a strong power confinement in the ridge section when comparing with other tower dimensions with the ridge section of the fabricated structure set to 600 μm width and height. The fabrication of the tower region is limited by the resolution of the 3D DLP printer due to the limitation of the 3D DLP printer slicing resolution of 50 microns. This limitation is also discussed and reported since the obtained structure had a rough surface and caused scattering of light. The texture analysis was also conducted for the rough surface generated during the printing of the structure using GLCM method which includes contrast and correlation measurements that helped in quantifying the images of the fabricated structures. Furthermore, the fabricated structure is examined for vapor detection by placing IPA inside the chamber. This chamber is printed using 3D printer FDM technology for strong mechanical alignment thereby reducing the overall cost of the experimental set-up. The achieved results are for 50 μl amount of IPA, increase of 39% in transmitted light intensity and for 100 μl of IPA, increase of 44% in transmitted light intensity can be observed. This intensity dynamics were achieved due to the variation of optical scattering that occurs during polymer resin and vapor interaction where the obvious dynamics were reported. With this, the fabricated structure demonstrates the potential of implementing it as a practical operating sensor.

For second approach, a gap is introduced in the fabricated tower-shaped waveguide horizontally with the intention to increase the its sensitivity as

compared to one without a gap with the analyte. This is also taken into account of the swelling behavior of the resin (Monocure rapid 3D clear resin) having refractive index of $n= 1.5017$ and re-coupling of light principle that is utilized due to a gap region. It results in enhancing the stronger light confinement. The surface roughness that is generated from the printing is also utilized. Various dimensions (250 μm , 300 μm , 400 μm and 500 μm) of the gap were optimized for the least feature size in order to achieve higher confinement of light in the ridge section of the waveguide structure. Three different amounts (2.5 μl , 5 μl and 10 μl) of isopropanol alcohol (IPA) are tested in a sensor chamber which is designed and developed using 3D printing FDM technology for strong mechanical alignment and proper characterization of the fabricated structure. This is taken to follow the exposure limit safety requirement of IPA which is of 400ppm as given by “National Institute for Occupational Safety and Health”. From the analysis measurements, 300 μm gap is five seconds faster in detecting response compared to other gap size. It also provided a stronger transmitted optical power of 65% at 500ppm and of 27% at 125ppm compared to other dimensions and responded to changes in the environment inside the sensor chamber below the exposure limit of 400ppm. With this configuration, the LOD (Limit of Detection) calculated for the 300 μm gap is found to be 0.366 μl which corresponded to the system sensitivity. Therefore, this fabricated optical system demonstrated its potential as a waveguide-type alcohol detection sensor.

The overall research work demonstrated a simple low cost and fast fabrication technique which was utilized to develop a resin-based optical

waveguide for optical sensing applications. This new approach overcome the need for the vacuum system for the fabrication process, thus reducing the cost of the overall system. The 3D printer DLP machine in our work is limited to print/fabricate lesser resolution size (50 microns) than what was fabricated in our designed and using a higher resolution 3D printer can lead to fabricate other type of integrated devices where there is possibility to print lesser than 50 microns since it also depends on the type of material (resin) that is supported for the printer.

Future work may investigate the development of an integrated optical waveguide system with the optimized introduction of two gaps that can be used for potential detection of other types of alcohol with the lower concentration with enhanced transmitted optical intensity and light coupling. There is also a potential to develop other types of integrated optical devices by using 3D DLP printing technology for example, Mach-Zehnder interferometer, waveguide splitters and waveguide connectors where the dimensions are in microns and can be fabricated without using a vacuum system. The advantage of fabrication using the 3D printing technology is the cost-effective and the rapid printing to develop integrated devices where it can lead to specific outcomes in improving the quality of research, less complexity for innovation work and huge mass production in market.

BIBLIOGRAPHY

- Ali, B., & Jianyong, J. (2019). Photopolymerization in 3D printing. *ACS Applied Polymer Materials*, 1(4), 593-611.
- Almeida, V. R., Xu, Q., Barrios, C. A., & Lipson, M. (2004). Guiding and confining light in void nanostructure. *Optics Letter*, 29(11), 1209–1211.
- Arrand, H. F., Benson, T. M., Sewell, P., Loni, A., Bozeat, R. J., Arens-Fischer, R., Krüger, M., Thönissen, M., & Lüth, H. (1998). The application of porous silicon to optical waveguiding technology. *IEEE Journal on Selected Topics in Quantum Electronics*, 49(6), 975-982.
- Bamiedakis, N., Beals, J., Penty, R. V., White, I. H., Degroot, J. V., & Clapp, T. V. (2009). Cost-effective multimode polymer waveguides for high-speed on-board optical interconnects. *IEEE Journal of Quantum Electronics*, 45(4), 415-424.
- Baumann, I., Bosso, S., Brinkmann, R., Dinand, M., Greiner, A., Schafer, K., Sochtig, J., Sohler, W., Suche, H., & Wessel, R. (1996). Er-doped integrated optical devices in LiNbO₃. *IEEE Journal of Selected Topics in Quantum Electronics*, 2(2), 355-366.
- Bêche, B., Pelletier, N., Gaviot, E., & Zyss, J. (2014). Single-mode TE₀₀–TM₀₀ optical waveguides on su-8 polymer. *Optics Communications* 230(1-3), 91-94.
- Bellini, A. & Güçeri, S. (2003). Mechanical characterization of parts fabricated

- using fused deposition modeling. *Rapid Prototyping Journal*, 9(4), 252–264.
- Bogue, R. (2013). 3D printing: The dawn of a new era in manufacturing? *Assembly Automation*. 33(4), 307–311.
- Carlyon, E. E., Lowe, C. R., Reid, D., & Ian, B. (1992). A single mode fibre-optic evanescent wave biosensor. *Biosensors and Bioelectronics* 7(2), 141-146.
- Chang-Yen, D. A., Eich, R. K., & Gale, B. K. (2005). A monolithic PDMS waveguide system fabricated using soft-lithography techniques. *Journal of Lightwave Technology*, 23(6), 2088.
- Chiang, K. S. (2010). Development of optical polymer waveguide devices. Proceedings of SPIE, Optoelectronic Integrated Circuits XII, 7605, 760507.
- Chin, M. K., Lee, C. W., Lee, S. Y., & Darmawan. S. (2005). High-index-contrast waveguides and devices. *Applied Optics*, 44(15), 3077-3086.
- Chong, J. S. (1969). Oxygen consumption during induction period of a photopolymerizing system. *Journal of Applied Polymer Science*, 13(1), 241-247.
- Crivello, J. V. & Reichmanis, E. (2014). Photopolymer Materials and Processes for Advanced Technologies. *Chemistry of Materials*, 26(1), 533-548.
- Dai, L., Cheng, T., Duan, C., Zhao, W., Zhang, W., Zou, X., Aspler, J., Ni, Y. (2019). 3D Printing Using Plant-derived Cellulose and Its Derivatives: A Review. *Carbohydrate Polymers*, 203, 71-86.

- Davis, K. M., Miura, K., Sugimoto, N. & Hirao, K. (1996). Writing waveguides in glass with a femtosecond laser. *Optics Letters* 21(21), 1729-1731.
- Decker, C., & Elazouk, B. (1995). *Current trends in polymer photochemistry* Edited by Norman S. Allen et.al. (1st ed.). New York: Ellis Horwood.
- Dell'Olio, F. & Passaro, V. M. N. (2007). Optical sensing by optimized silicon slot waveguides. *Optics Express*, 15(8), 4977-4993.
- Duguay, M. A., Kokubun, Y., Koch, T. L., & Pfeiffer, L. (1986). Antiresonant reflecting optical waveguides in SiO₂-Si multilayer structures, *Applied Physics Letters*, 49(1), 13-15.
- Dou, X., Wang, X., Lin, X., Ding, D., Pan, D. Z., & Chen, R. T. (2010). Highly flexible polymeric optical waveguide for out-of-plane optical interconnects. *Optics Express*, 18(15), 16227-16233.
- Dou, X., Wang, X., Huang, H., Lin, X., Ding, D., Pan, D. Z., & Chen, R.T. (2010). Polymeric waveguides with embedded micro-mirrors formed by Metallic Hard Mold," *Optics Express*, 18(1), 378-385.
- Eldada, L., Xu, C., Stengel, K. M., Shacklette, L. W., & Yardley, J. T. (1996). Laser-fabricated low-loss single-mode raised-rib waveguiding devices in polymers. *Journal of Lightwave Technology*, 14(7), 1704-1713.
- Eldada, L., & Shacklette, L. W. (2000). Advances in polymer integrated optics. *IEEE Journal of Selected Topics in Quantum Electronics*, 6(1), 54-68.
- Fernandez, F. A., Davies, J. B., Zhu, S., & Lu, Y. (1991). Sparse matrix eigenvalue solver for finite element solution of dielectric waveguides. *Electronics Letters*, 27(20), 1824-1826.

- Flores, A., Song, S., Yang, J.J., Liu, Z., & Wang, M. R. (2008). High-speed optical interconnect coupler based on soft lithography ribbons. *Journal of Lightwave Technology*, 26(13), 1956-1963.
- Friend, R., Gymer, R., Holmes, A., Burroughes, J., Marks, R., Taliani, C., Bradley, D. D. C, Dos Santos, D. A, Brédas, J. L., Lögdlund, M., & Salaneck, W.R. (1999). Electroluminescence in conjugated polymers. *Nature*, 397, 121-128.
- Gasó, P., Pudiš, D., Martinček, I., & Jandura, D. (2014). Fabrication of optical waveguide structures based on PDMS using photoresist fibers. *19th Polish-Slovak- Czech Optical Conference on Wave and Quantum Aspects of Contemporary Optics, Proceeding of SPIE, 9441*, 944101-1.
- Geskus, D., Shanmugam, A., Garcia-Blanco, S. M., & Pollnau, M. (2012). Giant optical gain in a rare-earth-ion-doped microstructure. *Advanced Materials*, 24(10), OP19-22.
- Gibson, I., Rosen, D., & Stucker, B. (2015). *Additive Manufacturing Technologies* (2nd ed.). New York: Springer.
- Glebov, A. L., Lee, M. G., Yokouchi, K. (2007). Integration technologies for pluggable backplane optical interconnect systems. *Optical Engineering*, 46(1), 015403.
- Goell, J. E. (1974). Loss mechanisms in dielectric waveguides. *Introduction to Integrated Optics*. Boston: Springer.
- Gramotnev, D. K. & Bozhevolnyi, S. I. (2010). Plasmonics beyond the diffraction limit. *Nature Photonics*. 4(2), 83-91.

- Groover, M. P. (2013). *Fundamentals of Modern Manufacturing: Materials, Processes, and Systems* (5th ed.). USA: John Wiley & Sons, Inc.
- Haralick, R. M., Shanmugam, K., & Dinstein, I. (1973). Textural feature for image classification. *IEEE Transactions on Systems, Man, and Cybernetics*. SMC-3(6), 610–621.
- Hashim, A., Bamiedakis, N., Beals, J., Hao, Y., Penty, R., & White, I. (2011). Polymer based board-level optical interconnects. In *proceedings of 2011 IEEE 2nd International Conference on Photonics*, Malaysia.
- Hayata, K., Koshiba, M., Eguchi, M., & Suzuki, M. (1986). Vectorial Finite-Element Method Without Any Spurious Solutions for Dielectric Waveguiding Problems Using Transverse Magnetic-Field Component. *IEEE Transactions on Microwave Theory and Techniques*, 34(11), 1120-1124.
- Hoffmann, M., & Voges, E. (2002). Bulk silicon micromachining for MEMS in optical communication systems. *Journal of Micromechanics and Microengineering*, 12(4), 349-360.
- Holtrup, R. (2015). *Design and construction of a multi-material 3D DLP printer*. (Bachelor thesis). University of Twente, Enschede, Netherlands.
- Hong, M., Yuhsuan, J., & Dalton, L. R. (2002). Polymer based optical waveguide: Material, Processing and Device. *Advanced Materials*, 14(19), 1339-1365.
- Hopkinson, N., Haque, R., & Dickens, P. (2005). *Rapid Manufacturing: An Industrial Revolution for a Digital Age* (1st ed.). United Kingdom: John

Wiley and Sons Ltd.

- Hossam, K., Soham, W., Changxue, X., & Fakhrul, A. (2019). Digital light processing (DLP) 3D-printing technology and photoreactive polymers in fabrication of modified-release tablets. *European Journal of Pharmaceutical Sciences*, 135, 60-67.
- Hosseinkhannazer, H., Kostiuk L. W., & McMullin, J. N. (2008). Two-species microparticle detection in optofluidic biochips with polymeric waveguides. *Proceeding of SPIE 7099, Photonics North, 7099*, 70990H-1.
- Hsieh, J., Weng, C.-J., Yin, H.-L., Lin, H.-H., & Chou, H.-Y. (2005). Realization and characterization of SU-8 micro cylindrical lenses for in-plane micro optical systems. *Microsystem technologies*, 11(6), 429-437.
- Huang, B., Du, Z., Yong, T., & Han, W. (2017). Preparation of a novel hybrid type photosensitive resin for stereolithography in 3D printing and testing on the accuracy of the fabricated parts. *Journal of Wuhan University of Technology-Mater Sci. Ed*, 32(3), 726-732.
- Hull, C. W., Spence, S. T., Lewis CW, Vinson, W., Freed, R. S., Smalley, D. R (1998). Stereolithographic Curl Reduction. *US, US 5772947 A*.
- Hunsperger, R. G. (1984). *Integrated optics: theory and technology* (2nd ed.). Berlin Heidelberg: Springer.
- Hu, H., Ricken, R., Sohler, W., & Wehrspohn, R. B. (2007). Lithium Niobate Ridge Waveguides Fabricated by Wet Etching. *IEEE Photonics*

Technology Letters. 19(6), 417-419.

- Hu, J., & Menyuk, C. R. (2009). Understanding leaky modes: slab waveguide revisited. *Advance in Optics and Photonics*, 1(1), 58-106.
- Hu, R., Dai, D., & He, S. (2008). A small polymeric ridge waveguide with a high index contrast. *Journal of Lightwave Technology*, 26(13), 1964-1968.
- Iizuka, K. (2002). *Element of Photonics: For Fiber and Integrated Optics*. Vol II ed.). New York: John Wiley and Sons Inc.
- Immonen, M., Karppinen, M., & Kivilahti, J. K. (2009). Fabrication and characterization of polymer optical waveguides with integrated micromirrors for three-dimensional board-level optical interconnects. *IEEE Transactions on Electronics Packaging Manufacturing*, 28(4), 304-311.
- Jalali, B., Yegnanarayanan, S., Yoon, T., Yoshimoto, T., Rendina, I., & Coppinger, F. (1998). Advances in silicon-on-insulator optoelectronics. *IEEE Journal of Selected Topics in Quantum Electronics*, 4(6), 938-947.
- Jiang, G., Baig, S., & Wang, M. R. (2013). Flexible Polymer Waveguides with Integrated Mirrors Fabricated by Soft Lithography for Optical Interconnection. *Journal of Lightwave Technology*, 31(11), 1835-1841.
- Jinghai, Yi., Ryan, F. L., Matthew, G. D., Timothy, N., Bean, T. C., Diane, S. B., Virji, M. A., & Stefaniak, A. B. (2016). Emission of particulate matter from a desktop three-dimensional (3D) printer. *Journal of Toxicology and Environmental Health, Part A*, 79(11), 453-465.

- Katal, G., Tyagi, N., & Joshi, A. (2013). Digital Light Processing and its Future Applications. *International Journal of Scientific and Research Publications*, 3(4), 2250-3153.
- Kawachi, M. (1990). Silica waveguides on silicon and their application to integrated optic components. *Optical and Quantum Electronics*, 22(5), 391-416.
- Kelly, B. E., Bhattacharya, I., Heidari, H. S. M., Spadaccini, C. M., Taylor, H. K. (2019). Volumetric additive manufacturing via tomographic reconstruction. *Science*, 363(6431), 1075-1079.
- Kemp, N. T., McGrouther, D., Cochrane, J. W., & Newbury, R. (2007). Bridging the gap: polymer nanowire devices. *Advanced Materials*, 19(18), 2634–2638.
- Ke, X., Wang, M. R., & Li, D. (2006). All-optical controlled variable optical attenuator using photochromic sol gel material. *IEEE Photonics Technology Letters*, 18(9), 1025-1027.
- Khatri, A., Dhawangale, A., & Mukherji, S. (2019). Single step, mould-free fabrication of polymer optical waveguides for localized surface plasmon resonance based sensing platform. *Sensors & Actuators: B. Chemical*, 280, 243-255.
- Kim, J. S., Kang, J. W., & Kim, J. J. (2003). Simple and low cost fabrication of thermally stable polymeric multimode waveguides using a UV-curable epoxy. *Japanese Journal of Applied Physics*, 42(1-3), 1277-1279.

- Klein, J., Stern, M., Franchin, G., Kayser, M., Inamura, C., Dave, S., Weaver, J. C., Houk, P., Colombo, P., Yang, M., & Oxman, N. (2015). Additive manufacturing of optically transparent glass. *3D Printing and Additive Manufacturing*, 2(3), 92-105.
- Koch, T. B., Davies, J. B., & Wickramasinghe, D. (1989). Finite element/finite difference propagation algorithm for integrated optical device. in *Electronics Letters*, 25(8), 514-516.
- Koo, J. S., Williams, R. B., Gawith, C. B. E., Watts, S. P., Emmerson, G. D., Albanis, V., Smith, P. G. R. & Gossel, M. C. (2003). UV written waveguide devices using crosslinkable PMMA-based copolymers. *Electronics Letters*, 39(4), 394-395.
- Koshiha, M., Mitobe, S., & Suzuki, M. (1984). Finite-Element Analysis of Periodic Waveguides for Acoustic Waves. *The Japan Society of Applied Physics*, 23(23-1), 139-141.
- Koshiha, M., Hayata, K., & Suzuki, M. (1985). Improved Finite-Element Formulation in Terms of the Magnetic Field Vector for Dielectric Waveguides. *IEEE Transactions on Microwave Theory and Techniques*, 33(3), 227-233.
- Koshiha, M. (1992). *Optical waveguide analysis* (1st ed.). New York: McGraw-Hill.
- Lee, T. E., Sonny, J. E., Hoyle, C. E., & Guymon, C. A. (2004). The effect of monomer structure on oxygen inhibition of (meth)acrylates photopolymerization. *Polymer*, 45(18), 6155–6162.

- Leung, D. M. H., Kan, X. B., Rahman, B. M. A., Kejalakshmy, N., & Grattan, K. T. V. (2011). Optimizing the power confinement in silicon slot waveguides by use of Finite Element Method. *Passive Components and Fiber-Based Devices VIII, Proceedings of SPIE (Optical Society of America)*, 8307, 83071A.
- Ligon, S. C., Liska, R., Stampfl, J., Gurr, M., Mulhaupt, R. (2017). Polymers for 3D Printing and Customized Additive Manufacturing. *Chemical Reviews*, 117(15),10212–10290.
- Lin, X., Hosseini, A., Dou, X., Subbaraman, H., & Chen, R. T. (2013). Low-cost board-to-board optical interconnects using molded polymer waveguide with 45degree mirrors and inkjet-printed micro-lenses as proximity vertical coupler. *Optics Express*, 21(1), 60-69.
- Lu, Y., Mapili, G., Suhali, G., Chen, S., & Roy, K. (2006). A Digital Micro-Mirror Device-Based System for the Microfabrication of Complex, Spatially Patterned Tissue Engineering Scaffolds. *Journal of Biomedical Materials Research. Part A*. 77(2), 396–405.
- Mackenzie, J. I. (2007). Dielectric solid-state planar waveguide lasers: a review. *IEEE Journal of Selected Topics in Quantum Electronics*, 13(3), 626-637.
- Melloni, A., Costa, R., Cusmai, G., & Morichetti, F. (2009). The role of index contrast in dielectric optical waveguides. *International Journal of Materials and Product Technology*, 34(4), 421-437.
- Metzger, M. C., Hohlweg-Majert, B., Schwarz, U., Teschner, M., Hammer, B.,

- & Schmelzeisen, R. (2008). Manufacturing splints for orthognathic surgery using a three-dimensional printer. *Oral Surgery, Oral Medicine, Oral Pathology, Oral Radiology and Endodontics*, 105(2), e1-e7.
- Miller, S. E. (1964). Directional control in light-wave guidance. *The Bell System Technical Journal*. 43(4), 1727-1739.
- Miller, S. E. (1969). Integrated optics: An introduction. *The Bell System Technical Journal*, 48(7), 2059-2069.
- Mookherjea, S. (2004). Semiconductor coupled-resonator optical laser. *Applied Physics Letters*, 84(17), 3265–3267.
- Mohan, R. E., Neha, P., Shalu, T., Darshana, K., & Sreelatha, K. (2015). Fabrication of ZnO and doped ZnO waveguides deposited by spin coating. In *proceedings of International Conference on Materials Science and Technology (ICMST 2012)*, India.
- Morisawa, M., Amemiya, Y., Kohzu, H., Liang, C. X., & Muto, S. (2001). Plastic optical fibre sensor for detecting vapour phase alcohol. *Measurement Science and Technology*, 12(7), 877– 881.
- Muto, S., Uchiyama, K., Vishnoi, G., Morisawa, M., Xin Liang, C., Machida, H., & Kiso, K. (1998). Plastic optical fiber sensors for detecting leakage of alkane gases and gasoline vapors. *Proceedings of SPIE, Photopolymer Device Physics, Chemistry and Applications IV*, 3417.
- Muto, S., Suzuki, O., Amano, T., & Morisawa, M. (2003). A plastic optical fibre sensor for real-time humidity monitoring. *Measurement. Science and Technology*, 14(6), 746–750.

- Nagata, J., Honma, S., Morisawa, M., & Muto, S. (2007). Development of polymer optical waveguide-type alcohol sensor. *Advanced Materials and Devices for Sensing and Imaging III, Proceedings of SPIE*, 6829, 682920.
- Neyer, A., Kopetz, S., Rabe, E., Kang, W., & Tombrink, S. (2005). Electrical-optical circuit board using polysiloxane optical waveguide layer. In *proceedings of 55th Electronic Components and Technology Conference (ECTC 2005)*, USA.
- Ngo, T. D., Kashani, A., Imbalzano, G., Nguyen, K. T. Q., Hui, D. (2018). Additive Manufacturing (3D Printing): A Review of Materials, Methods, Applications and Challenges. *Composites Part B: Engineering*, 143, 172–196.
- Ohji, H., Gennissen, P. T. J., French, P. J. & Tsutsumi, K. (2000). Fabrication of a beam-mass structure using single-step electrochemical etching for micro structures (SEEMS), *Journal of Micromechanics and Microengineering*, 10(3), 440-444.
- Okamoto, K. (1999). Recent progress of integrated optics planar light wave circuits. *Optical and Quantum Electronics*, 31(2), 107-129.
- Papakonstantinou, I., Selviah, D. R., Wang, K., Pitwon, R. A., Hopkins, K., & Milward, D. (2008). Optical 8-channel, 10 Gb/s MT pluggable connector alignment technology for precision coupling of laser and photodiode arrays to polymer waveguide arrays for optical board-to-board interconnects. In *proceedings of 58th Electronic Components and*

Technology Conference (ECTC 2008), USA.

Pavesi, L., & Guillot, G. (2006). *Optical Interconnects* (2006th ed.). Berlin Heidelberg: Springer.

Pelletier, N., Bêche, B., Tahani, N., Zyss, J., Camberlein, L., & Gaviot, E. (2007). Su-8 waveguiding interferometric micro-sensor for gage pressure measurement. *Sensors and Actuators A: Physical*, 135(1), 179-184.

Prajzler, V., Klapuch, J., Lyutakov, O., Huttel, I., Spirkova, J., Nekvindova, P., & Jerabek, J. (2011). Design, Fabrication and Properties of Rib Poly(methylmethacrylimide). *Optical Waveguides. Radioengineering*, 20(2), 479-485.

Rahman, B. M. A. (1995): Finite-element solution of integrated optical waveguide. *Progress in Electromagnetics Research*, 10, 187-216.

Rahman, B. M. A. & Agarwal, A. (2013). *Finite Element Modeling Method for Photonics* (2013th ed.). Boston: Artech House Books; Unabridged edition.

Ramaswamy, R. V., & Srivastava, R. (1988). Ion-exchanged glass waveguides: a review. *IEEE Journal of Lightwave Technology*, 6(6), 984-1000.

Ravve, A. (2006). *Light-Associated Reactions of Synthetic Polymers* (2006th ed.). New York: Springer.

Reed, G. T. (2008). *Silicon Photonics: The State of the Art* (1st ed.). England: John Wiley & Sons, Inc.

Rezem, M., Kelb, C., Rahlves, M., & Reithmeier, E. (2016). Low-cost

- fabrication of optical waveguides, interconnects and sensing structures on all-polymer based thin foils. *Proceeding of SPIE, Smart Photonic and Optoelectronic Integrated Circuits XVIII*, 9751, 975112- 975116.
- Robinson, G. (1995). The commercial development of planar optical biosensors. *Sensors and Actuators B: Chemistry*, 29(1-3), 31-36.
- Rodriguez, A., Vitrant, G., Chollet, P., & Kajzar, F. (2001). Optical control of an integrated interferometer using a photochromic polymer. *Applied Physics Letters*, 79(4), 461-463.
- Rogers, J. A. & Nuzzo, R. G. (2005). Recent progress in soft lithography. *Materials Today*, 8(2), 50-56.
- Saarinen, J. J., Weiss, S. M., Fauchet, P. M., & Sipe, J. (2005). Optical sensor based on resonant porous silicon structures. *Optics Express*, 13(10), 3754-3764.
- Saha, S. K., Wang, D., Nguyen, V. H., Chang, Y., Oakdale, J. S., Chen, S. C. (2019). Scalable Sub micrometer Additive Manufacturing. *Science*, 366(6461), 105-109.
- Schafer, K. J., Hales, J. M., Balu, M., Belfield, K. D., Van Stryland, E. W., & Hagan, D. J. (2004). Two-photon absorption cross-sections of common photoinitiators. *Journal of Photochemistry and Photobiology A: Chemistry*, 162(2-3), 497-502.
- Shen, G., Chen, P. C., Ryu, K., & Zhou, C. (2009). Devices and chemical sensing applications of metal oxides nanowires. *Journal of Materials Chemistry*, 19(7), 828-839.

- Shew, B. Y., Cheng, Y. C., & Tsai, Y. H. (2008). Monolithic SU-8 micro-interferometer for biochemical detections. *Sensors and Actuators, A: Physical*, 141(2), 299-306.
- Shi, Y., Zhang, C., Zhang, H., Bechtel, J. H., Dalton, L. R., Robinson, B. H., & William, H. S. (2000). Low (sub-1-volt) halfwave voltage polymeric electro-optic modulators achieved by controlling chromophore shape. *Science*, 88(5463), 119-122.
- Sieber, V. H., Kettlitz, S., Eschenbaum, C., Hollenbach, U., & Lemmer, U. (2012). Direct fabrication of PDMS waveguides via low-cost DUV irradiation for optical sensing, *Optics Express*, 20(27), 28855-28861.
- Snyder, A. W., & Love, J. D. (1983). *Optical Waveguide Theory* (1983 ed.). United States: Springer.
- Soref, R. A., & Lorenzo, J. P. (1985). Single-crystal silicon: a new material for 1.3 and 1.6 μm integrated-optical components. *Electronics Letters*, 21(21), 953-954.
- Stegeman, G. I., & Seaton, C. T. (1985). Nonlinear integrated optics. *Journal of Applied Physics B*, 58(12), R57-R78.
- Struk, P., Pustelny, T., Gut, K., Golaszewska, K., Kaminska, E., Ekielski, M., Pasternak, I., Lusakowska, E., & Piotrowska, A. (2009). Planar optical waveguides based on thin ZnO layers. *Optical and Acoustical Methods in Science and Technology*, 116(3), 414-418.
- Swargiary, K., Jarutatsanangkoon, P., Suwanich, P., Jolivot, R., & Mohammed, W. S. (2020). Single-step 3D-printed integrated optical system and its

- implementation for a sensing application using digital light processing technology. *Applied Optics*, 59(1), 122-128.
- Theiss, W. (1997). Optical properties of porous silicon, *Surface Science Reports*, 29(3-4), 91-93.
- Tien, P. K. (1971). Light waves in thin films and integrated optics. *Applied Optics*, 10(11), 2395-2413.
- Tong, X. C. (2014). *Advanced materials for integrated optical waveguides* (2014 ed.). Switzerland: Springer.
- Tsuji, Y., & Koshiba, M. (1996). A finite element beam propagation method for strongly guiding and longitudinally varying optical waveguides. *Journal of Lightwave Technology*, 14(2), 217-222.
- Tumbleston, J. R., Shirvanyants, D., Ermoshkin, N., Januszewicz, R., Johnson, A. R., Kelly, D., Chen, K., Pinschmidt, R., Rolland, J. P., Ermoshkin, A., Samulski, E. T., & DeSimone, J. M. (2015). Additive manufacturing. Continuous liquid interface production of 3D objects. *Science*, 347(6228), 1349-1352.
- Tung, K., Wong, W., & Pun, E. (2005). Polymeric optical waveguides using direct ultraviolet photolithography process. *Applied Physics A*, 80(3), 621-626.
- Vassallo, C. (1991). *Optical waveguide Concepts*. (1991 ed.). New York: Elsevier.
- Viphavakit, C., Atthi, N., Boonruang, S., Themistos, C., Komodromos, M., Mohammed, W. S. & Azizur Rahman, B. M. (2014). Realization of a

- polymer nanowire optical transducer by using the nanoimprint technique. *Applied Optics*, 53(31), 7487-7497.
- Wang, F., Yang, J., Chen, L., Jiang, X., & Wang, M. (2006). Optical switch based on multimode interference coupler. *IEEE Photonics Technology Letters*, 18(2), 421-423.
- Wang, L., Ren, J., Han, X., Claes, T., Jian, X., Bienstman, P., Baets, R., Zhao, M., & Morthier, G. (2012). A label-free optical biosensor built on a low-cost polymer platform. *IEEE Photonics Journal*, 4(3), 920-930.
- Wexler, A. (1969). Computational of electromagnetic fields. *IEEE transactions on Microwave Theory and Techniques*, 17(8), 416-439.
- Willis, K., Brockmeyer, E., Hudson, S., & Poupyrev, I. (2012). Printed optics: 3D printing of embedded optical elements for interactive devices. *Proceedings of the 25th Annual ACM Symposium on User interface Software and Technology*, 589-598.
- Wolfer, T., Bollgruen, P., Mager, D., Overmeyer, L., & Korvink, J. G. (2014). Flexographic and Inkjet Printing of Polymer Optical Waveguides for Fully Integrated Sensor Systems. *Procedia Technology*, 15, 521-529.
- Wong, W., & Pun, E. (2001). Polymeric waveguide wavelength filters using electron beam direct writing. *Applied Physics Letters*, 79(22), 3576-3578.
- Xia, Y., & Whitesides, G. M. (1998). Soft lithography, *Annual Review of Materials Science*, 28, 153-184.
- Xing, J. F., Zheng, M. L., & Duan, X. M. (2015). Two-photon polymerization

microfabrication of hydrogels: an advanced 3D printing technology for tissue engineering and drug delivery. *Chemical Society Reviews*, 44(15), 5031–5039.

Xu, Y., Wu, X., Guo, X., Kong, B., Zhang, M., Qian, X., Mi, S., & Sun, W. (2017). The Boom in 3D-Printed Sensor Technology. *Sensors*, 17(5), 1166-1203.

Zeinkiew, O. C., & Taylor, R. L. (1977). *The finite element method* (3rd ed.). London: McGraw-hill.

Zhang, J., & Xiao, P. (2018). 3D printing of photopolymers. *Polymer Chemistry*, 9(13), 1530–1540.

Zhang, S., Arya, R. K., Pandey, S., Vardaxoglou, Y., Whittow, W., & Mitra, R. (2016). 3D-printed planar graded index lenses. *IET Microwaves, Antennas & Propagation*, 10(13), 1411-1419.

National Institute for Occupational Safety and Health. Isopropyl Alcohol, (2011, September 28). Retrived from <https://www.cdc.gov/niosh/pel88/67-63.html>.

FDM Technology, About Fused Deposition Modeling Stratasys. Retrieved from <http://www.stratasys.com/3d-printers/technologies/fdm-technology>.



APPENDIX A

FEM code for calculation of mode for the designed structure

```

clear                % delete all variables
close all           % close all plot windows
delete(gcf('nocreate')); % get the current parallel pool and shut it down
set(0, 'DefaultFigurePosition', [0 0 1280 680],...
      'DefaultSurfaceEdgeColor', 'none',...
      'DefaultFigureColormap', parula) % set the plot window.
global lxx_g lyy_g small_tri large_tri % for using in other m files

%% get path, create timestamped result folder and load data
file_path = 'C:\Users\User02\Desktop\Kevin_FEM\FEM_1'; % path to save
results
config_path = strcat(file_path, 'config.xlsx'); % get config.xls path
structure_path = strcat(file_path, 'structure.xlsx'); % get structure.xls path
c1 = clock; % get current time for folder name
time = strcat(num2str(c1(1)), '-', num2str(c1(2)), '-', num2str(c1(3)),...
              '@', num2str(c1(4)), '.', num2str(c1(5))); % time in format year-month-
date @hour.min
result_path = strcat(file_path, 'result/result_', time); % add time to result
folder's name
mkdir(result_path); % make result folder

%% specify the range of setting file
data = xlsread(config_path, 'B3:O8'); % get all experiments (row 3-8)
data_sx = xlsread(structure_path, 'D9:H9'); % get structure data in x
data_sy = xlsread(structure_path, 'C4:C8'); % get structure data in y

%% structure setup
x_1 = [data_sx(1,1) data_sx(1,2) data_sx(1,3) data_sx(1,4) data_sx(1,5)]; %
length (um)
lx = sum(x_1); % total width
lxx = [sum(x_1(1:1)) sum(x_1(1:2)) sum(x_1(1:3)) sum(x_1(1:4)) sum(x_1(1:5))];
% accumulated width
lxx_g = lxx;
y_1 = [data_sy(5,1) data_sy(4,1) data_sy(3,1) data_sy(2,1) data_sy(1,1)]; %

```

```

length (um)
ly = sum(y_l); % total height
lyy = [sum(y_l(1:1)) sum(y_l(1:2)) sum(y_l(1:3)) sum(y_l(1:4)) sum(y_l(1:5))];
% accumulated height
lyy_g = lyy;
y_check = y_l(1) + y_l(2) + y_l(3) + y_l(4)/2; % aim at the middle of y4 for
checking results
small_tri = 0.04; % starting triangle size in meshing
large_tri = 0.10; % max triangle size after mesh refinement (It's actually a
mesh enlargement to reduce the number of tri)
%% meshing
[p,t] = meshing(lx,ly); % do meshing, p = point, t = triangle
hold on % hold on to the meshing plot. Will overlay with material in
"assign_material"
index_1 = [data(1,2) data(1,3) data(1,4)]; % refractive index of the first exp
t = assign_material(t,p,lxx,lyy,index_1); % t is now [p1 p2 p3 material x y],
plot meshing
savefig(strcat(result_path,'/mesh.fig')) % save the meshing in MATLAB format
save_path = strcat(result_path,'/mesh'); % prepare name for mesh.png
print(save_path,'-dpng','-r0'); % save fig as png
sprintf('meshing done'); % print to console

%% init variables and build bg
np = size(p,1); % the number of point
ne = size(t,1); % the number of element
sprintf('no. of point = %d',np)
sprintf('no. of triangle = %d',ne)
np3 = np*3; % multiply by 3 because there are 3 fields at each point
(Hx,Hy,Hz)
s_matrix = sparse([],[],[],np3,np3,0); % create a blank sparse matrix
bg = s_matrix; % init bg
disp('bg start')
bg = build_bg(bg,t,p,ne,np); % build bg matrix (the same for one mesh)
disp('bg done')

%% create cells for each iteration
exp_no = size(data,1); % the number of experiment, the number of row in
config.xls
itrn = max(data(:,5)); % use max to have space for every exp

```

```

eig_vector = cell(exp_no,itrn); % field value (total cell = exp_no * itrn)
eig_value = cell(exp_no,itrn); % k0^2
num_of_result = zeros(exp_no,itrn); % the number of result in each iteration
beta = zeros(exp_no,itrn); % propagation constant

%% start iterate through exp
for exp = 1:exp_no
    itrn = data(exp,5); % get itrn for each exp
    ag = cell(itrn,1); % an array of cells ag matrix for one exp
    [ag{:}] = deal(s_matrix); % deal s_matrix to all itrn of ag
%% init material and specify beta
    index = [data(exp,2) data(exp,3) data(exp,4)]; % get indices
    dlc = index.^2; % dielectric constant
    lamda = data(exp,1); % wavelength (um)
    k0 = 2*pi/lamda; % wavenumber
    shift = k0^2; % eigenvalue
    beta_lb = data(exp,13); % lower bound for finding beta
    beta_ub = data(exp,14); % upper bound for finding beta
    delta = beta_ub - beta_lb; % the range to find beta
    beta(exp,1:itrn) = beta_lb:delta/(itrn-1):beta_ub; % sweep beta
    bet = beta.^2; % create a new var for a clean equation
    alpha = 0.1; % penalty coefficient
    disp('ag start')
%% build ag
    parpool(4) % start parallel computation (4 cores)
    parfor itr = 1:itrn % distribute each iteration to each core
        sprintf('exp no. %d/%d, itrn %d ag start',exp,exp_no,itr) % print exp no.
        & itrn no.
        ag{itr} = build_ag(ag{itr},ne,beta(exp,itr),bet(exp,itr),np,t,p,dlc,alpha); %
        build ag (the core of this FEM)
        sprintf('exp no. %d/%d, itrn %d ag done',exp,exp_no,itr) % report when
        it's done
%% solve eigenvalue problem
        sprintf('exp no. %d/%d, itrn %d sptarn start',exp,exp_no,itr) % start solving
        eigenvalue problem of exp .. itrn ..
        [eig_vector{exp,itr},eig_value{exp,itr},num_of_result(exp,itr)] =
        sptarn(ag{itr},bg,shift*.998,shift*1.002,1,100*eps,3200); % sptarn is a
        MATLAB func
        sprintf('exp no. %d/%d, itrn %d sptarn done',exp,exp_no,itr) % report

```

```

when it's done
    end
    delete(gcf('nocreate')) % stop parallel computation
end
%% save result
c2 = clock; % get time to calculate elapsed time (c2-c1)
time = strcat(num2str(c2(1)),'-',num2str(c2(2)),'-',num2str(c2(3)),...
    '@',num2str(c2(4)),'.',num2str(c2(5))); % time in format year-month-date
@min.sec
save_path = strcat(result_path,'/data_',time,'.mat'); % path for saving data_year-
month-day @hour.min.mat
save(save_path,'beta','c1','c2','data','eig_value','eig_vector','exp_no','lx','lxx','ly','ly
y',...
    'ne','np','num_of_result','p','result_path','t','x_l','y_l'); % save almost
everything
%% result analysis
result_folder =
analyze_result_no_plot(eig_value,eig_vector,num_of_result,data,t,exp_no,np,y_
check); % result_folder -> 0 = no_mode, 1 = TE, 2 = TM, 3 = high_order
plot_all_and_save(eig_value,eig_vector,num_of_result,data,t,p,beta,exp_no,np,r
esult_path,result_folder,lxx,lyy); % plot and save to the correct folder

```

Assembly of element matrices

For the optical waveguide, the solution obtained by the FEM can be represented as a standard eigenvalue problem in the equation 3.39. In order to assemble the elements, equation 3.37 is considered. The nodal magnetic field vector $\{H_e\}$ over the cross section of triangular element and the shape function matrix $[N]^T$ are shown in the equation (A.1) and A.2) respectively,

$$\{H\}_e = [\{H_x\}_e \quad \{H_y\}_e \quad \{H_z\}_e]^T \quad (\text{A.1})$$

where $\{H_x\}$, $\{H_y\}$, $\{H_z\}$ are the nodal field vectors along each axis.

$$[N]^T = \begin{bmatrix} \{N\} & \{0\} & \{0\} \\ \{0\} & \{N\} & \{0\} \\ \{0\} & \{0\} & j\{N\} \end{bmatrix} \quad (\text{A.2})$$

where $\{N\}$ is the shape function vector and $\{0\}$, is the null vector. The term j arises, as for lossless cases H_z component is 90° out of phase with the transverse components.

Therefore, the equation 3.37 can be written as follows.

$$\{H\}_e = \begin{bmatrix} N_1 & N_2 & N_3 & 0 & 0 & 0 & 0 & 0 & 0 \\ 0 & 0 & 0 & N_1 & N_2 & N_3 & 0 & 0 & 0 \\ 0 & 0 & 0 & 0 & 0 & 0 & jN_1 & jN_2 & jN_3 \end{bmatrix} \begin{Bmatrix} H_{x1} \\ H_{x2} \\ H_{x3} \\ H_{y1} \\ H_{y2} \\ H_{y3} \\ H_{z1} \\ H_{z2} \\ H_{z3} \end{Bmatrix} \quad (\text{A.3})$$

With the Maxwell's equation, $(\nabla \times \mathbf{H})_e$, can be defined as:

$$(\nabla \times \mathbf{H})_e = [\nabla \times][N]^T \{H\}_e = \begin{bmatrix} 0 & -\partial/\partial z & \partial/\partial y \\ \partial/\partial z & 0 & -\partial/\partial x \\ -\partial/\partial y & \partial/\partial x & 0 \end{bmatrix} [N]^T \{H\}_e \quad (\text{A.4})$$

Form this equation (A.4), it can also be written as,

$$(\nabla \times \mathbf{H})_e = [Q]^T \{H\}_e \quad (\text{A.5})$$

where, the matrix $[Q]$ is defined by:

$$[Q] = \begin{bmatrix} \{0\} & -j\beta\{N\} & -\partial\{N\}/\partial y \\ j\beta\{N\} & \{0\} & \partial\{N\}/\partial x \\ j\partial\{N\}/\partial y & -j\partial\{N\}/\partial x & \{0\} \end{bmatrix} \quad (\text{A.6})$$

The solution to the optical waveguide problem can be obtained from Euler's equation, which can be transformed to a discretized form as in equation 3.38. By assuming isotropic media $[\varepsilon_r] = \varepsilon_r$ and substituting equation (A.5) into 3.38, the resulting equation is given below,

$$\frac{1}{\varepsilon_r} \iint_{\Omega} (\{H\}_e^T [Q]^* [Q]^T \{H\}_e) d\Omega - k_0^2 \iint_{\Omega} (\{H\}_e^T [M]^* [M]^T \{H\}_e) = 0 \quad (\text{A.7})$$

By summing all the elements over the cross-section of the guide, the above equation can be expressed in matrix form based on standard eigenvalue problem and is shown in the equation (A.8).

$$[A]\{H\} - k_0^2 [B]\{H\} = 0 \quad (\text{A.8})$$

where $[A]$ and $[B]$ are the global matrices of the eigenvalue equation. They are the summation of the element matrices for each triangular element of the discretized cross section of the optical waveguide and these matrices is given as follows,

$$[A] = \sum_e [A]_e = \sum_e \iint_{e} \frac{1}{\varepsilon_e} [Q]^* [Q]^T dx dy \quad (\text{A.9})$$

$$[B] = \sum_e [B]_e = \sum_e \iint_e [M]^* [M]^T dx dy \quad (\text{A.10})$$

$\frac{1}{\varepsilon_e}$ is the relative dielectric permittivity of the element, and $[A]_e$ and $[B]_e$ are the

element matrices which may be evaluated as follows:

For matrix $[A]_e$:

$$\begin{aligned}
 [A]_e &= \frac{1}{\epsilon_e} \iint_e \begin{bmatrix} \{0\} & j\beta\{N\} & -\partial\{N\}/\partial y \\ -j\beta\{N\} & \{0\} & \partial\{N\}/\partial x \\ -j\partial\{N\}/\partial y & j\partial\{N\}/\partial x & \{0\} \end{bmatrix} \begin{bmatrix} \{0\} & j\beta\{N\}^T & j\partial\{N\}^T/\partial y \\ -j\beta\{N\}^T & \{0\} & -\partial\{N\}^T/\partial x \\ -\partial\{N\}^T/\partial y & \partial\{N\}^T/\partial x & \{0\} \end{bmatrix} dx dy = \\
 &= \frac{1}{\epsilon_e} \iint_e \begin{bmatrix} \beta^2\{N\}\{N\}^T + \frac{\partial\{N\}}{\partial y} \frac{\partial\{N\}^T}{\partial y} & -\frac{\partial\{N\}}{\partial y} \frac{\partial\{N\}^T}{\partial x} & \beta\{N\} \frac{\partial\{N\}^T}{\partial x} \\ -\frac{\partial\{N\}}{\partial y} \frac{\partial\{N\}^T}{\partial x} & \beta^2\{N\}\{N\}^T + \frac{\partial\{N\}}{\partial x} \frac{\partial\{N\}^T}{\partial x} & \beta\{N\} \frac{\partial\{N\}^T}{\partial y} \\ \beta\{N\} \frac{\partial\{N\}^T}{\partial x} & \beta\{N\} \frac{\partial\{N\}^T}{\partial y} & \frac{\partial\{N\}}{\partial y} \frac{\partial\{N\}^T}{\partial y} + \frac{\partial\{N\}}{\partial x} \frac{\partial\{N\}^T}{\partial x} \end{bmatrix} dx dy
 \end{aligned}
 \tag{A.11}$$

The resulting matrix is a 9x9 real symmetric matrix and by using the shape function coefficients and the relation for a triangular element and the various terms can be determined as follows.

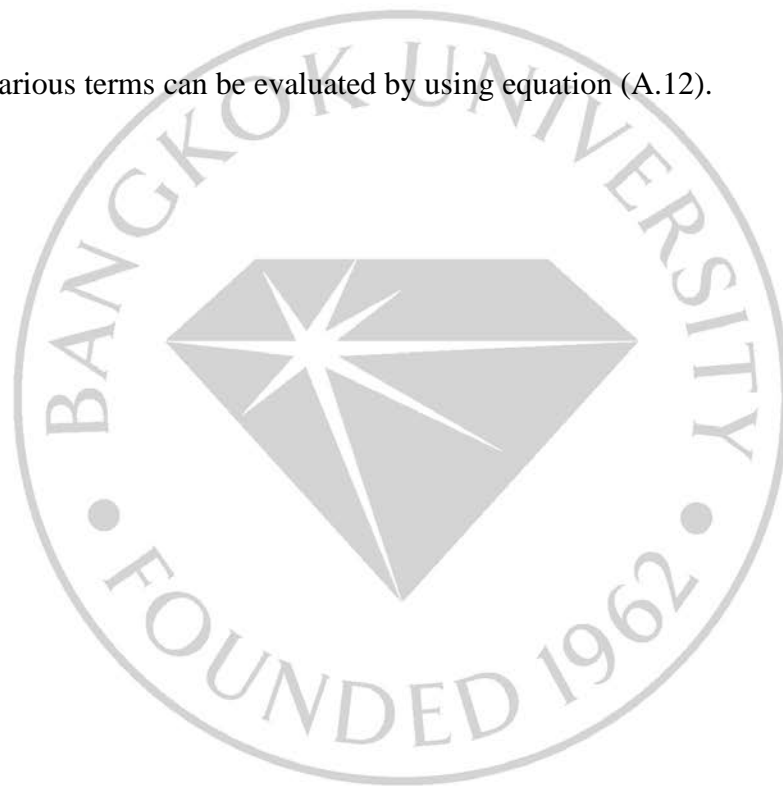
$$\iint_e N_1^i N_2^j N_3^k dx dy = \frac{i! j! k!}{(i+j+k+2)!} (2 \times \text{Area})
 \tag{A.12}$$

For the element matrix $[B]_e$:

$$\begin{aligned}
 [B]_e &= \iint_e [N]^* [N]^T dx dy = \iint_e \begin{bmatrix} \{N\} & \{0\} & \{0\} \\ \{0\} & \{N\} & \{0\} \\ \{0\} & \{0\} & -j\{N\} \end{bmatrix} \begin{bmatrix} \{N\}^T & \{0\}^T & \{0\}^T \\ \{0\}^T & \{N\}^T & \{0\}^T \\ \{0\}^T & \{0\}^T & j\{N\}^T \end{bmatrix} dx dy = \\
 &= \iint_e \begin{bmatrix} \{N\}\{N\}^T & \{0\}\{0\}^T & \{0\}\{0\}^T \\ \{0\}\{0\}^T & \{N\}\{N\}^T & \{0\}\{0\}^T \\ \{0\}\{0\}^T & \{0\}\{0\}^T & \{N\}\{N\}^T \end{bmatrix} dx dy
 \end{aligned}$$

(A.13)

where the various terms can be evaluated by using equation (A.12).



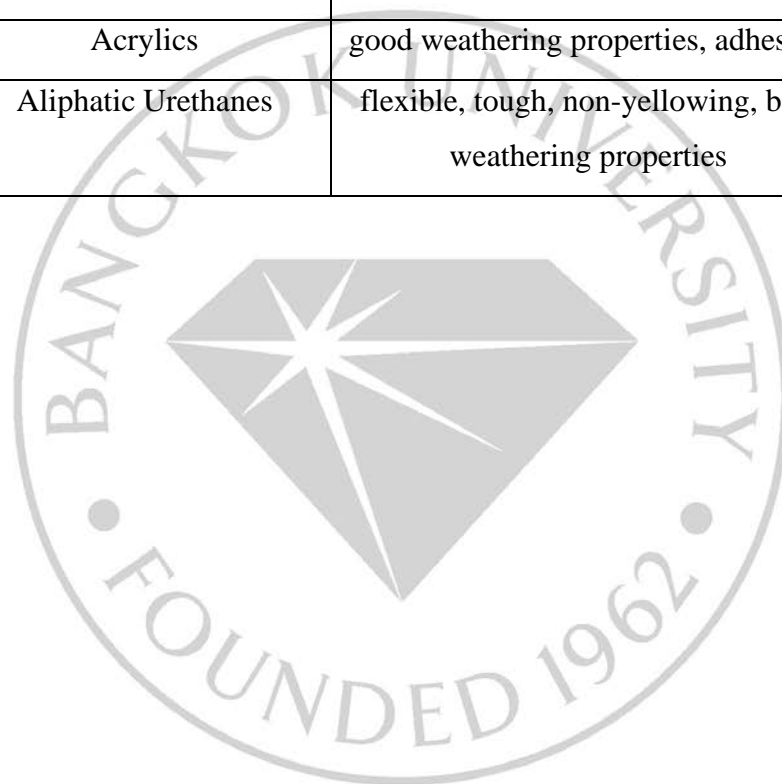
APPENDIX B

Table B.1: Curing properties of various acrylates (3Dprinter.wikidot, 2011)

	P.Ester Acryl Olig.(16)	P.Ester Acryl Olig.(16)	Ethox.(3) BP-A Diacryl.	Ethox.(4) BP-A Diacryl.	Ethox.(10) BP-A Diacryl.	Ethox.(6) BP-A Triacryl.	Di-PEG Diacryl.	Epoxy.(2) Soybean Oil Acryl.
Fast Cure	Excellent	High	Good	Good		Good	Good	Very Low
Photocuring Specific	Yes	Yes	Yes	Yes	Yes			Yes
Abrasion Resistance	Excellent	Excellent	Good	High	Good	High	High	
Hardness	Good	Good	Good	Good	Good	Good	Good	Low
Impact Strength			Good	High	Good	High	High	
Heat Resistance			Good	Good		Good		
Weatherability	Excellent	Excellent				Good	Good	
Shrinkage	Low 9.0%	Low 7%	Low (5% ?)	Low (5% ?)	Low (5% ?)	Low (5% ?)	Low	Low (5% ?)
Adhesion	High	Good	Good	Good	Good	Good	Good	Good
Flexibility		High			Good		High	Good
Pigment Wetting								Good
Chemical Resistance	Good		Good	Good	Good	Good	Good	Low
Cost Effectiveness		Yes						
Viscosity	Low 300 mPa.s	Good 0.4-1 Pa.s	Intermediate 1-2 Pa.s	Good 0.65-1.2 Pa.s	Good 0.61 Pa.s	Low 75-150 mPa.s	Very Low 8-14 mPa.s	High 16-26 Pa.s
Health Riks	Skin, Eyes Low Irritant	Skin, Eyes Irritant	Eyes Irritant	Skin, Eyes Irritant	Skin, Eyes Low Irritant	Low	Skin, Eyes Irritant	Skin, Eyes Low Irritant

Table B.2: Properties of oligomer types (Idacavage, 2012)

<u>(Meth)Acrylate</u>	<u>Characteristics</u>
Epoxies	fast curing, hard, solvent resistant, lower cost
Aromatic Urethane	flexible, tough, lower cost than aliphatic urethanes
Polyesters	low viscosity, good wetting properties
Acrylics	good weathering properties, adhesion
Aliphatic Urethanes	flexible, tough, non-yellowing, best weathering properties



APPENDIX C

Product datasheet

Px88+ Neo UVResin
xPMMA
 剛性高透
 類PMMA剛性高透

適用於非高溫環境下高透件應用，適合模型高透外殼部件，高透明度耳機外殼等。離型能力優異，打印門檻相對較高，適合專業外殼結構設計工程師與透明高精度耳機外殼工業設計師使用。



Product name: HEXPolymer-Poly-6-Special physical properties, high permeability and yellowing resistance, light-curing 3D printing photosensitive resin

Model: Px88+

Color: extremely transparent

Liquidity: General

Spectrum: 365 ~ 420nm

Operating temperature: 25 +-5°C

Shore hardness: 80D

Viscosity: 500CPS (25°C)

Recommended printing layer thickness: 0.025 ~ 0.1mm (25 ~ 100µm)

Toughness performance: rigidity

Basic printing performance:

First layer exposure time: 60 ~ 100 seconds (the actual time depends on the platform material and equipment exposure efficiency)

Single layer exposure time: 15 ~ 25 seconds (the actual time depends on the equipment exposure efficiency)

[The actual optimal time is subject to the curing effect, the stacking will reduce the time, and the separation will increase the time]

Source: <https://item.taobao.com/item.htm?id=562890008001>



Monocure 3D STANDARD photo-reactive clear resin has been designed to use in SLA & projector type DLP 3D Printers for UV wavelengths up to 420nm. The transparent appearance allows you to see internal features that would be useful for research, prototyping and engineering parts.

PHYSICAL PROPERTIES

Colour	Clear appearance
Viscosity	500 - 600cps @ 25°C (Brookfield RVT)
Odour	Negligible Characteristics
Shelf Life	12 months
Active Solids	100%
UV Cure	225nm to 420nm
Cure Speed	Fast with UV lasers and projectors
Storage	Dark cool, dry place out of direct sunlight
Wash Up	IPA (Isopropyl Alcohol)

PACKAGING

Monocure 3D3582C is packed in 500ml.

www.Monocure3D.com.au
 ABN 26 053 713 849
 14 Alexander Street, Auburn
 NSW 2144 AUSTRALIA

CONDITIONS: Our information is given in good faith and is based on result obtained from experience and test however as the actual end use of the product is beyond our control, all recommendation and suggestions are made without guarantee. No representative or agent of ours has the authority to waive or alter these conditions.

T: (612) 9644 9611
 F: (612) 9644 9288
 E: administrator@monocure3d.com.au

APPENDIX D

Gray-Level Co-Occurrence Matrix (GLCM) code for texture analysis

```

%% CD to the path (no space in path allowed)
cd('/Users/BU-CROCCS/Desktop/BU/Images to process')
[images_file, path] = uigetfile('*.png','Choose an image'); %% Select the image to
analyse

imOrigin = imread([path images_file]); %% Check the size of image
                                        %% For memory preallocation
imgray = rgb2gray(imOrigin);           % Convert to grayscale
% Set the offset
% Offset of 1 at 0 degree, 45 degree, 90 degree and 135 degree
GLCMstep1 = graycomatrix(imgray,'Offset',[0 1;-1 1;-1 0;-1 -1]);
% Offset of 2 at 0 degree, 45 degree, 90 degree and 135 degree
GLCMstep2 = graycomatrix(imgray,'Offset',[0 2;-2 2;-2 0;-2 -2]);
% Offset of 5 at 0 degree, 45 degree, 90 degree and 135 degree
GLCMstep5 = graycomatrix(imgray,'Offset',[0 5;-5 5;-5 0;-5 -5]);
% Calculate the GLCM for different offsets
% Offset of 1
statsstep1 =
graycoprops(GLCMstep1,{'contrast','correlation','energy','homogeneity'});
% Offset of 2
statsstep2 =
graycoprops(GLCMstep2,{'contrast','correlation','energy','homogeneity'});
% Offset of 5
statsstep5 =
graycoprops(GLCMstep5,{'contrast','correlation','energy','homogeneity'});

```

APPENDIX E

Processed ImageMetrics applied:

GLCM: Gray-Level Co-Occurrence Matrix

The aim of the metrics is to measure the texture of an image.

Statistic measured:

Contrast: Measure the local variations in co-occurrence matrix.

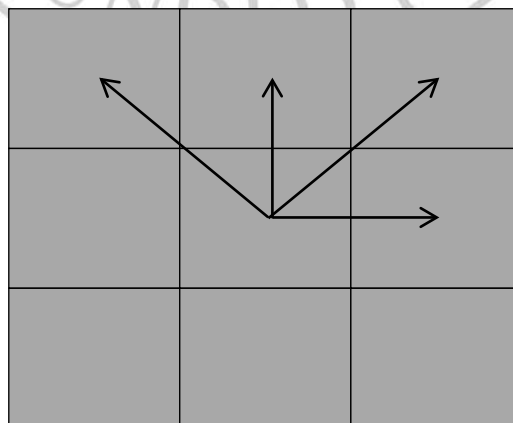
Correlation: Measures the joint probability occurrence of a specified pixel pairs

Energy: Provides the sum of squared elements in the GLCM (uniformity/angular second moment).

Homogeneity: Measures the closeness of the distribution of elements in the GLCM to the GLCM diagonal.

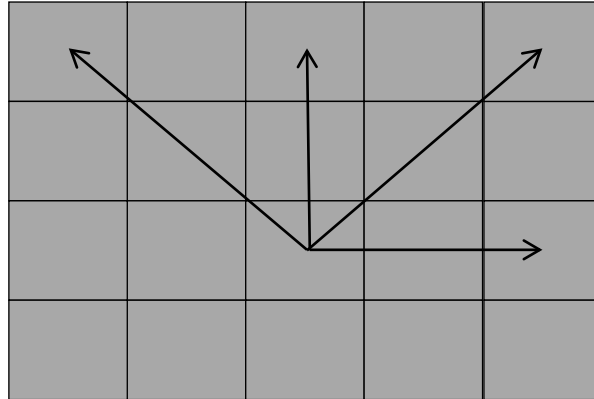
Different steps and angles:

- Pixel step size 1, angle 0° , 45° , 90° , 135°



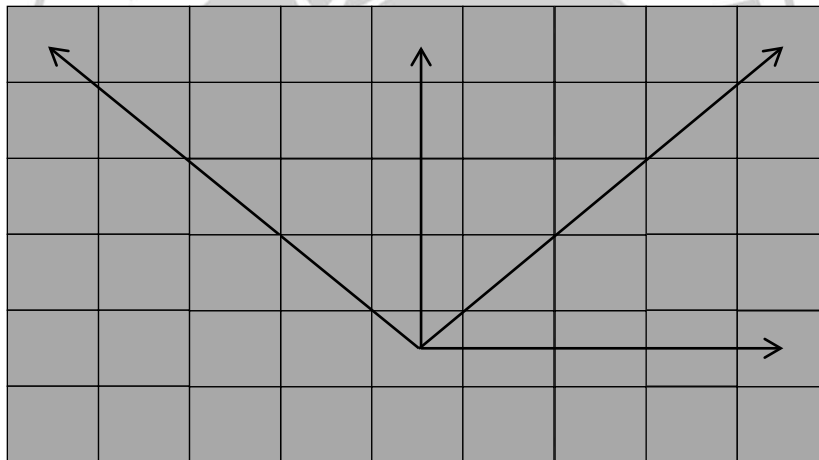
Step 1, angle 0, 45, 90, 135

- Pixel step size 2, angle 0° , 45° , 90° , 135°



Step 2, angle 0, 45, 90, 135

- Pixel step size 5, angle 0° , 45° , 90° , 135°



Step 5, angle 0, 45, 90, 135

Input images:

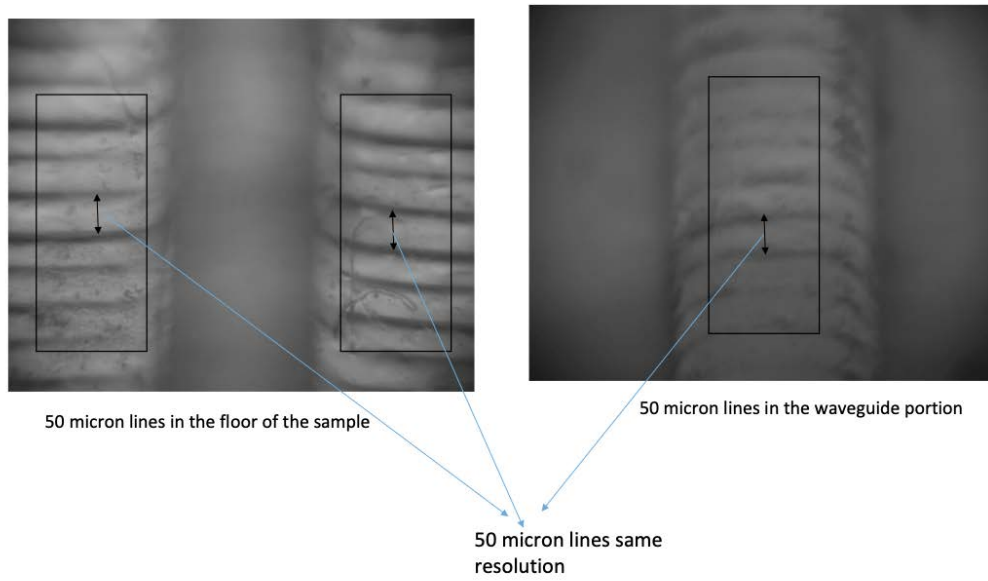


Figure E1: Left Center and Right image

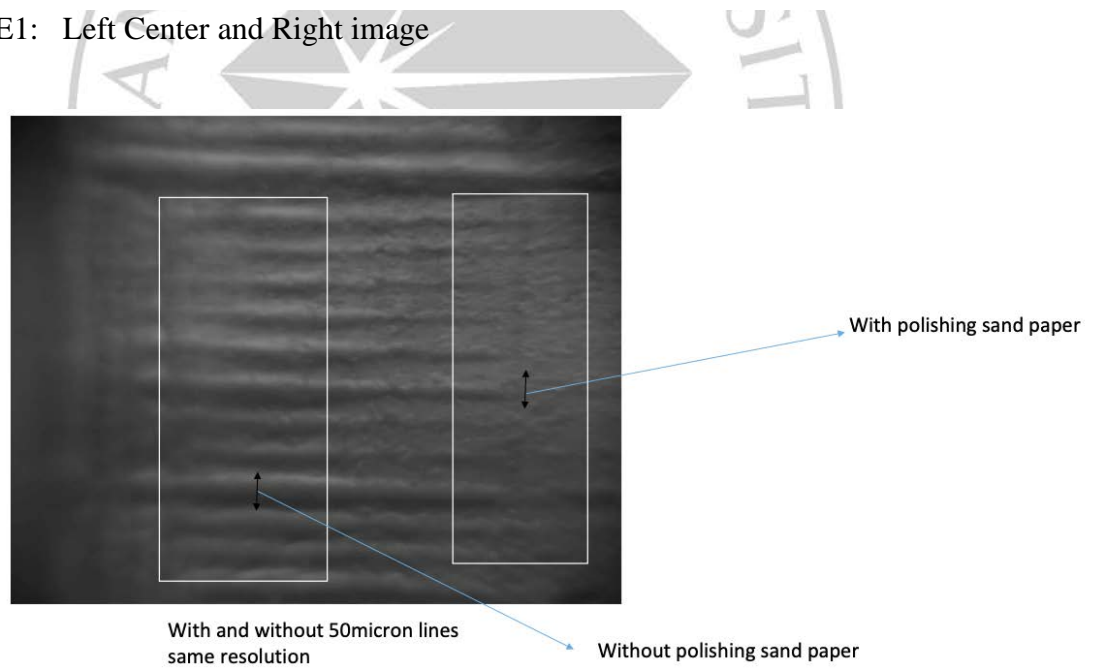


Figure E2: Left and Right image

Results:

Slide Left Image 1				
1 pixels step	0 degree	45 degree	90 degree	135 degree
Contrast	0.023277134	0.051123094	0.045703684	0.052920557
Correlation	0.977131669	0.949805496	0.955139254	0.948035522
Energy	0.377985421	0.358996585	0.362634202	0.35803955
Homogeneity	0.988361433	0.974438453	0.977148158	0.973539721
2 pixels step	0 degree	45 degree	90 degree	135 degree
Contrast	0.042438866	0.091548571	0.085960935	0.095005662
Correlation	0.958298685	0.910151818	0.915678976	0.90673778
Energy	0.364839404	0.333163252	0.336661811	0.33140251
Homogeneity	0.978780567	0.954225715	0.957019532	0.952497169
5 pixels step	0 degree	45 degree	90 degree	135 degree
Contrast	0.080224348	0.186595109	0.182803196	0.191340011
Correlation	0.921117211	0.817067084	0.821038848	0.812286036
Energy	0.339988052	0.28047513	0.282145796	0.278424268
Homogeneity	0.959887826	0.906702446	0.908598402	0.904329995

Slide Center Image 1				
1 pixels step	0 degree	45 degree	90 degree	135 degree
Contrast	0.015789205	0.045551137	0.037983566	0.039666826
Correlation	0.985480803	0.958072106	0.965049002	0.963493898
Energy	0.353787233	0.334010238	0.338973889	0.337922842
Homogeneity	0.992105398	0.977224432	0.981008217	0.980166587
2 pixels step	0 degree	45 degree	90 degree	135 degree
Contrast	0.02980199	0.086490194	0.07404663	0.07402422
Correlation	0.972590438	0.92029877	0.931809573	0.931808635
Energy	0.343998523	0.308313295	0.315845255	0.316034376
Homogeneity	0.985099005	0.956754903	0.962976685	0.96298789
5 pixels step	0 degree	45 degree	90 degree	135 degree
Contrast	0.061801975	0.198990681	0.176182903	0.169915151
Correlation	0.943149368	0.81617346	0.837450796	0.843154053

Energy	0.322598779	0.248468793	0.258936004	0.26257497
Homogeneity	0.96911053	0.900591595	0.911908548	0.915106177

Slide Right Image 1				
1 pixels step	0 degree	45 degree	90 degree	135 degree
Contrast	0.0218317	0.022739007	0.022165034	0.023559294
Correlation	0.955557825	0.953717622	0.954887724	0.952036067
Energy	0.487650429	0.486811243	0.487245427	0.486029913
Homogeneity	0.98908415	0.988630496	0.988917483	0.988220353
2 pixels step	0 degree	45 degree	90 degree	135 degree
Contrast	0.022643556	0.026634879	0.025727028	0.027860384
Correlation	0.953903555	0.945805617	0.947645336	0.943269737
Energy	0.486955083	0.483218936	0.483889427	0.482061579
Homogeneity	0.988678222	0.986682561	0.987136486	0.986069808
5 pixels step	0 degree	45 degree	90 degree	135 degree
Contrast	0.027843762	0.042853751	0.041827316	0.047339235
Correlation	0.943323099	0.912929208	0.914931356	0.903552717
Energy	0.482276517	0.468508103	0.468990441	0.464360854
Homogeneity	0.986078119	0.978573124	0.979086342	0.976330383

Slide Left Image 2				
1 pixels step	0 degree	45 degree	90 degree	135 degree
Contrast	0.012201186	0.038006304	0.034171055	0.037255133
Correlation	0.983211325	0.947756816	0.952995391	0.948789265
Energy	0.463475984	0.443090605	0.446265431	0.443658123
Homogeneity	0.993899407	0.980996848	0.982914472	0.981372433
2 pixels step	0 degree	45 degree	90 degree	135 degree
Contrast	0.022918842	0.071103779	0.066504449	0.069400836
Correlation	0.968486739	0.902437529	0.908618044	0.904772849
Energy	0.454793645	0.417951025	0.421732364	0.419177385
Homogeneity	0.988540579	0.964448111	0.966747776	0.965299582

5 pixels step	0 degree	45 degree	90 degree	135 degree
Contrast	0.044876994	0.162069501	0.155653468	0.158712794
Correlation	0.938423851	0.778830561	0.786836866	0.783389299
Energy	0.437256885	0.355283415	0.360282596	0.357352017
Homogeneity	0.977561503	0.918965249	0.922173266	0.920643603

Slide Right Image 2				
1 pixels step	0 degree	45 degree	90 degree	135 degree
Contrast	0.014901478	0.036631409	0.033404709	0.038443296
Correlation	0.954205491	0.887219369	0.897132042	0.881643871
Energy	0.700458017	0.681765723	0.684644285	0.680231156
Homogeneity	0.992549261	0.981684295	0.983297646	0.980778352
2 pixels step	0 degree	45 degree	90 degree	135 degree
Contrast	0.027909806	0.065396017	0.06271241	0.068293822
Correlation	0.914245318	0.798352189	0.806555477	0.789433505
Energy	0.688913663	0.657753167	0.660133951	0.655445651
Homogeneity	0.986045097	0.967301991	0.968643795	0.965853089
5 pixels step	0 degree	45 degree	90 degree	135 degree
Contrast	0.056025705	0.12589347	0.125137243	0.128224473
Correlation	0.827796023	0.610586659	0.612951874	0.60348462
Energy	0.664921856	0.610530612	0.611182716	0.608903525
Homogeneity	0.971987147	0.937053265	0.937431378	0.935887764

BIODATA

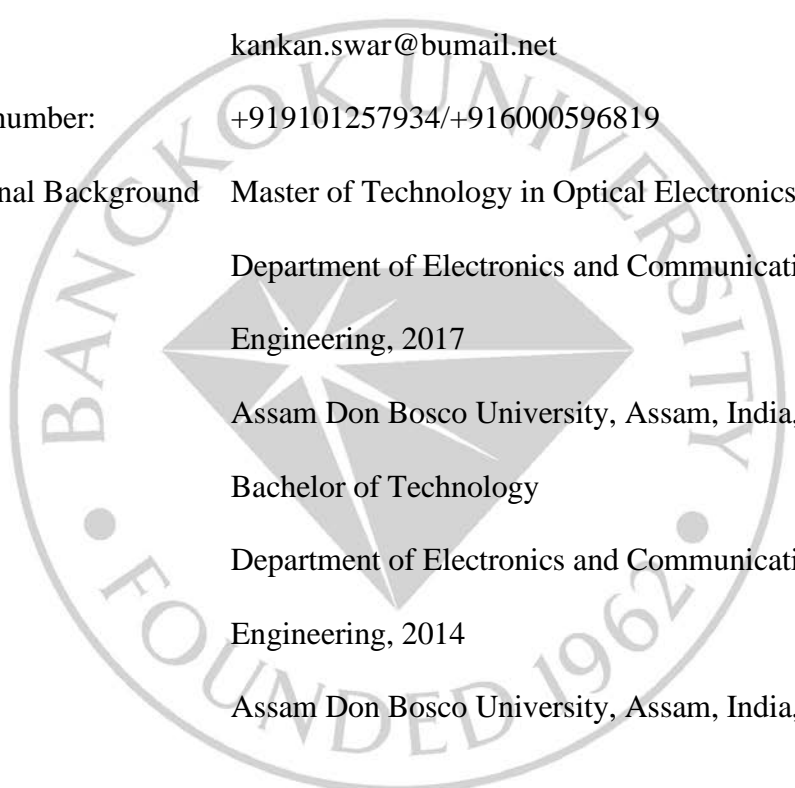
Name – Last name: Kankan Swargiary

Address: Tihu Town, Ward No-3, Near Tihu Hospital
District- Nalbari, Assam, India, 781371

Email: kevin.angelene.swargiary06@gmail.com
kankan.swar@bumail.net

Contact number: +919101257934/+916000596819

Educational Background Master of Technology in Optical Electronics
Department of Electronics and Communication
Engineering, 2017
Assam Don Bosco University, Assam, India, 781017
Bachelor of Technology
Department of Electronics and Communication
Engineering, 2014
Assam Don Bosco University, Assam, India, 781017

A large, semi-transparent watermark of the Bangkok University logo is centered on the page. The logo is circular with a diamond shape in the center. The text 'BANGKOK UNIVERSITY' is written along the top inner edge of the circle, and 'FOUNDED 1962' is written along the bottom inner edge. The diamond shape contains a stylized star or sunburst design.

Bangkok University
License Agreement of Dissertation/Thesis/ Report of Senior Project

Day 26 Month 06 Year 2021

Mr. Kankan Swargiary now living at Tihu Town
Soi Ward No 3 Street Near Tihu Hospital
Sub-district Nalbari District Nalbari
Province Assam, India Postal Code 781371
being a Bangkok University student, student ID 9600900014
Degree level Bachelor Master Doctorate
Program Electrical and Computer Engineering Department School of Engineering
School Graduate School hereafter referred to as “the licensor”

Bangkok University 119 Rama 4 Road, Klong-Toey, Bangkok 10110 hereafter referred to as “the licensee”

Both parties have agreed on the following terms and conditions:

1. The licensor certifies that he/she is the author and possesses the exclusive rights of dissertation/thesis/report of senior project entitled 3D printed optical system based on Digital Light Processing technology for sensing applications submitted in partial fulfillment of the requirement for Doctor of Engineering in Electrical and Computer Engineering of Bangkok University (hereafter referred to as “dissertation/thesis/ report of senior project”).
2. The licensor grants to the licensee an indefinite and royalty free license of his/her dissertation/thesis/report of senior project to reproduce, adapt, distribute, rent out the original or copy of the manuscript.
3. In case of any dispute in the copyright of the dissertation/thesis/report of senior project between the licensor and others, or between the licensee and others, or any other inconveniences in regard to the copyright that prevent the licensee from

reproducing, adapting or distributing the manuscript, the licensor agrees to indemnify the licensee against any damage incurred.

This agreement is prepared in duplicate identical wording for two copies. Both parties have read and fully understand its contents and agree to comply with the above terms and conditions. Each party shall retain one signed copy of the agreement.



(Kankan Swargiary) Licensor



(Director, Library and Learning Center) Licensee



(Dean, School of Engineering) Witness



(Program Director) Witness